

**Effects of symmetry and novel
geometries on observable
properties of liquid crystal
systems**

Nikita V. Solodkov

School of Physics and Astronomy

University of Leeds

A thesis submitted for the degree of

Doctor of Philosophy

31st December 2019

The candidate confirms that the work submitted is his own, except where work which has formed part of jointly authored publications has been included. The contribution of the candidate and the other authors to this work has been explicitly indicated below. The candidate confirms that appropriate credit has been given within the thesis where reference has been made to the work of others.

List of publications contributing to this thesis:

1. N. V. Solodkov, M. Hird, and J. C. Jones, "Alignment and electro-optical properties of SmC* with direct transition to N* phases", *Molecular Crystals and Liquid Crystals*, vol. 647, no. 1, p. 162, 2017. This material contributed to Chapter 3.
Author contributions: N. V. S. and J. C. J. designed the research. N. V. S. performed the research. J. C. J. supervised the project with inputs from M. H.
2. N. V. Solodkov, M. Nagaraj, and J. C. Jones, "Effects of monoclinic symmetry on the properties of biaxial liquid crystals," *Physical Review E*, vol. 97, no. 4, p. 042702, 2018. This material contributed to Chapter 3.
Author contributions: N. V. S. and J. C. J. designed the research. N. V. S. performed the research. M. N. and J. C. J. supervised the project.
3. N. V. Solodkov, J.-u. Shim, and J. C. Jones, "Self-assembly of fractal liquid crystal colloids," *Nature Communications*, vol. 10, no. 1, p. 198, 2019. This material contributed to Chapter 4.
Author contributions: N. V. S. and J. C. J. designed the research and performed confocal microscopy. Nikita V. Solodkov performed the research. J.-u. S. and J. C. J. supervised the project.
4. N. V. Solodkov, A. Saxena, and J. C. Jones, "Electrically driven rotation and non-reciprocal motion of nematic liquid crystal colloids," *submitted*, 2019. This material contributed to Chapter 5.
Author contributions: N. V. S., A. S. and J. C. J. designed the research. A. S. performed majority of the experiments with some contributions from N. V. S. N. V. S. performed the analysis and the numerical simulations. J. C. J. supervised the project.

This copy has been supplied on the understanding that it is copyright material and that no quotation from the thesis may be published without proper acknowledgement.

This thesis is dedicated to my father and mother

Abstract

From atoms to galaxies, symmetry plays a key role in providing structure and coherence to the laws of nature. The aim of this thesis is to investigate the effects of symmetry on a variety of liquid crystal systems. Liquid crystals are anisotropic fluids, in which the rigid and anisotropic constituent molecules have a strong tendency to form mesophases with long-range orientational order. Within this classification, there exists a rich variety of distinct mesophases with varying degrees of orientational and positional order.

Tilted smectic liquid crystal phases, such as the smectic-C phase seen in calamitic liquid crystals, are usually treated using the assumption of biaxial orthorhombic symmetry. However, the smectic-C phase has monoclinic symmetry, thereby allowing a disassociation of the principal optic and dielectric axes based on symmetry and invariance principles. In this thesis, we demonstrate this by comparing optical and dielectric measurements for two materials with highly first order direct transitions from the nematic to the smectic-C phases. The results show a high difference between the orientations of the principal axes sets, which is interpreted as the existence of two distinct cone angles for optical and dielectric frequencies.

Dispersion of microparticles in nematic liquid crystals offers novel means for controlling both their orientation and position through the combination of topology and external stimuli. In this thesis, we use double emulsions of water droplets inside radial nematic liquid crystal droplets to form various structures, ranging from linear chains to three-dimensional fractals. These systems are modelled as a formation of satellite droplets, distributed around a larger, central core droplet. Furthermore, we extend this reasoning to explain the formation of fractal structures. We show that a distribution of droplet sizes plays a key role in determining the symmetry properties of the resulting geometric structures.

Finally, we disperse cuboid and triangular prism shaped particles in a nematic liquid crystal. Experimental observations are compared with numerical simulations to understand the influence of geometry and symmetry on the orientation and position of the particles, both with and without the application of electric fields. We find that a particle's orientation depends on its aspect ratio and the applied voltage for both particle types. We show that geometric symmetry breaking plays a key role in the

dynamics, which prompts the field induced rotation of the particles and allows the triangular prisms to travel perpendicular to the applied electric field.

Acknowledgements

First of all, I would like to thank my supervisors Cliff Jones and Jung-uk Shim for giving me the opportunity to study under their guidance. I would also like to thank my industrial supervisor Joe Sargent and Merck Chemicals Limited for supporting my studentship and giving me the freedom to explore my own research interests. Furthermore, I wish to express my gratitude to everyone that helped during the course of my studies. In particular, I wish to thank James Bailey and Antariksh Saxena for their continuous support in the liquid crystals laboratory. Finally, and most importantly, I would like to thank my parents for their ongoing guidance, love and support.

Nomenclature and abbreviations

δ_{ij}	Kronecker delta
ϵ_{ijk}	Levi-Civita symbol
k	Boltzmann constant
T	Temperature
T_c	Critical temperature
Σ	Entropy
F	Free energy
Z	Partition function
E	Electric field
V	Voltage (electrostatic potential)
P	Electric polarisation
\mathcal{P}	Spontaneous polarisation
D	Electric displacement field
χ_{ij}^e	Electric susceptibility tensor
ϵ_0	Permittivity of free space
ϵ_{ij}	Relative permittivity tensor
$\bar{\epsilon}$	Average relative permittivity
$\Delta\epsilon$	Dielectric anisotropy
$\partial\epsilon$	Dielectric biaxiality
n_o	ordinary refractive index
n_e	extraordinary refractive index
Δn	birefringence
H	Magnetic field
χ_{ij}^m	Magnetic susceptibility tensor
$\bar{\chi}$	Average magnetic susceptibility
$\Delta\chi$	Magnetic susceptibility anisotropy
μ_0	permeability of free space
v	Domain
s	Boundary of v
\hat{s}	outward pointing unit normal on s

S	Uniaxial scalar order parameter
P	Biaxial scalar order parameter
\mathbf{n}	Long-axis director
Q_{ij}	Nematic order tensor
K_i	Elastic constants in the vector representation
L_i	Elastic constants in the tensor representation
w_i	Anchoring coefficients of the director on s in the vector representation
W_i	Anchoring coefficients of the director on s in the tensor representation
A, B, C	Landau coefficients
\mathbf{a}	Smectic layer normal
δ	Out of plane tilt of \mathbf{a} in a parallel plate capacitor
θ_c	Cone angle in the smectic-C phase
θ_o	Optical cone angle
θ_ε	Dielectric cone angle
$\partial\theta$	Cone angle asymmetry
N_c	Characteristic primary orbit capacity of satellites
Θ	Angular separation of neighbouring satellites in the same orbit
h	Nematic inclusion separation factor
r	Ratio of the core to satellite radii and reciprocal fractal scaling factor
D	Fractal dimension
$\mathcal{L}, \mathcal{T}, \mathcal{W}$	Particle dimension such that $\mathcal{T} < \mathcal{L} < \mathcal{W}$
D_{2D}	2D diagonal length of the particle
d	Inner separation gap of parallel plate capacitor cells
d_c	Critical inner separation gap of parallel plate capacitor cells
Φ_0	Out of plane tilt angle of rectangular particles
Φ_0^∞	Asymptote of Φ_0 as $d/\mathcal{L} \rightarrow \infty$
Φ	Voltage dependent out of plane tilt angle of the rectangular particles
V_{ch}	Characteristic voltage
Φ_∞	Asymptote of Φ as $V/V_{ch} \rightarrow \infty$
BC	Boundary condition
NLC	Nematic liquid crystal
SmA	Smectic-A liquid crystal
SmC	Smectic-C liquid crystal

Iso	Isotropic fluid
Cry	Crystalline phase
NBC	Normal boundary condition
TBC	Tangential boundary condition
AC	Alternating current
DC	Direct current

Contents

List of figures	xi
List of tables	xiv
1 Physics of liquid crystals — an introduction	1
1.1 A phase of matter	1
1.1.1 Liquid crystal phases	2
1.1.2 Symmetry groups	3
1.1.3 Application of symmetry groups to liquid crystals	5
1.1.4 Nematic order parameter	6
1.1.5 Maier-Saupe phase transition	8
1.2 Continuum description	12
1.2.1 Nematic order tensor	12
1.2.2 Landau phase transition	12
1.2.3 Elasticity	14
1.2.4 Boundary conditions	16
1.2.5 Electric fields	18
1.2.6 Magnetic fields	21
1.2.7 Topological defects	21
1.3 Solving liquid crystal problems	23
1.3.1 Minimisation	23
1.3.2 Analytical solutions	25
1.3.3 Numerical methods	25
1.3.4 Modelling the parallel plate capacitor	26
1.4 Thesis road map	29

2	Methodology	30
2.1	Polarising optical microscopy	30
2.2	Confocal microscopy	31
2.3	Dielectric spectroscopy	32
2.4	Microfluidics	34
3	Effects of monoclinic symmetry on the properties of biaxial liquid crystals	37
3.1	Introduction	37
3.2	Monoclinic Symmetry and the Dielectric Tensor	38
3.3	Governing Equations	40
3.4	Materials and Methods	43
3.5	Results and Discussion	47
3.6	Conclusion	50
4	Self-assembly of fractal liquid crystal colloids	52
4.1	Introduction	52
4.2	Methods	53
4.3	Self-assembly of radial inclusions	54
4.4	Primary orbit satellite packing	59
4.5	Fractals	63
4.6	Conclusion	67
5	Electrically driven rotation and non-reciprocal motion of nematic liquid crystal colloids	69
5.1	Introduction	69
5.2	Methods	70
5.3	Quasistatic orientation	72
5.4	Restricted geometries and non-reciprocal motion	76
5.5	Conclusion	80
6	Discussion	81
	References	85

List of Figures

1.1	Liquid crystal phases	2
1.2	Local symmetries of the nematic and smectic-C phases	6
1.3	Visual representation of the first seven axially symmetric, real, spherical harmonics	7
1.4	Nematic distribution function	8
1.5	Visual representation of the statistical distribution of 500 molecular orientations on a unit sphere	10
1.6	Maier-Saupe representation of the thermodynamic free energy	11
1.7	Landau representation of the thermodynamic free energy density	13
1.8	Elastic deformations in liquid crystal systems	15
1.9	Liquid crystal boundary conditions	17
1.10	Free energy density of tangential boundary conditions	18
1.11	Parallel plate capacitor filled with a nematic liquid crystal	20
1.12	Illustration of a selection of 2D topological defects, accompanied by the corresponding director fields	22
1.13	Nematic director field and topological defects on particles' surfaces	23
1.14	Director orientation in a parallel plate capacitor	27
2.1	Director profile around two neighbouring inclusions	31
2.2	Montage of a series of confocal fluorescence images, scanned through the depth of the sample.	32
2.3	Effective permittivity and optical retardation in a parallel plate capacitor.	33
2.4	Radius of microfluidically generated droplets as a function of the flow rate ratio between the inner and the outer fluids.	35
2.5	Microfluidics of double emulsions.	36

3.1	Diagonalisation of the relative permittivity tensor	41
3.2	Optical and dielectric cone angles	41
3.3	Chemical structures for X and Y liquid crystals	43
3.4	Ferroelectric switching of the director in a smectic-C liquid crystal . . .	44
3.5	Director configurations in a smectic-C liquid crystal phase	45
3.6	Dielectric permittivity measurements	46
3.7	Angle measurements	46
3.8	Frequency dependence of the dielectric permittivity	47
3.9	Disassociation of optical and dielectric cone angles	48
3.10	Dielectric biaxiality	49
3.11	Optimised chemical structures for X and Y liquid crystals	51
4.1	Double emulsion formation	55
4.2	Structural self-assembly in double emulsion systems with normal boundary conditions	56
4.3	Satellite distortion network	57
4.4	Square antiprism satellite packing	59
4.5	Primary orbit capacity and packing	60
4.6	Switching between primary satellite configurations	62
4.7	Triangular satellite self-assembly in a parallel plate geometry	63
4.8	Octahedral satellite packing	63
4.9	Fractal satellite packing	65
4.10	Large scale, complex fractal satellite packing	66
5.1	2D numerical simulations of a cuboid shaped particle's out of plane tilt in cells filled with MLC-6204-000 nematic liquid crystal.	73
5.2	2D out of plane tilt of a cuboid shaped particle in cells filled with MLC-6204-000 NLC, as a function of the dimensionless cell gap and the dimensionless particle length.	74
5.3	Experimental and numerical voltage dependence of a particle's out of plane tilt in a geometrically unrestricted cell filled with MLC-6204-000 NLC.	75
5.4	Experimental voltage dependence of a particle's out of plane tilt in a constricted cell filled with MLC-6204-000 NLC.	77

5.5	Dynamics of colloidal particles caused by the motion of topological defects after the removal of high voltage	78
5.6	Image sequence showing positional tracking of a triangular prism.	79

List of Tables

1.1	32 point groups under the crystallography restriction	4
-----	-----------------------------------------------------------------	---

Chapter 1

Physics of liquid crystals — an introduction

1.1 A phase of matter

In a world governed by symmetry and invariance principles, complex mathematical concepts often realize themselves in seemingly simple physical systems, providing structure and coherence to the laws of nature.^[1] The symmetry of a phase of matter is central to describing material physical properties, phase transitions and the order parameters associated with those changes. At a young age we are taught about *the three phases of matter*: gases, liquids and solids. As we progress through higher education, we learn that phases such as plasmas, superfluids and many more exist. Among them, are *liquid crystals* — a class of ordered fluids, in which the rigid and anisotropic constituent molecules have a strong tendency to form mesophases with long-range orientational order and no or partial positional order.^[2]

The first observation of liquid crystals dates back to the mid-19th century, when Virchow^[3] and Mettenheimer^[4] observed that the suspension of myelin in water formed a texture when viewed through a microscope in between crossed polarisers. Although not recognized at the time, this was a *lyotropic* liquid crystal, in which the properties depend on solvent concentration. The more well studied, *thermotropic*, liquid crystals were first observed in cholesteryl benzoate by Friedrich Reinitzer in 1888^[5] and first recognized as a distinct phase of matter by Otto Lehman in 1889^[6]. Unlike their lyotropic counterparts, thermotropic liquid crystals change their properties with temperature. In this thesis, we will focus on the properties of several sub-phases of thermotropic liquid crystals.

1.1.1 Liquid crystal phases

In the simplest and most widely studied liquid crystal phase, the *nematic*, the constituent anisotropic molecules exhibit long range orientational order.^[2] In such systems, the molecules have no positional order but share a common pointing direction, described by headless unit pseudovector \mathbf{n} , called the director. Uniaxial nematics have cylindrical symmetry, which makes \mathbf{n} , along with all of its associated physical observable properties, indistinguishable from $-\mathbf{n}$.

At temperatures below the nematic (or sometimes directly below isotropic) phase, some materials become more ordered and confine themselves to layers, which behave as two dimensional fluids. These phases are known as *smectics* and come in many different types, depending on their properties. The two most commonly occurring smectic phases are the smectic-A (SmA) and the smectic-C (SmC) liquid crystals. Both SmA and SmC phases exhibit long range orientational order, short range positional order within layers and quasi-long range positional order perpendicular to layers.^[2,7] In the SmA phase, the so called director lies parallel to the *layer normal*, \mathbf{a} , while in the SmC phase, it tilts away from the layer normal at an angle, θ_c , known as the *cone angle*.^[2,7] This allows us to define the director in term of the \mathbf{a} and the projection of \mathbf{n} onto the layer plane, \mathbf{c} , as $\mathbf{n} = \mathbf{a} + \mathbf{c}$.

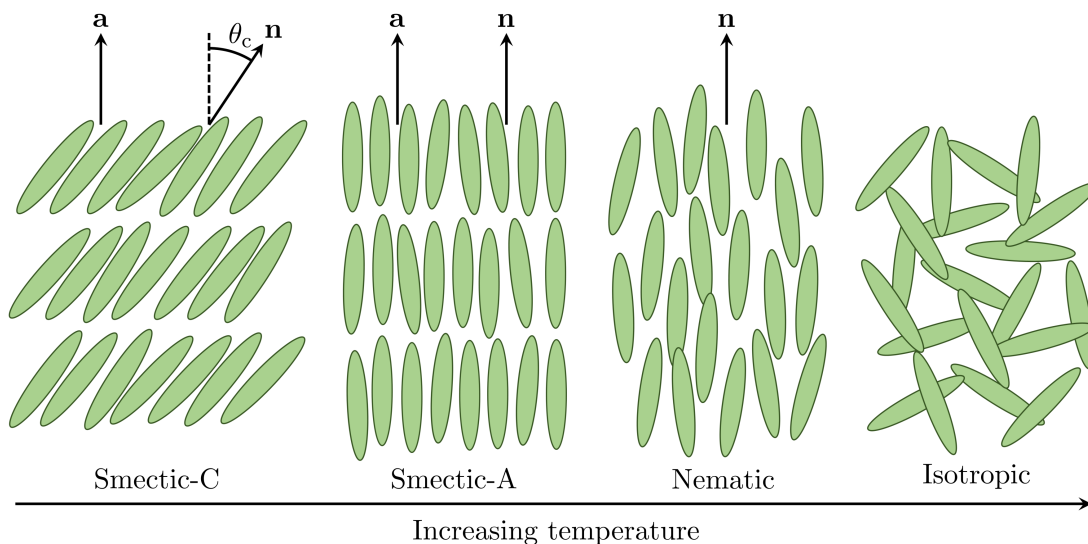


Figure 1.1: Liquid crystal phases. An illustration depicting the degrees of molecular self-assembly in smectic-C, smectic-A, nematic and isotropic phases with their corresponding directors and layer normals.

1.1.2 Symmetry groups

We often associate symmetry with balance and pleasing proportions. The importance of symmetry is so prominent in our lives that sometimes we imagine symmetry when it is partially missing. A more precise definition of symmetry can be found in the language of mathematics and physics. In order to classify the symmetry properties of a particular system, such as a molecule or a geometrical shape, we need to consider *symmetry operations*. When we apply a symmetry operation to a given system with matching symmetry properties, the result remains indistinguishable from its original state.^[8] Each operation is performed with respect to a symmetry element, all of which must pass through the same point of the symmetric object.^[9] A set of all permissible symmetry operations forms a *mathematical group* that describes the symmetry properties of a given system. The importance of symmetry classification is best illustrated by the Curie symmetry laws.^[10] In essence, a material can exhibit a given physical phenomenon if and only if its symmetry group is a subset of that of the physical phenomenon. One of the goals of this thesis is to illustrate the importance of symmetry in liquid crystal systems. In later chapters, we will demonstrate how simple molecular and geometrical symmetry arguments can help us explain complex physical phenomena.

If two groups have a *homomorphism* (a map, preserving group operations and the identity) which has a homomorphic inverse, the two are said to be *isomorphic*.^[11] When taking an abstract view of isomorphic groups, they appear to be the same. This allows the operations to be represented by a group of matrices, isomorphic to the group of symmetry operations. Furthermore, if A , B , C and the identity, E , are elements of a group G , the following properties must hold:^[11]

1. *Closure*: If $A, B \in G$, then the product $AB \in G$.
2. *Associativity*: $\forall A, B, C \in G$, $(AB)C = A(BC)$.
3. *Identity*: $\exists E$ such that $EA = AE = A \forall A \in G$.
4. *Inverse*: $\forall A \in G$, $\exists B = A^{-1} \in G$ such that $A^{-1}A = AA^{-1} = E$.

Since liquid crystals have a high degree of rotational and translational freedom,^[12] *point groups* are typically used to describe their properties.^[13] Point group operations leave at least one point in an identical position to the original picture. This is known as the *crystallography restriction*, which limits the number of groups to 32.^[14] Table 1 shows 32 point groups, which are labelled according to Schönflies notation:

Type	Point Groups
non-axial	C_1, C_s
cyclic	C_1, C_2, C_3, C_4, C_6
cyclic with horizontal planes	$C_{2h}, C_{3h}, C_{4h}, C_{6h}$
cyclic with vertical planes	$C_{2v}, C_{3v}, C_{4v}, C_{6v}$
dihedral	D_2, D_3, D_4, D_6
dihedral with horizontal planes	$D_{2h}, D_{3h}, D_{4h}, D_{6h}$
dihedral with planes between axes	D_{2h}, D_{3h}
improper rotation	S_4, S_6
cubic	T, T_h, T_d, O, O_h

Table 1.1: 32 point groups under the crystallography restriction.^[15]

- C_n represents n^{th} order cyclic rotation.
- D_n represents n^{th} order rotation with an addition of n C_2 axes perpendicular to it.
- S_n represents n^{th} order improper rotation axis.
- T represents the rotation axes of a tetrahedron, which has three C_2 axes and four C_3 axes.
- O represents the rotation axes of a cube, which has three C_4 axes, four C_3 axes and six C_2 axes.

The additional subscripts are used to indicate additional symmetry elements: σ_s for reflection, σ_i for inversion, σ_h for horizontal reflection, σ_v for vertical reflection and σ_d for diagonal reflection (through vertical symmetry planes passing *between* the C_2 axes as opposed to passing *through* them). In addition to this, there are three continuous groups for 3D space, falling into the following categories:^[15]

- *Curie groups* have the limit of $n \rightarrow \infty$.
- *Special orthogonal group* $SO(3)$ contains all rotations in 3D space.
- *Orthogonal group* $O(3)$ contains all rotations and reflections in 3D space.

In order of increasing symmetry, these point groups are $C_\infty, C_{\infty v}, D_\infty, C_{\infty h}, D_{\infty h}, SO(3)$ and $O(3)$.^[13]

1.1.3 Application of symmetry groups to liquid crystals

Isotropic fluids, consisting of molecules with no chirality, can be described by the $O(3)$ symmetry group, as they have an infinite number of C_∞ axes and symmetry planes. When chirality is added to an isotropic fluid, it loses the reflection and inversion symmetries and the symmetry group reduces to $SO(3)$.^[13]

Molecules in the nematic phase have no positional order but are orientated in a particular direction. To describe the symmetry of this phase, we take a space or time averaged representation.^[12] For uniaxial nematics, this can be represented by a cylinder whose long axis coincides with the director. From this, we can deduce that the nematic phase can be described by the $D_{\infty h}$ symmetry group. However, when we add chirality into the system, the nematic phase loses its symmetry planes and the symmetry group is reduced to D_∞ (it still has an infinite number of C_2 axes perpendicular to the helical axis). The same analysis can be performed for all other liquid crystal phases and unique properties to be obtained. Much like the nematic phase, the uniaxial SmA phase will have $D_{\infty h}$ symmetry and adding chirality to it will reduce the symmetry to D_∞ .

Recently, there has been much interest in the possibility of biaxial nematic phases and evidence for biaxial polar SmA phases was found in certain bent-core liquid crystals.^[16–22] The molecular bend angle in these systems further reduces the symmetry of phases they exhibit leading to biaxial and polar mesophases even though the constituent molecules are achiral in nature. These phases may have triclinic or monoclinic symmetry,^[19,23] but it is usually assumed that such phases have the highest symmetry D_{2h} and that the biaxial properties are orthorhombic.

In the smectic-C (SmC) phase, the director is tilted at the cone angle θ_c with respect to the layer normal \mathbf{a} (see Fig. 1.2). McMillan proposed a model based on dipole-dipole interactions, where the torque generated by the outbound dipoles causes the molecules to tilt in the smectic-C phase^[24]. A steric model was later proposed by Wulf, which considered the packing of symmetric molecules and suggested that a zigzag molecular shape is the primary driving mechanism in the breaking of the symmetry and formation of tilt within layers^[25]. This suggests that, for a system to form a SmC phase, the aliphatic end-chains of the molecules must be sufficiently long to induce a zigzag shape but insufficient to make the zigzag negligible. Since the molecules have monoclinic symmetry (described by the C_{2h} symmetry group), the SmC phase is inherently biaxial.

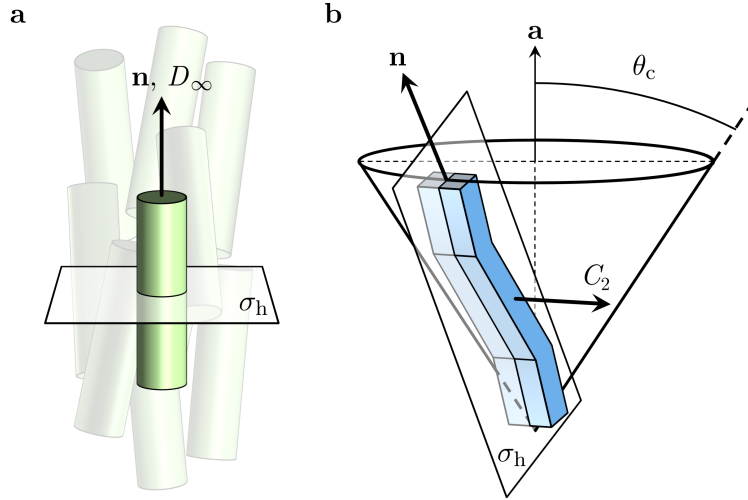


Figure 1.2: Local symmetries of the (a) nematic and (b) smectic-C phases. The directors are indicated with \mathbf{n} , the layer normal of the smectic-C phase by \mathbf{a} and the corresponding cone angle by θ_c . D_∞ represents the infinite-fold rotational symmetry of the nematic phase and C_2 represents the two-fold rotational symmetry of the smectic-C phase; both of which are accompanied by perpendicular mirror planes, σ_h .

1.1.4 Nematic order parameter

Consider an ensemble of cylindrical molecules with individual symmetry axes $\mathbf{n}^{(i)}$ that follow a distribution function $g(\mathbf{n}^{(i)}) = g(-\mathbf{n}^{(i)})$. Since g describes the probability of molecular orientations on the unit sphere, we can expand it as a series of the real spherical harmonics

$$Y_l^m(\theta, \phi) = \alpha(l, m) P_l^m(\cos \theta) \cos(m\phi), \quad (1.1)$$

P_l^m represents the *associated Legendre polynomials* and $\alpha(l, m)$ are the appropriate normalisation functions.^[15] Here, θ represents the angle between a given molecule and the director, and ϕ represents the azimuthal orientation of its projection onto the plane perpendicular to the director. Since $g(\mathbf{n}^{(i)}) = g(\theta)$ for uniaxial liquid crystals, our expansion must only consist of functions with $m = 0$. This reduces Equation (1.1) to the *Legendre polynomials* of degree l on a unit sphere:

$$\begin{aligned} P_0(\cos \theta) &= 1, \\ P_1(\cos \theta) &= \cos \theta, \\ P_2(\cos \theta) &= \frac{1}{2}(3 \cos^2 \theta - 1), \end{aligned}$$

$$\begin{aligned}
P_3(\cos \theta) &= \frac{1}{2}(5 \cos^3 \theta - 3 \cos \theta), \\
P_4(\cos \theta) &= \frac{1}{8}(35 \cos^4 \theta - 30 \cos^2 \theta + 3), \\
&\dots,
\end{aligned}$$

the first seven of which are illustrated in Figure 1.3. Furthermore, we can see that only *even* values of l allow the director to retain its head-tail symmetry. Therefore, our expansion of $g(\theta)$ can be expressed as an infinite series of $P_{2l}(\cos \theta)$

$$g(\theta) = \sum_{l=0}^{\infty} \frac{4l+1}{2} \langle P_{2l}(\cos \theta) \rangle P_{2l}(\cos \theta), \quad (1.2)$$

where $\langle P_{2l} \rangle$ represents the ensemble average of P_{2l} . This makes $\langle P_{2l} \rangle$ a natural choice for defining a series of order parameters that correspond to the contribution of the above Legendre polynomials to the overall distribution function.

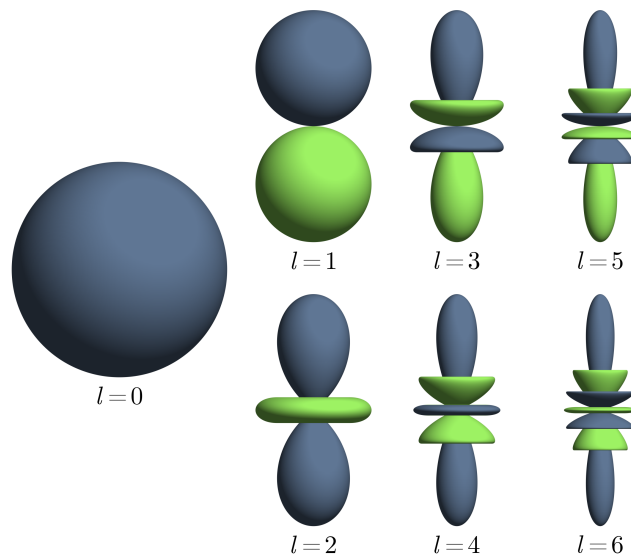


Figure 1.3: Visual representation of the first seven axially symmetric, real, spherical harmonics (Legendre Polynomials, defined on a unit sphere). The colour map corresponds to the sign of each function, with blue representing positive values and green representing negative values.

In practice, obtaining complete measurements of $g(\theta)$ is unrealistic due to insufficient accuracy of the required experiments. One advantage of using Equation (1.2) is that the first few $\langle P_{2l} \rangle$ can be measured using a large variety of techniques, such as nuclear magnetic resonance (NMR), polarised Raman spectroscopy,^[26] X-ray diffraction^[27,28] and many more.^[29–33] This allows us to recover a large amount of information about

the distribution of molecules in liquid crystals to make accurate predictions in molecular theories. The simplest choice is to use $\langle P_2 \rangle$ as the scalar order parameter (directly measured by NMR)

$$S = \langle P_2 \rangle = \int_{\mathbb{S}^2} P_2(\cos \theta) g(\theta) \sin \theta \, d\phi \, d\theta, \quad (1.3)$$

where $g(\theta)$ is chosen according to minimisation with the free energy constraints. Figure 1.4 shows the effects of truncating the series from Equation (1.2) at different values of l on the nematic distribution function. We can see that including a higher number of terms in the expansion results in a narrower peak. This means that the simplest approximation of $g(\theta)$ typically slightly underestimates the orientational order parameter of the system.

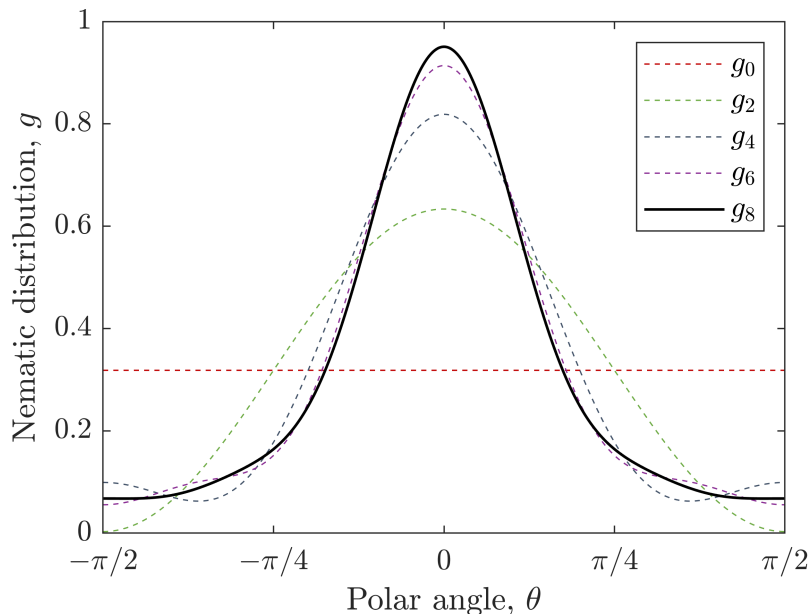


Figure 1.4: Nematic distribution function. Probability density of individual molecular orientations in an example nematic system, g_{2L} , as a sum of weighted Legendre polynomials, truncated at $l = L$, with $\langle P_0 \rangle = 1$, $\langle P_2 \rangle = 0.66$, $\langle P_4 \rangle = 0.27$, $\langle P_6 \rangle = 0.1$, $\langle P_8 \rangle = 0.03$ and $\langle P_{10} \rangle = 0.00$. Experimental measurements from Ref. [28]

1.1.5 Maier-Saupe phase transition

Naturally, we expect that there exists a temperature at which a liquid crystal phase becomes isotropic. To evaluate the nature of the corresponding phase transition, we

must perform a stability analysis of the (Helmholtz) free energy,

$$F = U - T\Sigma, \quad (1.4)$$

where U is the internal energy and Σ is the entropy of the system. Let us consider a system with N molecules, each interacting with M of its neighbours. Consequently, there will be a total of $MN/2$ unique pair interactions. For a given pair of neighbouring molecules, we can expect that there exists some interaction potential, I , that depends on their relative orientation to each other, given by ψ , and takes the form of

$$I = -ukT P_2(\cos \psi), \quad (1.5)$$

where u is a positive dimensionless constant. From this, we can express the total internal energy of the system as

$$U = \frac{MN}{2} \langle I \rangle = -\frac{MN}{2} ukT \langle P_2(\cos^2 \psi) \rangle = -\frac{MN}{2} ukT \left(\frac{3}{2} \langle (\mathbf{m} \cdot \mathbf{n})^2 \rangle - \frac{1}{2} \right), \quad (1.6)$$

where \mathbf{m} and \mathbf{n} are the individual directors of the two molecules in an interacting pair. If we assume that the neighbouring molecules interact with each other only via their centres of mass and neglect orientational correlations, $\langle n_i m_i n_j m_j \rangle \approx \langle m_i m_j \rangle \langle n_i n_j \rangle$, then we can simplify this to

$$U = -\frac{MN}{2} kT u S^2. \quad (1.7)$$

Similarly, we can expect that a given molecule interacts with the rest of the ensemble via an effective potential, J , that depends on the molecule's relative orientation to the average director, given by θ , that takes the form of

$$J = -bkT P_2(\cos \theta), \quad (1.8)$$

where b is the dimensionless energy of state in the mean-field approximation.^[7,34–36] Since the system is in thermodynamic equilibrium, the probability of a molecule existing in an orientation θ is given by the Boltzmann distribution,

$$g(\theta) = \frac{1}{Z} \exp(bP_2(\cos \theta)), \quad (1.9)$$

where Z is the partition function, given by

$$Z = \int_{\mathbb{S}^2} \exp(bP_2(\cos \theta)) \sin \theta \, d\theta \, d\phi. \quad (1.10)$$

This allows us to express the entropy of an individual molecule as $\Sigma_i = -k \ln g(\theta)$. Furthermore, we can now rewrite the scalar order parameter in the following way

$$S = \frac{1}{Z} \int_{\mathbb{S}^2} P_2(\cos \theta) \exp(bP_2(\cos \theta)) \sin \theta \, d\theta \, d\phi = \frac{\int_0^1 (3x^2 - 1) \exp\left(\frac{3bx^2}{2}\right) dx}{2 \int_0^1 \exp\left(\frac{3bx^2}{2}\right) dx}. \quad (1.11)$$

While not necessarily helpful analytically, we can (slightly) simplify this function to

$$S = \frac{1}{2b} \left(\frac{\sqrt{6b} \exp(3b/2)}{\sqrt{\pi} \operatorname{erfi}(\sqrt{3b/2})} - 1 \right) - \frac{1}{2}, \quad (1.12)$$

where $\operatorname{erfi}(\cdot)$ is the *imaginary error function*, which requires numerical integration.

By considering the limiting cases of Equation (1.12), we can see that $S \in (-0.5, 1)$ for $b \in (-\infty, \infty)$ and $S = 0$ for $b = 0$. Furthermore, we can find the inverse of this function, $b(S)$, to help visualise $g(\theta)$ on a unit sphere. A set of examples is shown in Figure 1.5, where $g(\theta)$ is visualised for $S = -0.4$, $S = 0$ and $S = 0.6$. As expected, when $S = 0$, the orientation of the molecules is distributed in such a way that the director cannot exist, which manifests itself when $S > 0$. We can also see a less intuitive system for $S < 0$. Here, the average orientation of the molecules is perpendicular to the director, while maintaining a random azimuthal distribution to ensure its uniqueness.

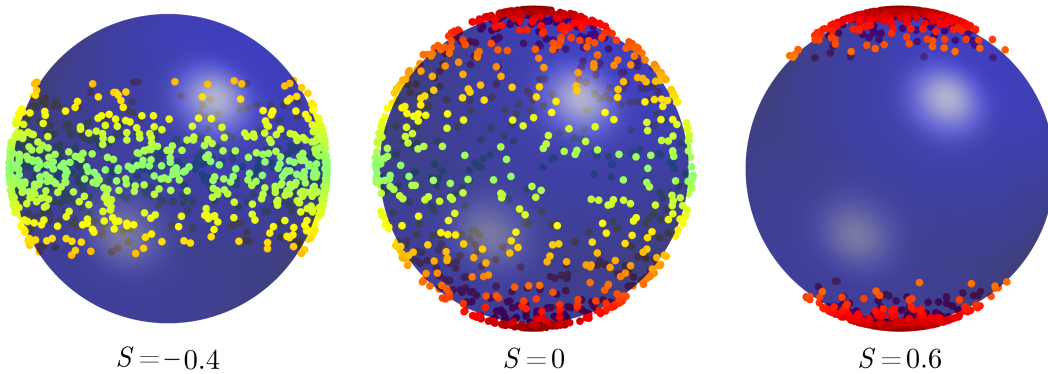


Figure 1.5: Visual representation of the statistical distribution of 500 molecular orientations on a unit sphere for $S = -0.4$, $S = 0$ and $S = 0.6$.

Following this, we can write Equation (1.4) as

$$\begin{aligned} F &= -\frac{MN}{2} kTuS^2 - TN \langle \Sigma_i \rangle \\ &= -\frac{MN}{2} kTuS^2 + NkT \langle \ln g(\theta) \rangle \end{aligned}$$

$$= NkT \left(-\frac{M}{2} uS^2 + bS - \ln Z \right), \quad (1.13)$$

where S and Z are functions of b . Existence of energetic minima of the system in the nematic phase can be ensured by letting the derivative of F with respect to b ,

$$\frac{\partial F}{\partial b} = NkT \left(-MuS \frac{\partial S}{\partial b} + b \frac{\partial S}{\partial b} + S - \frac{1}{Z} \frac{\partial Z}{\partial b} \right) = NkT \left(b - MuS \right) \frac{\partial S}{\partial b}, \quad (1.14)$$

vanish. From this, we find that $b = MuS$, which allows us to express the free energy of the system as

$$F = NkT \left(\frac{bS}{2} - \ln Z \right). \quad (1.15)$$

The free energy of the nematic phase can be evaluated as a function of S and compared to that of the isotropic phase, where $F(S=0) = -NkT \ln 4\pi$. This allows us to deduce that the nematic phase is stable for $S > 0.43$, where the free energy of the nematic phase falls below that of the isotropic phase.^[34] Therefore, when a fluid experiences a phase transition from an isotropic state to a nematic state, the scalar order parameter has a discontinuous jump from 0 to 0.43 — a *first order* phase transition. This is illustrated in Figure 1.6.

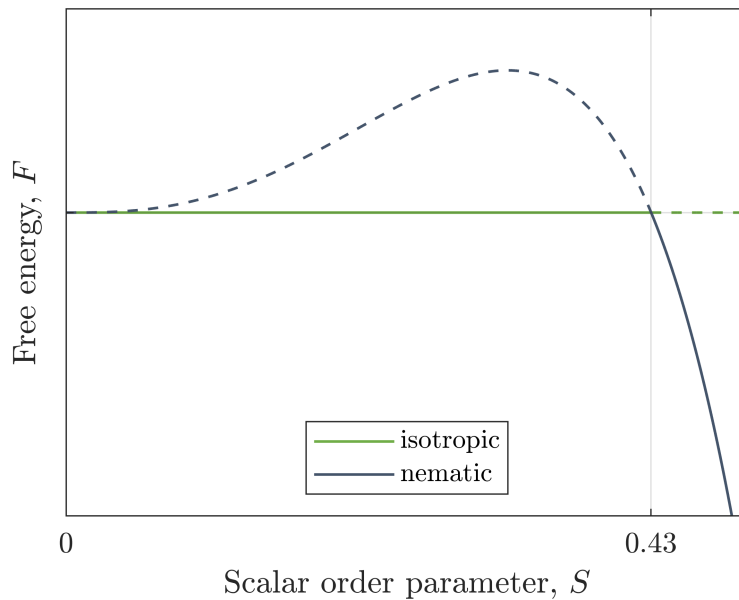


Figure 1.6: Maier-Saupe representation of the thermodynamic free energy. Free energy, F , of the nematic phase (blue) and the isotropic phase (green) as a function of the nematic scalar order parameter, S . Globally stable solutions are indicated by solid lines.

1.2 Continuum description

1.2.1 Nematic order tensor

So far, we have considered the defining features of nematic liquid crystal phases in the form of the director and the scalar order parameter by assuming cylindrical symmetry. In principle, we can construct a cuboid-shaped eigenframe by considering a set of three mutually orthogonal directors, \mathbf{l} , \mathbf{m} and \mathbf{n} , to represent a biaxial nematic phase. To describe these properties in the continuum sense, we can represent the nematic phase by a traceless order tensor

$$Q_{ij} = l_i l_j \lambda_1 + m_i m_j \lambda_2 + n_i n_j \lambda_3, \quad (1.16)$$

where λ_k are the eigenvalues of the system. Since Q_{ij} is traceless, we can simplify the above expression to

$$Q_{ij} = S \left(n_i n_j - \frac{\delta_{ij}}{3} \right) + \frac{P}{3} \left(m_i m_j - l_i l_j \right), \quad (1.17)$$

where $S = \frac{3}{2}\lambda_3$ is the uniaxial order parameter, given by Equation (1.3), $P = \frac{3}{2}(\lambda_3 + 2\lambda_2)$ the biaxial order parameter and δ_{ij} is the Kronecker delta.^[2,13,37,38] Both S and P can vary as a function of temperature and local distortion of the director. For simplicity, we will assume that all physical properties of nematic liquid crystals have cylindrical symmetry and that $P = 0$. This is a common assumption in the vast majority of studies, excluding those that specifically focus on studying biaxial effects and defect cores. However, we will discuss biaxiality and its effects on the physical properties of SmC liquid crystals.

1.2.2 Landau phase transition

An alternative way of characterising phase transitions and equilibrium properties of liquid crystals is to consider a phenomenological thermodynamic free energy density, f_t , as a Taylor series expansion of the order parameters. This can express this as

$$f_t = f_0 + \frac{1}{2}A Q_{ij} Q_{ij} + \frac{1}{3}B Q_{ij} Q_{jk} Q_{ki} + \frac{1}{4}C (Q_{ij} Q_{ij})^2 + \mathcal{O}(Q^5), \quad (1.18)$$

where f_0 is a reference state and A , B and C are functions of temperature and pressure. This method was first introduced by Lev Landau and is known as the *Landau theory of phase transitions*.^[39,40] We can assume that if the system is under constant pressure

and close to the phase transition temperature, T_C , then $A = a(T - T_-)$, where T_- is the supercooling temperature. To ensure that the free energy is bounded from below, it is necessary to have a positive fourth order coefficient, $C > 0$. In the previous section we have established that the nematic-isotropic phase transition is of the first order kind. Therefore, we must incorporate a non-zero value of B . From this, we can see that the expansion of f_t up to the fourth power of S is necessary and sufficient for describing the uniaxial nematic phase from a phenomenological point of view.

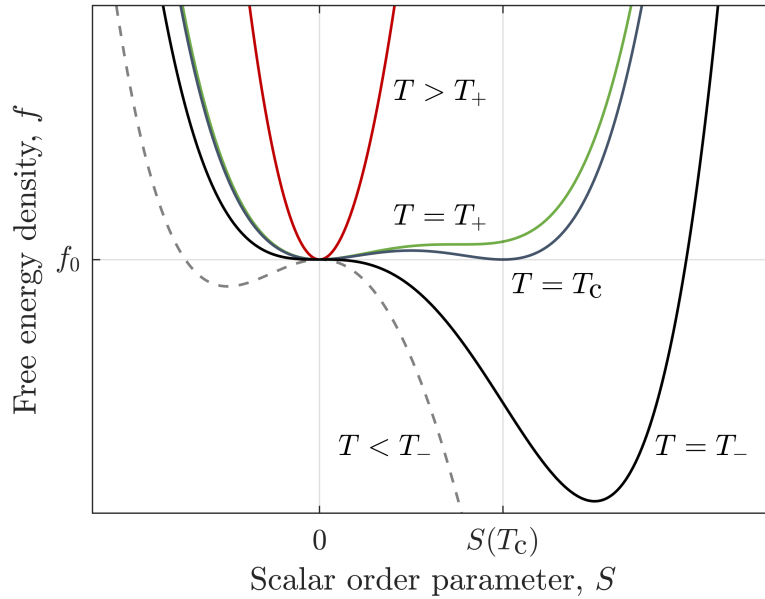


Figure 1.7: Landau representation of the thermodynamic free energy density, f_t , as a function of the uniaxial scalar order parameter, S , for a selection of temperatures, T . Here, T_C , T_- and T_+ represent the phase transition temperature, the supercooling temperature and the superheating temperature, respectively.

Evaluating the stationary points of Equation (1.18) allows us to find the equilibrium (or *bulk*) scalar order parameter to be

$$S_e = \frac{-B + \sqrt{B^2 - 24AC}}{4C}. \quad (1.19)$$

Comparing $f_t(S_e)$ to the trivial solution and performing the second derivative test for each of the characteristic temperatures allows us to determine the stability properties of the system.^[2] From this, we can see that the nematic phase is globally stable for $A < A(T_C) = \frac{B^2}{27C}$, metastable for $A(T_C) \leq A \leq A(T_+) = \frac{B^2}{24C}$ and does not exist for $A > A(T_+)$, where T_+ is the superheating temperature. For $A < 0$, a negative

order parameter distribution (see Figure 1.5) becomes locally stable with respect to S (unstable with respect to P), although the stationary point at $S > 0$ corresponds to the global minimum of the system. The dependence of f on T and S is shown in Figure 1.7, which illustrates its above mentioned special cases.

1.2.3 Elasticity

As a direct consequence of their anisotropic nature, liquid crystals exhibit elastic resistance to deformations of the director field. This manifests itself as a distortion free energy density, f_d , consisting of a set of deformation modes, weighted by their corresponding *elastic constants* (typically measured in pN). It should be noted that liquid crystals are also highly susceptible to flows and elasticity is coupled to the Navier-Stokes equations,^[38,41] which will not be studied in this thesis.

The most natural way to construct f_d is to consider the vector representation of the director and analyse its primary deformation modes. The first step is to assume a uniform director field, and add a small perturbation by expanding it as a Taylor series of its spatial gradients, $n_i(\mathbf{x}) = n_i(\mathbf{0}) + n_{i,j}(\mathbf{0})x_j + \mathcal{O}(|\mathbf{x}|^2)$, where $n_{i,j} = \partial n_i / \partial x_j$. By penalising distortion, we can write down an expression for its free energy contribution as

$$f_d = k_i a_i + \frac{1}{2} K_{ij} a_i a_j + \dots,$$

where k_i and K_{ij} represent elastic constants and a_i represents the vectorisation of $n_{i,j}$. Through a series of symmetry arguments for uniaxial nematics, this can be reduced to^[42]

$$f_d = \frac{1}{2} K_1 (\nabla \cdot \mathbf{n})^2 + \frac{1}{2} K_2 (\mathbf{n} \cdot (\nabla \times \mathbf{n}))^2 + \frac{1}{2} K_3 (\mathbf{n} \times (\nabla \times \mathbf{n}))^2 - \frac{1}{2} K_4 \nabla \cdot (\mathbf{n} (\nabla \cdot \mathbf{n}) + \mathbf{n} \times (\nabla \times \mathbf{n})). \quad (1.20)$$

The first three terms of Equation (1.20) correspond to the primary deformation modes in liquid crystals and commonly known as *splay*, *twist* and *bend*, which are illustrated in Figure 1.8. The term corresponding to K_4 is typically labeled as *saddle-splay* and consists of the *splay*, *twist* and *biaxial splay* deformation modes.^[43] Due to the fact that it can be transformed into a surface integral using the *Divergence theorem*, its contribution to the bulk is often assumed to be minimal, especially with strong anchoring on the boundary conditions (BCs). Because of this, and the lack of any substantial experimental measurements, K_4 is typically omitted from liquid crystal models.

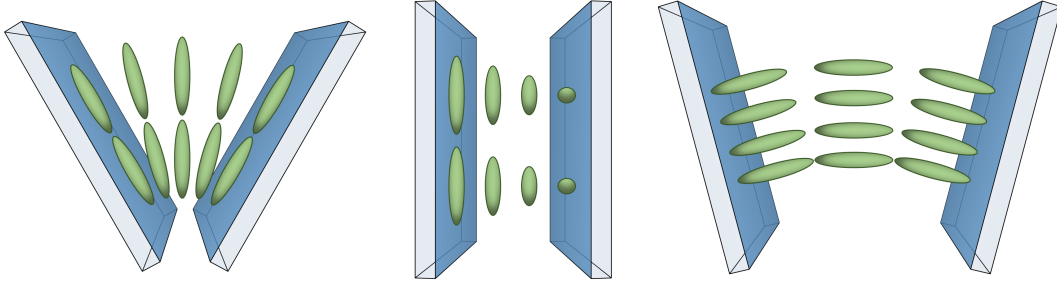


Figure 1.8: Elastic deformations in liquid crystal systems. Illustration of the splay, twist and bend deformation modes of the director in nematic liquid crystals.

The above representation of the elastic free energy has many advantages, ranging from those in finding analytical solutions to having relatively quick numerical solving times. However, its main drawback is that it does not allow us to study systems with changes in the order parameter or those that require \mathbf{n} and $-\mathbf{n}$ to be indistinguishable. For modeling such systems, it is best to consider the order tensor variant of the distortion free energy

$$f_d = \frac{1}{2}L_1(Q_{ij,k})^2 + \frac{1}{2}L_2Q_{ij,j}Q_{ik,k} + \frac{1}{2}L_3Q_{lk}Q_{ij,l}Q_{ij,k} + \frac{1}{2}L_4Q_{ik,j}Q_{ij,k}, \quad (1.21)$$

where L_i are elastic constants.^[37,38,44,45] For uniaxial systems, the elastic constants between the two representations are related via a linear mapping:

$$\begin{pmatrix} L_1 \\ L_2 \\ L_3 \\ L_4 \end{pmatrix} = \frac{1}{S_e^2} \begin{pmatrix} -\frac{1}{6} & \frac{1}{2} & \frac{1}{6} & 0 \\ 1 & -1 & 0 & -1 \\ -\frac{1}{2S_e} & 0 & \frac{1}{2S_e} & 0 \\ 0 & 0 & 0 & 1 \end{pmatrix} \begin{pmatrix} K_1 \\ K_2 \\ K_3 \\ K_4 \end{pmatrix}. \quad (1.22)$$

While there is no easy way to visualise its deformation modes, the order tensor representation of the free energy allows us to model a more complete set of physical phenomena in liquid crystals.

Similar analysis can be performed for the other liquid crystal phases by considering their most prominent deformation modes and penalising them by a corresponding set of elastic constants. For example, in the smectic C phase, the distortion free energy density can be described by a function of \mathbf{a} , \mathbf{c} and their (co-dependent) spatial gradients.^[41,46] We can expect that it is significantly easier to deform \mathbf{c} , which acts as a *polar* director within each layer, than the layers. For this reason, it is common to assume that the

layers remain unchanged in device-friendly operation modes, which we will do later in this thesis.

1.2.4 Boundary conditions

One of the defining features of liquid crystal materials is their responsiveness to BCs. In simple cases, a *Dirichlet* BC can be imposed on a boundary. This defines the preferred orientation of the director, $\mathbf{n} = (\cos \phi \sin \theta, \sin \phi \sin \theta, \cos \theta)$, as well as the preferred order parameter for the order tensor, $Q_{ij} = S(n_i n_j - \delta_{ij}/3)$. Since the LC has to match these conditions exactly, this is typically referred to as a *strong anchoring* of the director. In practice, we can expect that the *anchoring strength* is strongly dependent on the material properties of both the LC and the material that is in contact with it. Therefore, the orientation of the director is held in the preferred orientation by a finite physical force, which can be overcome by an external disturbance or by the elasticity of the LC itself.^[2]

The anisotropic shape of the molecules allows us to control where the director is pointing at the surrounding surfaces by coating them with an *alignment layer* of some suitable material, such as a polymer. The energetic contribution of the surface alignment then extends throughout the bulk of the liquid crystal in order to minimise the overall energy of the system, governed by the viscoelastic properties of the system. In the majority of cases, the surfaces can be coated with a polymer layer to achieve *tangential* boundary conditions (TBC). However, the random nature of the polymer chains causes this alignment to be degenerate. Homogeneous alignment can be achieved by rubbing the polymer layer with a velvet cloth in the desired direction, which is commonly referred to as the *rubbing direction*. This causes local reorientation of the polymer chains, which then interact with the liquid crystal to give a preferred alignment direction. For *normal* boundary conditions (NBC), where the director points perpendicular to the glass surface, the surfaces can be coated using surfactants and detergents (or in some cases polymers). These BCs are illustrated in Figure 1.9. These are the most common alignment techniques for studying liquid crystals, but other means of alignment exist, such as the use of photosensitive polymers.^[7]

Any resistance to reorientation at a given surface, s , can be expressed as an integral of a surface free energy density, f_s . In the simplest form, we can express f_s (to the

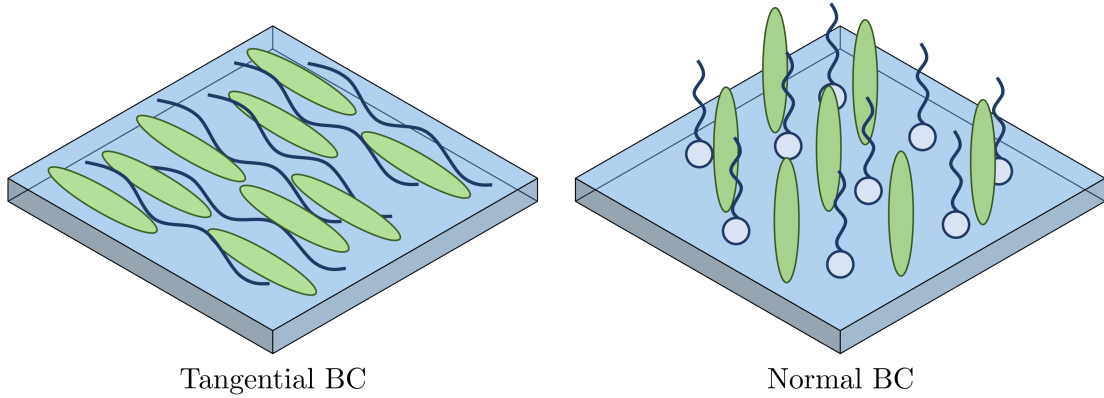


Figure 1.9: Liquid crystal boundary conditions. A schematic diagram, showing common alignment techniques for achieving tangential (left) and normal (right) boundary conditions (BCs) of liquid crystal molecules on glass surfaces. Tangential BCs: rubbing the polymer surface realigns the random chains to point along the rubbing direction, along which the energy of liquid crystal molecules due to orientation is minimized. Normal BCs: polar head groups of surfactants adhere to the glass surface and the aliphatic tails (usually) provide the alignment for liquid crystal molecules.

leading order) as

$$f_s = \frac{1}{2}w_s (1 - (\mathbf{n} \cdot \bar{\mathbf{n}})^2) = \frac{1}{2}w_s (1 - n_i \bar{n}_i n_j \bar{n}_j), \quad (1.23)$$

where w_s is the anchoring strength and $\bar{\mathbf{n}}$ is the preferred director at the surface.^[47] For surfaces with *normal* BCs, this reduces to $\frac{1}{2}w_s \sin^2 \theta$, where θ is measured from the outward pointing unit normal to the surface s . To achieve *degenerate tangential* BCs, Equation (1.23) can be modified to

$$f_s = \frac{1}{2}w_s (\mathbf{n} \cdot \hat{\mathbf{s}})^2 = \frac{1}{2}w_s (n_i \hat{s}_i n_j \hat{s}_j) = \frac{1}{2}w_s \cos^2 \theta. \quad (1.24)$$

where $\hat{\mathbf{s}}$ is the outward pointing unit normal to the surface s . In general, the director can experience different resistances to azimuthal and polar reorientations at its bounding surfaces. To account for this, Equation (1.23) can be decomposed into separate ϕ and θ contributions with individual anchoring strengths, w_ϕ and w_θ , respectively.

Similarly, we have

$$f_s = \frac{1}{2}W_s (Q_{ij} - Q_{ij}^s)^2 \quad (1.25)$$

for the tensor representation, where W_s is the anchoring strength and Q_{ij}^s is the preferred order tensor at the surface.^[48] In this case, to achieve normal BCs, set

$Q_{ij}^s = S_s(\hat{s}_i\hat{s}_j - \delta_{ij}/3)$, where S_s is the preferred order parameter at the surface. Degenerate tangential BCs can be achieved with

$$f_s = W_\theta \left(\tilde{Q}_{ij} - \tilde{Q}_{ij}^\perp \right)^2 + W_S \left(\tilde{Q}_{ij}^2 - S_s^2 \right)^2, \quad (1.26)$$

where $\tilde{Q}_{ij} = Q_{ij} + S\delta_{ij}/3$, $\tilde{Q}_{ij}^\perp = (\delta_{ik} - \hat{s}_i\hat{s}_k)\tilde{Q}_{kl}(\delta_{lj} - \hat{s}_l\hat{s}_j)$, W_θ is the anchoring strength that brings the director to a tangential configuration and W_S is responsible for S achieving its equilibrium value.^[49] An example colour map of the degenerate tangential f_s is shown in Figure 1.10 for $W_\theta = W_S$ and $S_s = S_e = 0.6$, which shows a clear minimum at $\theta = \pi/2$ and $S = S_e$.

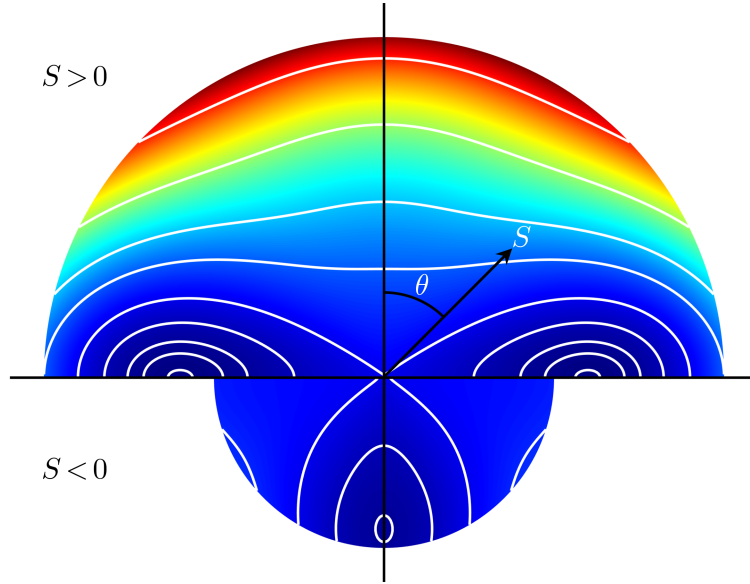


Figure 1.10: Free energy density of tangential boundary conditions. Colour map of the surface free energy density, f_s , illustrating the effects of breaking tangential boundary conditions ($\theta = \pi/2$) and changes in the order parameter, S . The upper part of the colour map corresponds to $S > 0$ and the lower part corresponds to $S < 0$, while the polar angle of the director from the unit normal to the surface, θ , ranges between $-\pi/2$ and $+\pi/2$. When $S = 0$, f_s is independent of θ .

1.2.5 Electric fields

In dielectric fluids, such as liquid crystals, the molecules carry charges that are *free* to move around the immediate space of the individual molecules in the presence of an external electric field, \mathbf{E} . However, they cannot flow through the material on a macroscopic level, as they do in electric conductors such as metals, salts and plasmas.

When the charges are *displaced* from their equilibrium positions (in the opposite direction to \mathbf{E}), dielectric materials acquire electric polarisation, \mathbf{P} . To account for this contribution in Gauss' law, an *electric displacement* field,

$$D_i = \varepsilon_0 E_i + P_i = \varepsilon_0(\delta_{ij} + \chi_{ij}^e)E_j = \varepsilon_0 \varepsilon_{ij} E_j, \quad (1.27)$$

is introduced, where $\varepsilon_0 = 8.854 \text{ pF/m}$ is the permittivity of free space, χ_{ij}^e is the electric susceptibility tensor and ε_{ij} is the relative dielectric permittivity tensor.

The anisotropic nature of liquid crystals extends its effects to its dielectric properties, which manifests itself in the form of an anisotropic eigenframe of ε_{ij} . In turn, an external electric field creates a dielectric torque on the director, $-\mathbf{D} \times \mathbf{E}$, whose effect can be expressed as an electrostatic free energy density $f_e = -\int \mathbf{D} \cdot d\mathbf{E}$. In other words, if the electric field is strong enough to overcome the combined effects of elasticity and BCs in a given liquid crystal system, the director will change its orientation to minimise its total free energy. If we assume that ε_{ij} and Q_{ij} share the same eigenframe and the system is uniaxial, we have

$$f_e = -\frac{1}{2}\varepsilon_0 (\varepsilon_{\perp} \delta_{ij} + \Delta\varepsilon n_i n_j) E_i E_j = -\frac{1}{2}\varepsilon_0 \left(\bar{\varepsilon} \delta_{ij} + \frac{\Delta\varepsilon}{S_e} Q_{ij} \right) E_i E_j, \quad (1.28)$$

where ε_{\perp} and ε_{\parallel} correspond to the eigenvalues of ε_{ij} perpendicular and parallel to the director, respectively, $\bar{\varepsilon} = (2\varepsilon_{\perp} + \varepsilon_{\parallel})/3$ is the average relative permittivity and $\Delta\varepsilon = \varepsilon_{\parallel} - \varepsilon_{\perp}$ is the relative dielectric anisotropy. In general, ε_{ij} has three distinct eigenvalues ε_k with their corresponding eigenvectors $\mathbf{e}^{(k)}$ and the eigenframes of ε_{ij} and Q_{ij} do not necessarily coincide.

So far, we have assumed that the director and all of its associated physical properties are invariant under inversion. However, some systems form phases with reduced symmetry that exhibit an additional *spontaneous* polarisation, \mathcal{P} , whose strength is determined by the molecule's intrinsic dipole moment. This results in an additional contribution to electrostatic free energy density, given by

$$f_e^+ = f_e - \mathcal{P}_i E_i. \quad (1.29)$$

In most cases, the molecules are able to arrange themselves into pairs with opposite dipole orientations (sometimes referred to as *dipole-dipole correlation*) and cancel out the effect of spontaneous polarisation. Therefore, it is necessary for an additional symmetry breaking feature to exist in the liquid crystal system. Since \mathcal{P} can be characterised by

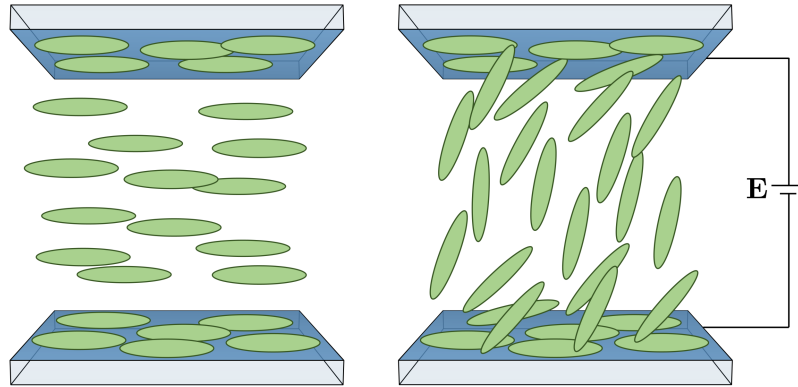


Figure 1.11: Parallel plate capacitor filled with a nematic liquid crystal. A schematic diagram, illustrating the effect of an external electric field, \mathbf{E} , on the orientation of the liquid crystal molecules with positive dielectric anisotropy, $\Delta\epsilon$, in a parallel plate capacitor system.

the $C_{\infty v}$ point group, a given liquid crystal phase can exhibit spontaneous polarisation if and only if its symmetry defining point group is a subset of $C_{\infty v}$ (see Section 1.1.2). In nematics, this can be achieved by composing the phase from pear-shaped or banana-shaped molecules and the effect of \mathcal{P} can be seen whenever the director is in a flexed configuration. For this reason, this is commonly referred to as the *flexoelectricity*.^[50]

Meeting the symmetry requirements for spontaneous polarisation is much easier in the SmC phase. This can be done by introducing chirality (indicated by the * symbol) into the system to reduce its symmetry group to C_2 .^[2] This removes any possibility of polarisation-reducing pairs and allows the existence of \mathcal{P} in the direction of the C_2 axis (defined by $\mathbf{a} \times \mathbf{c}$) in the *ferroelectric* SmC* phase.^[51] When we look at the bulk of the SmC* phase, the contribution of \mathcal{P} from each layer cancels out. This is because the helical nature of the SmC* phase increases its global symmetry to D_{∞} . The helix can be unwound by applying an external electric field (deformed helix mode)^[52] or by constricting the material in a device with a sufficiently thin inner separation gap (surface stabilised state)^[53]. Similarly to the the nematic phase, it is possible to achieve a ferroelectric SmC (and in some special cases, SmA) phase without chirality by using banana-shaped molecules to achieve the C_2 symmetry group.^[54]

1.2.6 Magnetic fields

Similarly, we can expect that liquid crystals can be magnetised by external magnetic fields, \mathbf{H} and have anisotropic magnetic susceptibility, χ_{ij}^m . By making the same assumption as with the electrostatic case, we can express the magnetic contribution to the free energy density as

$$f_m = -\frac{1}{2}\mu_0 (\chi_\perp \delta_{ij} + \Delta\chi n_i n_j) H_i H_j = -\frac{1}{2}\mu_0 \left(\bar{\chi} \delta_{ij} + \frac{\Delta\chi}{S_e} Q_{ij} \right) H_i H_j, \quad (1.30)$$

where $\mu_0 = 1.257 \mu\text{H/m}$ is the permeability of free space, χ_\perp and χ_\parallel correspond to the eigenvalues of χ_{ij}^m perpendicular and parallel to the director, respectively, $\bar{\chi} = (2\chi_\perp + \chi_\parallel)/3$ is the average relative permittivity and $\Delta\chi = \chi_\parallel - \chi_\perp$ is the magnetic susceptibility anisotropy. In most cases, electric fields provide a much more feasible means of controlling liquid crystals than their magnetic field counterparts. This section was included for completeness and magnetic fields will not be considered in the subsequent chapters of this thesis.

1.2.7 Topological defects

Topology is a study of geometrical properties that are preserved by continuous deformations and is mostly associated with pure mathematics.^[55] However, it provides coherence to many physical phenomena that are not always abstract, including cosmology,^[56] topological insulators^[57] and flow fields in fluid mechanics.^[58]

Much like normal mathematical vector fields, director fields are strongly influenced by geometry, BCs and topological rules.^[38,59–61] To illustrate this, let us consider a spherical nematic droplet with radial BCs in its equilibrium state. As we approach the centre of the domain, we observe that the droplet must contain a radial-like singularity in the director field^[62,63] (cf. sink/source in fluid mechanics). Since liquid crystals are comprised of real molecules, singularities in the director field manifest themselves as small isolated regions (typically of the order of tens of nm) with localised melting to the isotropic phase, where $S = 0$ (assuming that any induced biaxiality^[64] is negligible).

Singularities of this nature are commonly referred to as *topological defects* and are described by a property known as the *topological charge* q . This is a measure of the number of turns made by \mathbf{n} in a closed loop or surface around an isolated singularity and remains invariant in a closed system with Dirichlet BCs.^[38,55,65] In general, topological defects can appear as point-like *hedgehogs* and *disclination lines* in liquid crystal

domains and their bounding surfaces. It is worth noting that surface-bound hedgehogs are commonly known as *boojums*. In principle, topological defects in the form of *disclination sheets* can appear in 3D nematic domains, but these are typically unstable and the director relaxes into one of the lower energy counterparts. A selection of 2D examples is illustrated in Figure 1.12, where all defects can be treated as cross-sections of disclination lines and q is characterised by the winding number of the director. Due to the head-tail symmetry of the director, topological defects with half-integer charges can exist in nematic liquid crystals. On the other hand, only defects with integer charges can exist in SmC liquid crystals, because \mathbf{c} is not indistinguishable from $-\mathbf{c}$ (when ignoring sheet dislocations, twist grain boundaries and other defects associated with layers).

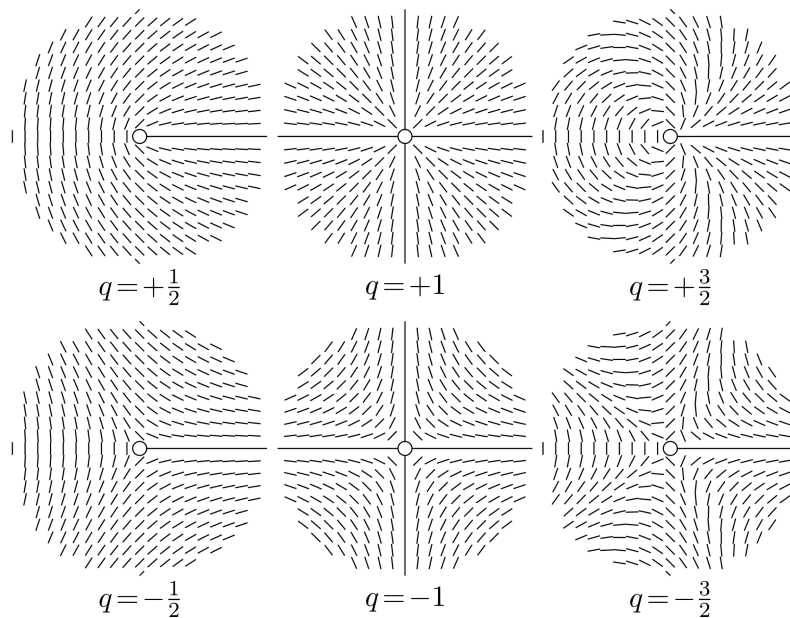


Figure 1.12: Illustration of a selection of 2D topological defects, accompanied by the corresponding director fields.

Existing topological defects cannot be removed from the system without breaking topological rules (or BCs), but they can be continuously deformed into topologically equivalent structures.^[55,60,61,63] For example, a +1 hedgehog is equivalent to a disclination loop with a cross-sectional charge of +1/2. Figure 1.13 illustrates the topological equivalence of topological defects on surfaces of different three-dimensional geometric shapes with tangential BCs. Similarly, if we forcefully introduce a defect into a liquid crystal system, the director field will adapt by creating an accompanying defect of opposite topological charge.^[60,61,63] An early commercial adopter of this feature in

liquid crystal devices is the Zenithal Bistable Display,^[66,67] in which the process of creation and annihilation of nematic defects at structured surfaces is used as a means of switching between two stable configurations of the director. The defects are electrically induced at the point of inflexion on the vertical edges of a grating surface and then separated using the polar response that arises from strong elastic deformations due to the inherent flexoelectricity of the nematic phase^[50,68]

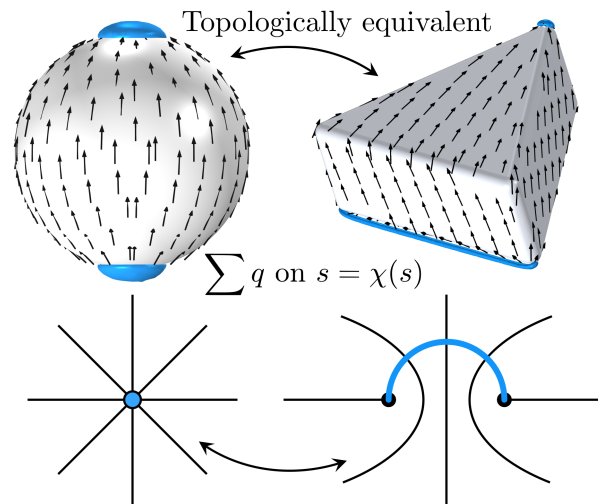


Figure 1.13: Nematic director field and topological defects on particles' surfaces. Illustration showing the topological equivalence of the nematic director fields (black arrows and streamlines) on the surfaces of different 3D geometric shapes with tangential boundary conditions and the corresponding possibilities of the resulting topological defects (blue volumes). This results in two +1 topological defects that move as far away as possible from each other to minimise elastic distortion. Each +1 defect is topologically equivalent to two +1/2 defects, which are also observed experimentally. The sum of all individual topological charges, q , on a given surface, s , must equal to its Euler characteristic, $\chi(s)$, which is equal to 2 for a 2-sphere and other topologically equivalent shapes.

1.3 Solving liquid crystal problems

1.3.1 Minimisation

From the second law of thermodynamics, we know that a closed system with constant entropy seeks a stable equilibrium. In other words, the total free energy of the system

must be minimised. Let us now consider a system in which the total free energy, F , can be described by an integral of some energy density function $f(x, y(x), y'(x))$ over a domain v , such that

$$F = \int_v f(x, y, y') dx. \quad (1.31)$$

Let us assume that y minimises F and consider a small perturbation $y + \epsilon \tilde{y}$, where ϵ is small and \tilde{y} is a continuous function of x . The perturbation must also maintain the original BCs of the system, which requires that $\tilde{y} = 0$ on the boundary of v . To find the governing equations of the system, we can start by considering the first variation of the above integral,

$$\delta F = \left[\frac{d}{d\epsilon} \int_v f(x, y + \epsilon \tilde{y}, y' + \epsilon \tilde{y}') dx \right]_{\epsilon=0}, \quad (1.32)$$

and letting it vanish to ensure that an extremum is achieved. By Leibniz' rule, we have

$$\delta F = \int_v \left[\frac{\partial}{\partial \epsilon} f(x, y + \epsilon \tilde{y}, y' + \epsilon \tilde{y}') \right]_{\epsilon=0} dx. \quad (1.33)$$

By setting $\delta F = 0$, we directly achieve the *weak form* of the governing equations for our system with \tilde{y} acting as the *test function*. To find the *strong form* of the governing equations, we must analyse δF further by expanding its derivatives and using integration by parts:

$$\delta F = \int_v \left(\frac{\partial f}{\partial y} \tilde{y} + \frac{\partial f}{\partial y'} \tilde{y}' \right) dx = \left[\frac{\partial f}{\partial y'} \tilde{y} \right]_v + \int_v \left(\frac{\partial f}{\partial y} - \frac{d}{dx} \frac{\partial f}{\partial y'} \right) \tilde{y} dx. \quad (1.34)$$

From this, we can see that δF vanishes for all \tilde{y} if and only if the final integrand of (1.34) is equal to zero everywhere in v , resulting in the Euler-Lagrange equation

$$\frac{\partial f}{\partial y} - \frac{d}{dx} \frac{\partial f}{\partial y'} = 0. \quad (1.35)$$

Equations (1.33) and (1.35) are equivalent and can be generalised to multi-dimensional, multi-variable systems with higher derivatives.^[15] The strong form allows us to find analytical solutions for simple systems and acts as a powerful tool in solving many physical problems. However, it also requires smoothness and continuity of its solutions at every point of the domain, which can sometimes become its weakness. This can be due to the complexity of the BCs, lack of local smoothness of the physical effects or computational cost associated with the number of variables that are required to construct a suitable approximation. On the other hand, the weak form relaxes the requirements to be met in the integral sense, which can sometimes make more physical sense than the strong form solutions.

1.3.2 Analytical solutions

As we build up our expression for the free energy of a liquid crystal system, the degree of difficulty involved in solving the problem analytically considerably increases. Beyond a selection of special cases, it quickly becomes impossible to find analytical solutions. A common way to simplify the equations is to use a single elastic constant approximation, in which $K_1 = K_2 = K_3 = K$, $K_4 = 0$ and $L_1 = L = \frac{K}{6S^2}$. While this is not necessarily true, it greatly simplifies the governing equations and has proven to be a useful tool in many studies. In most nematics that are comprised of calamitic molecules, the elastic constants differ by less than a factor of 2 from each other and so the one constant approximation provides realistic results (this will be used in Chapter 5). For example, if we consider a 2D system, the vector representation of f_d simplifies to

$$f_d = \frac{1}{2}K \nabla \mathbf{n} : \nabla \mathbf{n} = \frac{1}{2}K n_{i,j} n_{i,j} = \frac{1}{2}K (\nabla \phi)^2, \quad (1.36)$$

where ϕ is the angular coordinate of the director (measured counterclockwise from the x -axis in the x - y plane). If there are no other contributions to the free energy density, we can use Equation (1.35) to find the governing equation for the director. For Equation (1.36), the result is just the Laplace's equation for ϕ :

$$\nabla^2 \phi = 0, \quad (1.37)$$

which we can use to find analytical solutions for simple geometries.

Let us consider a nematic liquid crystal inside a parallel plate capacitor with the following BCs: $\phi(y=0) = \phi_0$ and $\phi(y=1) = \phi_1$. In an ideal world, we can expect that ϕ will be independent of the x coordinate and only vary as a function of y . Solving the Laplace's equation for $\phi(y)$ and applying the BCs gives us $\phi = (\phi_1 - \phi_0)y + \phi_0$. When dealing with slightly more complicated geometries, such as wedges, it is often easier to solve Equation (1.37) using conformal mapping techniques.^[69,70] However, as the geometry acquires more structure defining features, such as additional corners, numerical evaluation becomes necessary for obtaining the solutions.^[71]

1.3.3 Numerical methods

In modern science, numerical solutions are becoming the dominant approach behind finding the solutions to the real world problems. While analytical solutions can provide

us with the outline of the physics behind many liquid crystal systems, numerical methods are required in the majority of cases.

The two most commonly used numerical techniques in liquid crystal simulations are the *finite difference method* (FDM)^[72] and the *finite element method* (FEM),^[73] both of which have their own advantages and disadvantages. The main idea behind using such techniques is to find an approximate solution of the governing equations by breaking up the domain into much smaller elements and linking up their individual solutions to build up the complete picture. From a mathematical point of view, FDM is much easier to implement. The domain is typically discretised as a regular grid and the governing equations are replaced by their linearised counterparts. On the other hand, FEM utilises a more general approach by using polynomials to approximate local physics, which results in higher quality approximations between elements. The domain is approximated by a mesh of triangular or tetrahedral *elements*, which gives us greater flexibility when defining complicated geometries. In particular, the elements can be selectively refined in regions that require greater accuracy while maintaining a coarse mesh elsewhere. Consequently, all boundaries are directly approximated by the boundaries of the adjacent finite elements, which removes any ambiguity associated with defining BCs in FDM.

In this thesis, we will use commercial FEM software (COMSOL Multiphysics) to perform stationary and time-dependent studies on nematic liquid crystal systems. In Chapters 4 and 5, we will use the multi-variable version of Equation (1.35) in its multi-dimensional form.

1.3.4 Modelling the parallel plate capacitor

A good but simple example of this is the parallel plate capacitor system from the previous section. Now that we no longer require the one constant approximation, we can find out exactly what happens to the director inside a real device. Let us consider a device with tangential BCs and a constant inner separation gap, d , between the parallel plate electrodes with a potential difference V , where $\phi(y = 0) = 0$ and $\phi(y = d) = 0$, filled with E7 liquid crystal. E7 is a commercial liquid crystal mixture that is nematic at standard room temperature with $K_1 = 10.8$ pN, $K_2 = 6.5$ pN, $K_3 = 17.5$ pN, $\varepsilon_{\perp} = 5.2$ and $\varepsilon_{\parallel} = 19.2$.^[74] As before, we can expect that ϕ is a function of y only. Therefore, we can exclude the contribution of K_2 (twist) from the free energy density. Combining

Equation (1.20) and Equation (1.28) results in

$$f = \frac{1}{2} \left(\frac{d\phi}{dy} \right)^2 (K_1 \cos^2 \phi + K_3 \sin^2 \phi) - \frac{1}{2} \epsilon_0 (\epsilon_{\perp} + \Delta\epsilon \sin^2 \phi) \left(\frac{dV}{dy} \right)^2, \quad (1.38)$$

which can be prepared for numerical evaluation using either Equation (1.33) or Equation (1.35) in their multi-variable form. Plotting a colour map of ϕ as a function of y and V can provide us with valuable insight about the physics of such devices. From Figure 1.14, we can see that ϕ remains unaffected by the voltage until it reaches a critical value, V_c . This effect is commonly known as the *Frederiks transition*, which was originally studied using magnetic fields.^[75] At the critical point, the electrostatic force overpowers the elastic resistance of the director and $\phi = 0$ becomes unstable. The director begins to tilt at the midpoint of the system, $y = d/2$, where the effects of the BCs are least important.

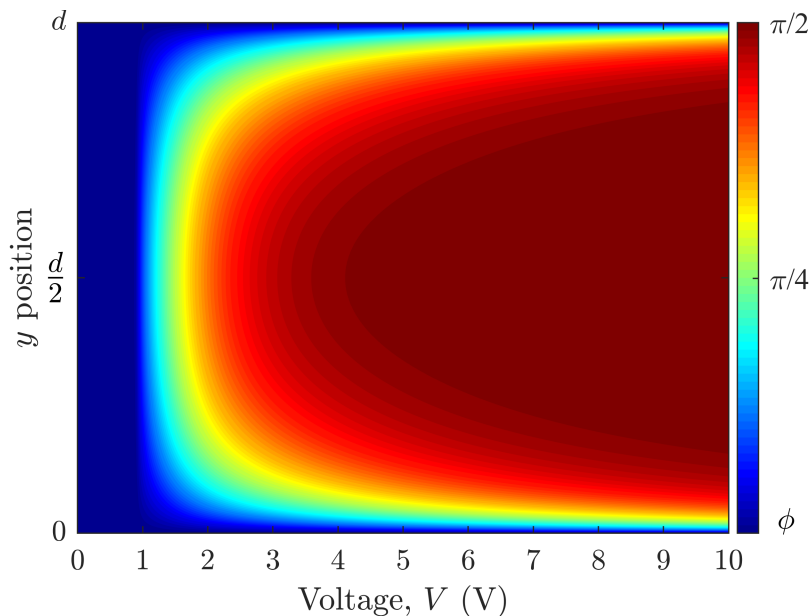


Figure 1.14: Director orientation in a parallel plate capacitor. Colour map of the director's out of plane tilt angle, ϕ , as a function of voltage, V , and position $y \in [0, d]$ inside a parallel plate capacitor system with E7 liquid crystal and tangential boundary conditions ($\phi = 0$). Blue colour corresponds to $\phi = 0$, green to $\phi = \pi/4$ and red to $\phi = \pi/2$. (Results were obtained through a finite element method simulation.)

The critical voltage can be found by expressing $\phi(y)$ as a Fourier series, subject to symmetry about the midpoint and the original BCs of the system, and evaluating the the free energy of the system. Because $\phi = 0$ throughout the system just before the

critical point, we can assume that $E = V/d$ and only consider the leading term of its expansion

$$\phi(y) = 0 + \tilde{\phi} \sin\left(\frac{\pi y}{d}\right) + \mathcal{O}(\tilde{\phi}^2), \quad (1.39)$$

where $\tilde{\phi} \ll 1$. Substituting this into Equation (1.38) and integrating with respect to y gives

$$\begin{aligned} F &= F_0 + \frac{1}{2}\tilde{\phi}^2 \int_0^d \left(\frac{\pi^2}{d^2} K_1 \cos^2\left(\frac{\pi y}{d}\right) - \varepsilon \Delta \varepsilon E^2 \sin^2\left(\frac{\pi y}{d}\right) \right) dy \\ &= F_0 + \frac{d}{4}\tilde{\phi}^2 \left(\frac{\pi^2}{d^2} K_1 - \varepsilon_0 \Delta \varepsilon E^2 \right), \end{aligned} \quad (1.40)$$

where F_0 is the director independent free energy of the system. Beyond the critical point, $F < F_0$ for all $\tilde{\phi}$ and therefore, its multiplier in (1.40) must be negative. From this, we find that

$$V_c = E_c d = \pi \sqrt{\frac{K_1}{\varepsilon_0 |\Delta \varepsilon|}}, \quad (1.41)$$

which matches up with our numerical simulation for E7 exactly, where $V_c = 0.93$ V.

Of course, we have to first measure the physical properties of liquid crystals before we can model them numerically. In principle, Figure 1.14 can be created experimentally using any of a variety of techniques such as *fluorescence polarised confocal microscopy*,^[76] which requires the addition of a small amount of suitably chosen fluorescent dye. However, it is significantly easier to measure the effective dielectric permittivity of the system as a function of voltage and fit the data numerically to extract its principal permittivities and elastic constants.^[77]

1.4 Thesis road map

In this chapter, we have provided an introduction to the physics of liquid crystals. The aim of this section is to provide a road map for the rest of the thesis.

In Chapter 2, we will discuss the general experimental methods used to obtain the results in this thesis.

In Chapter 3, we will consider the effects of monoclinic symmetry on observable properties of biaxial liquid crystal phases. In particular, we will use the inherent symmetry properties of the smectic-C phase to measure the disassociation angle of its optical and dielectric eigenframes.

In Chapter 4, we will use double emulsions of water droplets inside radial nematic liquid crystal droplets to form various structures, ranging from linear chains to three-dimensional fractal structures. Through a series of symmetry arguments and numerical modelling, we will describe the formation mechanism of fractal liquid crystal colloids. This chapter will introduce the concepts of fractal systems and colloidal self-assembly in nematic liquid crystals.

In Chapter 5, we will combine experiments with numerical modelling to investigate effects of geometric symmetry on electrically induced rotation and non-reciprocal motion of colloidal particles in parallel plate capacitor cells filled with nematic liquid crystals. Finally, Chapter 6 will provide an overview of the results presented in this thesis by reviewing the key findings from each chapter and discussing the outlook of future projects.

Chapter 2

Methodology

2.1 Polarising optical microscopy

When polarised light passes through a birefringent material, it experiences refraction and splits into two orthogonal components, one parallel to the extraordinary axis of the material and the other perpendicular to it. Due to the birefringent nature of the material, the two components will travel through the material at different speeds and accumulate a phase difference, given by

$$\Gamma = \frac{2\pi}{\lambda} \Delta n d, \quad (2.1)$$

where λ is the wavelength of light, Δn is the birefringence and d is the distance travelled of through the birefringent material. If the resulting light waves pass through another polariser, only the components that are parallel to the polariser pass through. Since most liquid crystals are birefringent, a polarising compound microscope is an essential tool for most liquid crystal scientists. In general, the sample appears black if its optic axis is perpendicular to at least one of the crossed polarisers. This allows us to determine the orientation of the director in Chapter 3 by rotating the sample such that the light passing through the region of interest is minimised.

Additional optical retarders with a known birefringence are often used in conjunction with a set of crossed linear polarisers to determine the director's orientation. Figure 2.1 shows a simulated image of a liquid crystal director profile around two optically isotropic cylinders with normal BCs between crossed polarisers and a full-waveplate optical retarder inserted at 45° to both polarisers. This adds to the overall retardance of the system when the extraordinary axis of the optical retarder is parallel to the director and subtracts when it is perpendicular, which can be used to distinguish between the

two orientations of the director. Birefringence can be measured by inserting a tilting compensator (usually made from a well characterised birefringent material, such as rutile) between a set of crossed polarisers such that the projection of its extraordinary axis is perpendicular to that of the liquid crystal.

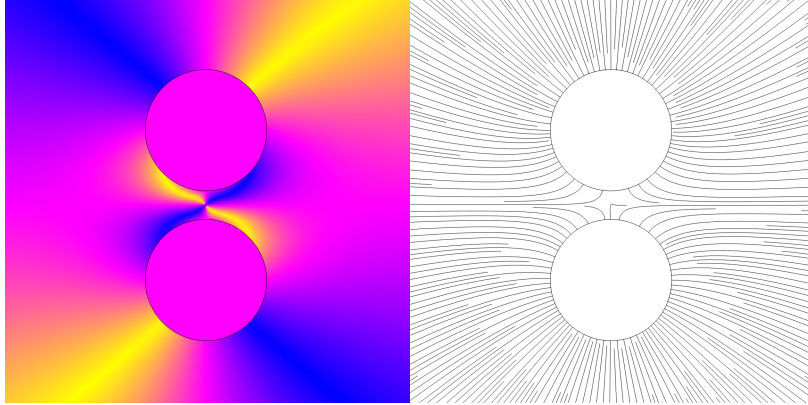


Figure 2.1: Director profile around two neighbouring inclusions. Two cylinders between crossed polarisers with a full wave plate on the left and the corresponding director profile on the right. Crossed polarisers at South-North and West-East orientations; full-waveplate at NW-SE orientation of the extraordinary axis. (Results were obtained through a finite element method simulation.)

2.2 Confocal microscopy

In this thesis we also use confocal microscopy to capture images of three-dimensional structures with improved resolution in Chapter 4 and confirm the depth of suspended particles in Chapter 5. In contrast to the conventional microscope design, confocal microscopes utilise a point source laser to illuminate the sample and an additional pinhole in front of the detector. Consequently, only the information within a small distance away from the focal plane is observed by the detector. This allows us to build up a three-dimensional image by combining a series of two-dimensional slices taken at different depths of the sample. Figure 2.2 shows the three-dimensional positioning of a triangular prism that was suspended within a liquid crystal sample, which was doped with a small amount of Nile red fluorescent dopant. In Chapter 5, we assume that the suspended particles remain in the centre of the parallel plate cells, which was confirmed by confocal microscopy. This remains true for a short period of time after filling the

cells but can be reset by applying an external voltage.

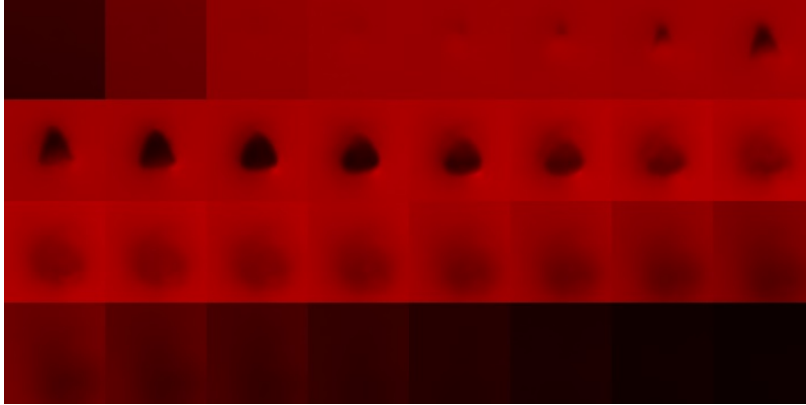


Figure 2.2: Montage of a series of confocal fluorescence images, scanned through the depth of the sample. Red regions correspond to the fluorescence of the Nile red dye in the nematic liquid crystal. Black regions correspond to the suspended triangular prism within the sample. (Imaging performed with Antariksh Saxena)

2.3 Dielectric spectroscopy

When an alternating current is applied across a dielectric circuit, it follows the path of lowest impedance, Z . Dielectric response of liquid crystal materials is typically measured by an impedance analyser as a function of frequency, ω . In practice, this process measures the combined effects of the individual components that make up the circuit of a given sample. In the case of the standard parallel plate capacitor cells (discussed in Section 1.3.4), the total impedance is given by

$$Z_{\text{cell}} = R_e + \frac{R_a - i\omega C_a R_a^2}{1 + (\omega C_a R_a)^2} + \frac{R - i\omega C R^2}{1 + (\omega C R)^2}, \quad (2.2)$$

where R_e is resistance of the wires, R_a is the resistance of the alignment layers, C_a is their capacitance, R is the resistance of the liquid crystal layer and C is its capacitance. Typically, the empty cell impedance is measured before filling it with a liquid crystal material. This allow us to isolate the dielectric response of the liquid crystal and measure its physical properties. In this thesis, we are mostly concerned with measurements of relative permittivity, $\varepsilon^* = \varepsilon' - i\varepsilon''$, whose real and imaginary components are given by

$$\varepsilon' = \frac{\text{Im}(\tilde{Z})}{\omega C_0 (\text{Re}(\tilde{Z})^2 + \text{Im}(\tilde{Z})^2)} \quad \text{and,} \quad \varepsilon'' = \frac{\text{Re}(\tilde{Z})}{\omega C_0 (\text{Re}(\tilde{Z})^2 + \text{Im}(\tilde{Z})^2)}, \quad (2.3)$$

where \tilde{Z} is the impedance contribution of the liquid crystal and C_0 is the empty cell capacitance. The liquid crystal layer can be treated as a leaky capacitor with an additional *equivalent series resistance* that contributes to the loss of the electromagnetic energy of the system (usually as heat). This can be characterised by a frequency dependent dissipation factor (dielectric loss), given by $\varepsilon''/\varepsilon'$. Naturally, we aim to minimise dielectric loss for device friendly applications. This can be achieved by selecting an appropriate frequency range, which is typically between 1 kHz and 1 MHz for liquid crystals in devices with ITO conductors.^[7,12] In such cases, calculating the real component of the relative dielectric permittivity is simplified to $\varepsilon = C/C_0$.

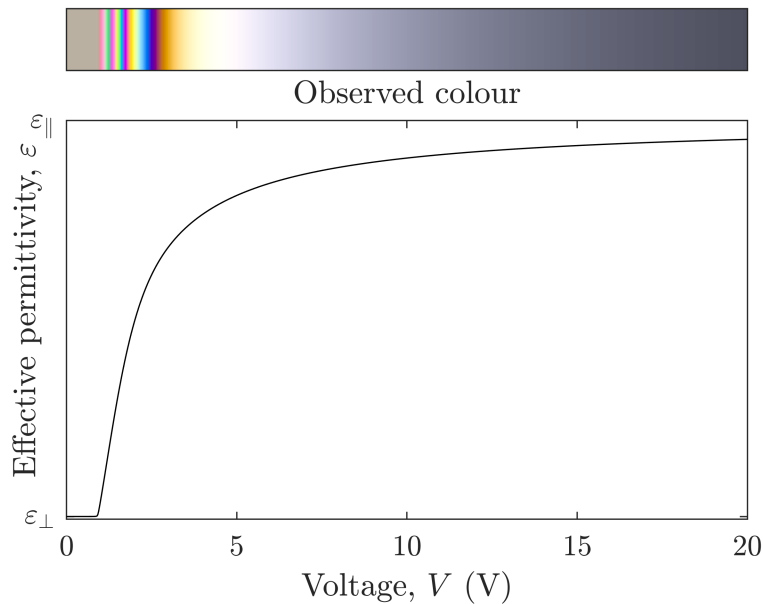


Figure 2.3: Effective permittivity and optical retardation in a parallel plate capacitor. Optical and dielectric effects of voltage on the measured dielectric permittivity, ε , as a function of voltage, V , inside a parallel plate capacitor with uniform tangential BCs and an inner separation gap of $10 \mu\text{m}$, filled with E7 liquid crystal (bottom) accompanied by the corresponding colour when observed through a cross polarising optical microscope (top).

Figure 2.3 shows the results of a typical experiment for E7 in a parallel plate capacitor with uniform tangential BCs and an inner separation gap of $10 \mu\text{m}$. As expected, ε remains at a constant value, equal to ε_{\perp} , until a critical voltage of 0.93 V is reached. Subsequently, the director begins to rotate within the cell to align with the electric field, ε increases and tends to an infinite voltage asymptote of ε_{\parallel} . When

this process is observed through a cross-polarising optical microscope, we can observe a corresponding colour sequence from the changing effective birefringence of the sample. This is illustrated in the top part of Figure 2.3. Here, the retardation was calculated using numerical integration of $\Delta n(\phi)$ through the y coordinate of Figure 1.14, with $n_{\perp} = 1.53$ $n_{\parallel} = 1.76$,^[78] and evaluated according to the *gamma corrected* Michel-Lévy birefringence chart^[79] to give a realistic visual representation. This calculation assumes that reflection, absorption and dispersion of light within the sample are negligible. However, if the sample is uniformly illuminated by a large light source at normal incidence (such as the microscope in our example), then the optical retardation can be tracked through the sample. In such cases, Jones matrices are often used to track the retardation of light as it passes through the sample.^[7]

2.4 Microfluidics

Microfluidics is the most common technique for producing droplets on the micrometre scale. In Chapter 4, we will use this technique to create double emulsion systems of small water droplets inside radial nematic droplets. To prevent the nematic droplets from coalescing and make the formation process easier, a small amount of surfactant is typically added to the water solution. In our study we add 0.5% (with respect to mass) of hexadecyltrimethylammonium bromide (CTAB) to purified water to stabilise the emulsions and provide normal BCs at the interfaces. The flow rate is typically controlled by a set of high precision syringe pumps that push the fluids through plastic tubes into the microfluidics device. First, the channel is slowly flooded with the outer fluid, pushing the air out of the system to ensure that the pressure can be well controlled by flow rate. Once the system is filled with the outer fluid, the inner fluid is pushed towards the junction, where the outer fluid flow pinches off the inner fluid into regular droplets. Each system has its own unique properties and the flow rates are usually adjusted on the case by case basis to find a stable regime. Following this, the flow rate of the outer fluid is fixed and the flow rate of the inner fluid is adjusted to achieve the desired droplet size. Figure 2.4 shows the typical dependence of the microfluidically generated droplet radius as a function of the flow rate ratio between the inner and the outer fluids. We can see increasing the flow rate of the inner fluid results in the creation of larger droplets. The formation process of nematic liquid crystal droplets

in water is illustrated in Figure 2.5a. This process can be repeated to create double emulsions by stacking a sequence of junctions with alternating inner and outer fluids or by using using an inner fluid that already contains the smaller emulsions. Figures 2.5b and 2.5c show the creation process of double emulsion systems before and after the final emulsification step, respectively.

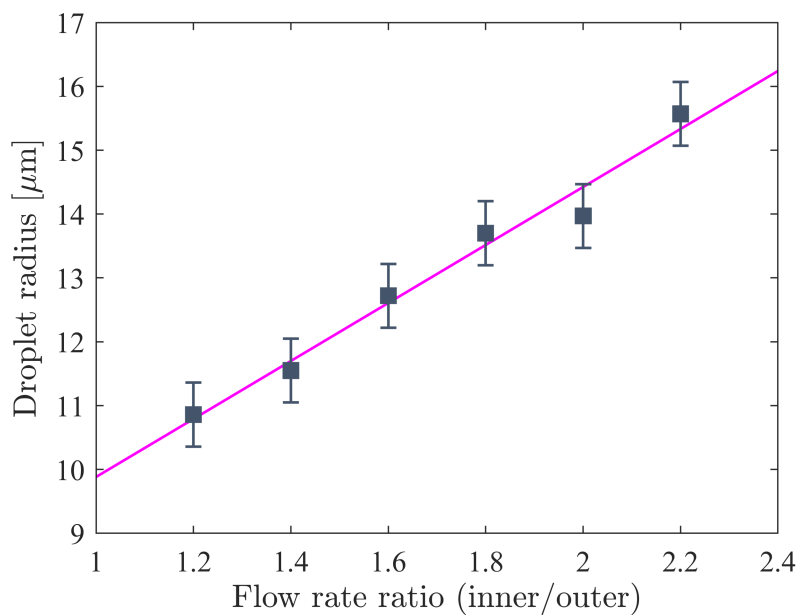


Figure 2.4: Radius of microfluidically generated droplets as a function of the flow rate ratio between the inner and the outer fluids. Outer flow rate was maintained at a constant value of $25 \mu\text{L/h}$. (Data obtained by Clare Verduyn, under the supervision of Nikita V. Solodkov.)

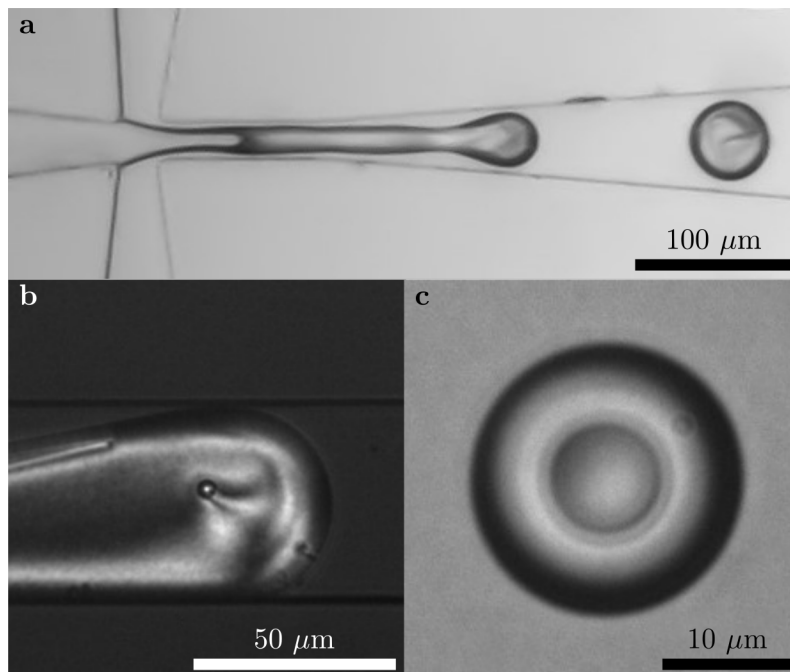


Figure 2.5: Microfluidics of double emulsions. Single and double emulsion microfluidics of E7 and water solution containing a small amount of CTAB surfactant. (a) shows the creation process of nematic liquid crystal droplets at a typical microfluidics junction. (b) shows a $4 \mu\text{m}$ water droplet floating inside a soon to be formed nematic liquid crystal droplet (observed under crossed polarisers). (c) shows a double emulsion consisting of a water droplet inside a nematic liquid crystal droplet.

Chapter 3

Effects of monoclinic symmetry on the properties of biaxial liquid crystals

This chapter reproduces the study from “Effects of monoclinic symmetry on the properties of biaxial liquid crystals”, published in *Physical Review E*, vol. 97, no. 4, p. 042702, 2018,^[80] which partially encapsulate the results from “Alignment and electro-optical properties of SmC* with direct transition to N* phases”, published in *Molecular Crystals and Liquid Crystals*, vol. 647, no. 1, p. 162, 2017.^[81] Nikita V. Solodkov and J. Cliff Jones designed the research. Nikita V. Solodkov performed the research. Mamatha Nagaraj and J. Cliff Jones supervised the project.

3.1 Introduction

Tilted smectic liquid crystal phases such as the smectic-C phase seen in calamitic liquid crystals are usually treated using the assumption of biaxial orthorhombic symmetry (D_{2h} and D_2). However, the smectic-C phase has monoclinic symmetry (C_{2h} and C_2), thereby allowing disassociation of the principal optic and dielectric axes based on symmetry and invariance principles, described in Sections 1.1.2 and 1.1.3. The goal of this work described in this chapter is to present experimental evidence for the effects of monoclinic symmetry of the SmC phase on its dielectric and optical properties. This is demonstrated here by comparing optical and dielectric measurements for two materials with highly first order direct transitions from nematic to smectic-C phases. Additionally,

we measure the extent of monoclinic behavior by interpreting it as a separation of cone angles for each observable property. The results show a high difference between the orientations of optical and dielectric eigenframes, which is interpreted as the existence of two distinct cone angles for optical and dielectric frequencies. Understanding the symmetry properties of a simple SmC system is a major stepping stone in understanding monoclinic symmetry in new non-calamitic liquid crystals, such as those with bent cores.

Due to fast switching speeds, ferroelectric smectic-C* materials are important for fast modulators and LCoS devices, where the dielectric biaxiality influences device operation, particularly at high voltages. When compared to the dielectric torque used to switch NLC based devices, the ferroelectric torque is usually much stronger, allowing much faster switching times at lower voltages. This is because ferroelectric liquid crystals exhibit a polar response to electric fields, which additionally allows both the “on” and the “off” switching mechanisms to be driven electrically. For this reason, ferroelectric SmC liquid crystals have been used in various applications.^[52,53,82] Electro-optic behavior at high electric fields and frequencies beyond that of ferroelectric switching is dominated by the dielectric biaxiality.^[82,83] Knowing the dielectric biaxiality is critical for understanding the behavior of devices, from fast electro-optical shutters to high resolution liquid crystal on silicon spatial light modulators.

3.2 Monoclinic Symmetry and the Dielectric Tensor

Assuming orthorhombic symmetry between optical and permittivity axes allows the individual permittivity components to be calculated using the combination of optical and dielectric measurements.^[83] This requires permittivity measurements in geometries with tangential boundary conditions (TBC) and normal boundary conditions (NBC), ε_p and ε_h , respectively. Two similar methods were previously used to calculate the principal permittivity components in SmC* materials: using electric fields to unwind the helical structure^[84,85] and using surface interactions in devices with sufficiently thin containment regions to permanently suppress the helix formation^[83].

Since the SmC phase has monoclinic symmetry, the principal dielectric axes do not necessarily coincide with the optical axes. However, all previous measurements of the biaxial electric permittivities have used the optical cone angle^[83,85]. The monoclinic order parameter will grow continuously from zero below the transition. Hence, the

dispersion of the symmetry axes will also increase significantly. Thus, differences between the monoclinic physical properties may be more difficult to measure experimentally. By continuity principles, the monoclinic properties will appear gradually for second order transitions (e.g. SmA to SmC) and therefore, monoclinic properties may not have a significant effect and lie within the experimental error. In such cases, an orthorhombic approximation is appropriate close to the phase transitions. However, if the phase transition is highly first order (e.g. NLC to SmC, where the biaxiality has a discontinuous jump), then we expect the monoclinic properties to have a more pronounced contribution and monoclinic symmetry must be considered when studying dielectric properties of such materials.

As the sample is cooled into and through the SmC phase, the smectic layer spacing typically shrinks, resulting in the layers tilting to a chevron structure in geometries with tangential BCs.^[86] Typical materials that undergo the SmA to SmC phase transition lead to a ratio of layer tilt δ to the cone angle θ_c that is roughly constant and around 0.85^[82]. This has been explained using the argument of monoclinic symmetry of the SmC(*) phase, where the ratio corresponds to that of the steric and polarizability cone angles. However, in liquid crystals that exhibit a first order NLC to SmC phase transition directly, layers initially form with an in-plane tilt component in systems with homogeneous tangential boundary conditions. This can be approximated by the steric cone angle, which interacts with the surfaces of the system. The first order transition leads to less layer shrinkage and correspondingly lower values of δ . In such cases, asymptotic discontinuities arise whenever a SmC material exhibits layer tilts that satisfy

$$\delta \leq \delta_c = \arcsin \left(|\sin \theta_c| \sqrt{\frac{\cos 2\theta_c}{2 - 3 \sin^2 \theta_c}} \right), \quad (3.1)$$

where δ_c is the critical layer tilt at which the system of linear equations described in Ref.^[83] becomes linearly dependent, resulting in unphysical solutions. Measurements of the biaxial permittivities for materials with an NLC to SmC phase sequence have not been reported before, partly because of this issue.

Consideration of energy conservation and time reversal symmetry can be used to show that the dielectric tensor ε_{ij} is always symmetric.^[40,87] Therefore, we can use the *spectral theorem* for symmetric matrices, which states that a symmetric matrix is

always orthogonally diagonalisable^[88] such that

$$\begin{pmatrix} \varepsilon_1 & 0 & 0 \\ 0 & \varepsilon_2 & 0 \\ 0 & 0 & \varepsilon_3 \end{pmatrix} = \begin{pmatrix} \mathbf{e}^{(1)} & \mathbf{e}^{(2)} & \mathbf{e}^{(3)} \end{pmatrix}^T \varepsilon_{ij} \begin{pmatrix} \mathbf{e}^{(1)} & \mathbf{e}^{(2)} & \mathbf{e}^{(3)} \end{pmatrix}, \quad (3.2)$$

where ε_k are the eigenvalues and $\mathbf{e}^{(k)}$ are the eigenvectors of ε_{ij} , for $k = 1, 2, 3$. The eigenvalues of the dielectric tensor are the *principal* dielectric permittivities and the eigenvectors are the principal dielectric axes, such that $\mathbf{e}^{(3)}$ is the *dielectric director*. By applying invariance principles along the C_2 axis, we can deduce that there exists a principal dielectric axis $\mathbf{e}^{(2)}$ parallel to C_2 , which coincides with analogous optic and other principal axes. The lack of orthorhombic symmetry results in a decoupling of the eigenvectors of permittivity and optics by rotating one with respect to another about the common C_2 axis. This asymmetry can be interpreted as a difference between the optical and dielectric cone angles

$$\partial\theta = \theta_o - \theta_\varepsilon, \quad (3.3)$$

where θ_o and θ_ε are the cone angles generated by the optical and dielectric axes, respectively. Figures 3.1 and 3.2 illustrate the diagonalisation process and two cone angles with respect to the layer normal, respectively, and indicate the principal optical and permittivity axes. In principle, there can exist a distinct cone angle for every observable physical property in SmC liquid crystals, such as magnetic susceptibility and steric alignment. It is also worth noting that $\partial\theta$ is likely to be frequency dependent and have a number of relaxation modes.

3.3 Governing Equations

When measuring relative permittivities of the SmC phase in the laboratory frame of reference (x, y, z) along the $(0, 1, 0)$ direction, we measure $\varepsilon = \varepsilon_{22}$. Without loss of generality, we can assume that the director is rotated by an angle θ_c away from \mathbf{z} , by an angle ϕ around \mathbf{z} and by an angle δ around \mathbf{x} . For the general monoclinic case, $\partial\theta$ is not known and represents the difference between the optical and dielectric cone angles, θ_o and θ_ε , respectively. The result of this is that the measured value of ε consists of an orthorhombic part ε° (the case in which $\partial\theta = 0$) with an additional monoclinic contribution. In the reference frame of the orthorhombic diagonalisation of ε_{ij} , we can

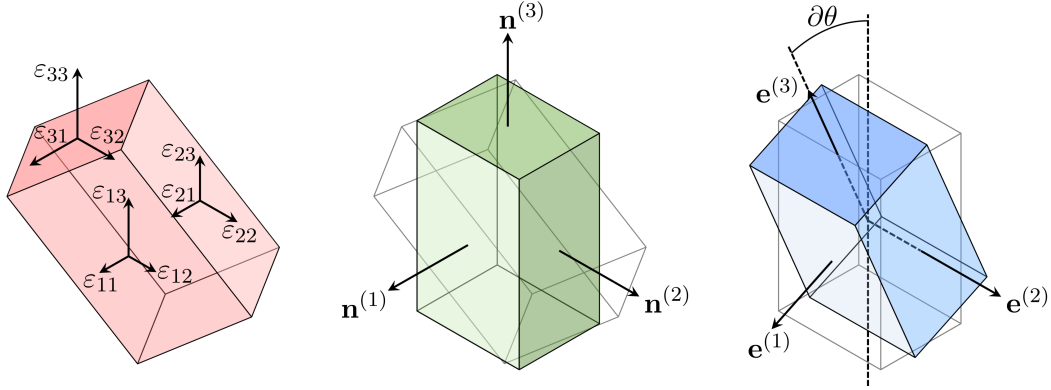


Figure 3.1: Diagonalisation of the relative permittivity tensor. Schematic diagram illustrating the diagonalisation process of the relative permittivity tensor, ε_{ij} , in the orthorhombic case (middle) and the monoclinic case (right).

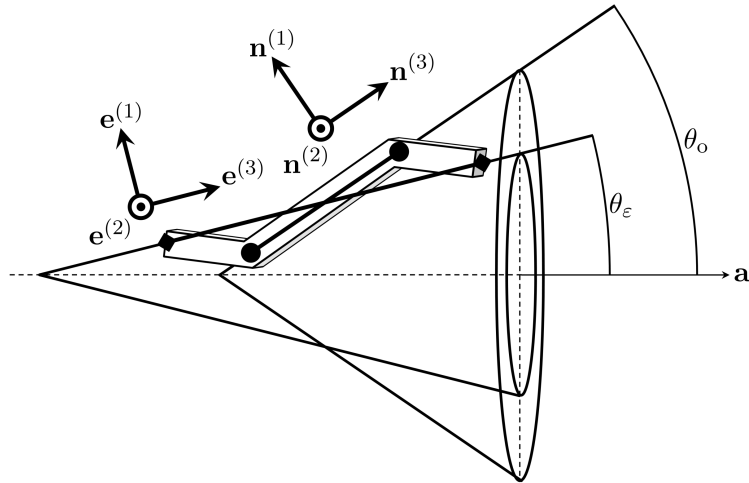


Figure 3.2: Optical and dielectric cone angles. Schematic representation of the assumed average molecular configuration of the SmC phase, illustrating the differences between the principal components of the optical and dielectric axes, indicated by $\mathbf{n}^{(k)}$ and $\mathbf{e}^{(k)}$ (for $k = 1, 2, 3$), respectively. The corresponding cone angles, measured from layer normal \mathbf{a} , are indicated by θ_o and θ_ε .

express this as

$$\varepsilon = \underbrace{\varepsilon_{11} + (\varepsilon_2 - \varepsilon_{11}) \cos^2 \delta \cos^2 \phi + (\varepsilon_{33} - \varepsilon_{11}) \sin^2 \zeta}_{\text{orthorhombic} = \varepsilon^o} + \underbrace{2\varepsilon_{13} \sin \zeta (\cos \delta \sin \phi \cos \theta_c + \sin \delta \sin \theta_c)}_{\text{monoclinic correction}}, \quad (3.4)$$

where the out of plane director tilt, ζ , is given by $\sin \zeta = (\cos \delta \sin \phi \sin \theta_c - \sin \delta \cos \theta_c)$.

A rotation by an angle $\partial\theta$ around the C_2 axis of the phase diagonalizes the dielectric tensor. Therefore, we can choose a different cone angle to be $\theta_\varepsilon = \theta_o - \partial\theta$ and disassociate the other two principal dielectric and optical axes, reducing (3.4) to

$$\varepsilon = \varepsilon_1 + (\varepsilon_2 - \varepsilon_1) \cos^2 \delta \cos^2 \phi + (\varepsilon_3 - \varepsilon_1) \sin^2 \zeta_\varepsilon, \quad (3.5)$$

where ζ_ε now has $\theta_c = \theta_\varepsilon$, while δ and ϕ remain the same. Since we have chosen $\mathbf{e}^{(2)}$ to be in the direction of the C_2 axis of rotation, ε_2 and $(\varepsilon_{11} + \varepsilon_{33})$ are invariant under any rotation about the C_2 axis.

If the material is ferroelectric (see Section 1.2.5), the director can be switched to the side of the cone in the TBC geometry. Consequently, an additional permittivity measurement can be made by applying a DC bias to the sample.^[82] In the fully switched position of the director (when the maximal amount of the C_2 axis points along the field, such that $\phi = 0$ and $\zeta_\varepsilon = \zeta_o = \delta$) the measured permittivity is given by

$$\varepsilon_f = \varepsilon_2 \cos^2 \delta + \varepsilon_h \sin^2 \delta, \quad (3.6)$$

where ε_p and ε_h are the permittivities measured in TBC and NBC geometries, respectively. This allows ε_2 to be calculated directly and reduces the problem to the following three equations:

$$\varepsilon_h = \varepsilon_1 \sin^2 \theta_\varepsilon + \varepsilon_3 \cos^2 \theta_\varepsilon, \quad (3.7)$$

$$\varepsilon_p = \varepsilon_1 (1 - \cos^2 \delta \cos^2 \phi - \sin^2 \zeta_\varepsilon) + \varepsilon_3 \sin^2 \zeta_\varepsilon + \varepsilon_2 \cos^2 \delta \cos^2 \phi, \quad (3.8)$$

$$3\bar{\varepsilon} = \varepsilon_1 + \varepsilon_2 + \varepsilon_3, \quad (3.9)$$

where $\bar{\varepsilon}$ is the mean permittivity, which can be extrapolated from the uniaxial and isotropic phases.^[84] Equation (3.6-3.9) can be solved numerically to find a unique solution for the principal permittivities and the dielectric cone angle. Additionally, these equations remove the restriction due to the discontinuity for $\delta \leq \delta_c$ and allow us to calculate relative permittivities for materials with low δ to θ_c ratios, such as those with direct NLC to SmC phase transitions. In this study, we assume that the director remains uniform throughout the depth of system, which is a reasonable approximation when δ is much smaller than θ_c . In practice, ϕ and ζ can vary within the samples if δ is sufficiently large, such as in materials with a direct SmA to SmC phase transitions.

3.4 Materials and Methods

In this work, we investigate the dielectric and optical properties of two partially fluorinated terphenyl liquid crystals with direct NLC to SmC phase transitions, both of which potentially show highly monoclinic behavior. Compound X^[89] has a strong coupling between the sole dipole moment and the polarizability tensor. On the other hand, compound Y^[90] was chosen because it has multiple dipoles, which are therefore less likely to be orientated along the eigenvectors of its polarizability tensor. Optically measured phase transition temperatures for both materials are presented in Figure 3.3.

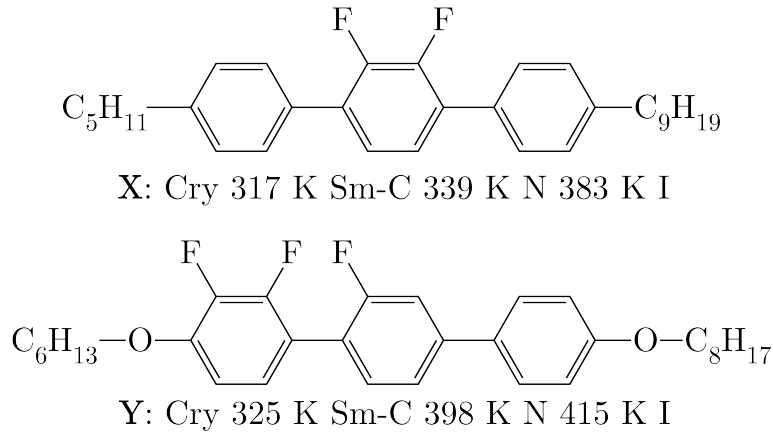


Figure 3.3: Chemical structures for X [2',3'-difluoro-4-nonyl-4''-pentyl-1,1':4',1''-terphenyl] and Y [2,2',3-trifluoro-4-(hexyloxy)-4''-(octyloxy)-1,1':4',1''-terphenyl] liquid crystals, where the phase transition temperatures are shown under the corresponding structures.

Measurements of optical and dielectric properties of X and Y were facilitated by adding a small amount of the BE8OF2N chiral dopant (0.5% w.r.t. mass). This low concentration introduces spontaneous polarization ($\lesssim 5 \times 10^{-6} \text{ Cm}^{-2}$ for the studied temperature ranges), which allows ferroelectric switching in the SmC* phase^[2] while keeping the other physical properties the same as the undoped SmC phase to within the experimental error range. Measurements were made by studying doped X and Y in (nominally) $2 \mu\text{m}$ -spaced TBC (2° surface pre-tilt) and NBC devices. Such low concentrations of the chiral dopant also make the pitch much longer than the selected cell gaps, which allows the helix to be unwound by the tangentially-aligned surfaces, forming the surface stabilized state^[53]. The samples were cooled from the isotropic phase at a rate of 1 K/min using a Linkam T95-PE temperature controller with a resolution of 0.01 K and stabilized for 60 seconds before each set of measurements to

achieve uniform alignment.

Polarized optical microscopy was used to find the director orientations in TBC devices by observing optical extinction angles as a function of temperature. At each temperature increasingly stronger electric fields were applied as square waveforms with corresponding voltages from 0 V to 10 V using the Aim-TTi TGA1241 arbitrary waveform generator. The director was switched to both sides of the layer normal interchangeably to determine the orientation of the in-plane component of the layer normal, as shown in Figure 3.4. From this, zero voltage β_0 and infinite voltage asymptote β_∞ extinction angles were

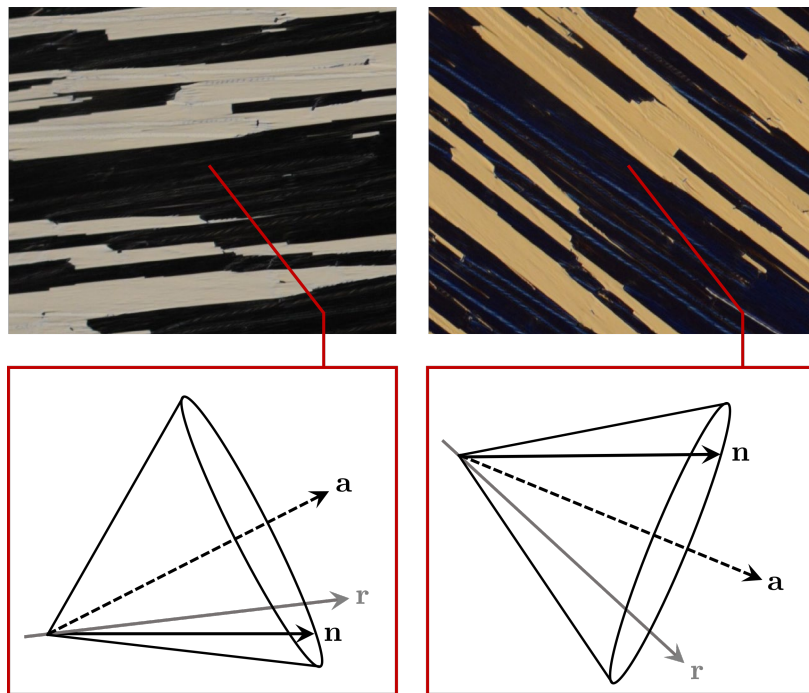


Figure 3.4: Ferroelectric switching of the director in a smectic-C liquid crystal. Photographs of a ferroelectric smectic-C liquid crystal in a parallel plate capacitor with homogeneous tangential boundary conditions and an inner separation gap of $2 \mu\text{m}$. External voltage of $+9 \text{ V}$ was applied in the left image and -9 V was applied in the right image. Rubbing direction is indicated by \mathbf{r} , layer normal is indicated by \mathbf{a} and the director is indicated by \mathbf{n} . The average director of the system was aligned to be perpendicular to one of the crossed polarisers in both cases. Crossed polarisers at South-North and West-East orientations.

calculated as a function of reduced temperature (both are measured in relation to the in-plane component of the layer normal). This allowed optical cone angles θ_o and layer

tilts δ to be calculated numerically from

$$\cos \delta = \frac{\cos \theta_o}{\cos \beta_0} = \frac{\tan \theta_o}{\tan \beta_\infty}, \quad (3.10)$$

which can be derived by considering the limiting cases for the relaxed and the fully switched orientations of the director.^[91,92] Figure 3.5 illustrates the optical director configurations and the corresponding angles that were measured during the process of characterisation of the SmC* phase.

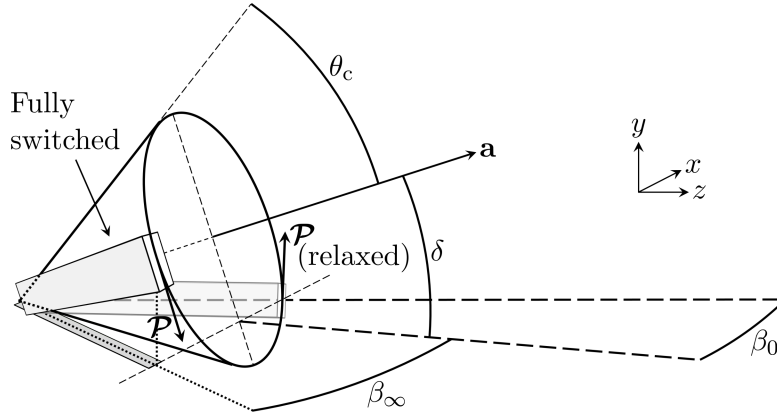


Figure 3.5: Director configurations in a smectic-C liquid crystal phase. Illustration of the optical director configurations in the relaxed and the fully switched ferroelectric smectic-C system in a parallel plate geometry system with an out of plane layer tilt due to layers assuming a chevron geometry.

After every 1 K interval, measurements of the capacitance and the dielectric loss were taken with an Agilent E4980A precision LCR meter were performed on TBC and NBC devices to find ε_p and ε_h , respectively. Each set of measurements was taken by applying an AC voltage of 0.05 V at frequencies ranging from 20 Hz to 2 MHz. Subsequently, an additional DC voltage bias was applied at ascending magnitudes to the TBC devices to find the infinite voltage asymptotes of capacitance to find ε_f , given by Equation (3.6). Optical measurements were combined with permittivity measurements to find the dielectric cone angles θ_ε and the principal permittivities ε_1 , ε_2 and ε_3 of X and Y by solving in Equations (3.6-3.9). Figure 3.6(a) and Figure 3.6(b) show ε_1 , ε_2 , ε_3 , ε_p , ε_f , ε_h and $\bar{\varepsilon}$ as a function of reduced temperature for X and Y, respectively. Calculated values of θ_o , θ_ε , δ , β_0 and β_∞ from optical extinction angle measurements are shown as a function of the reduced temperature in Figure 3.7(a) and Figure 3.7(b) for X and Y, respectively.

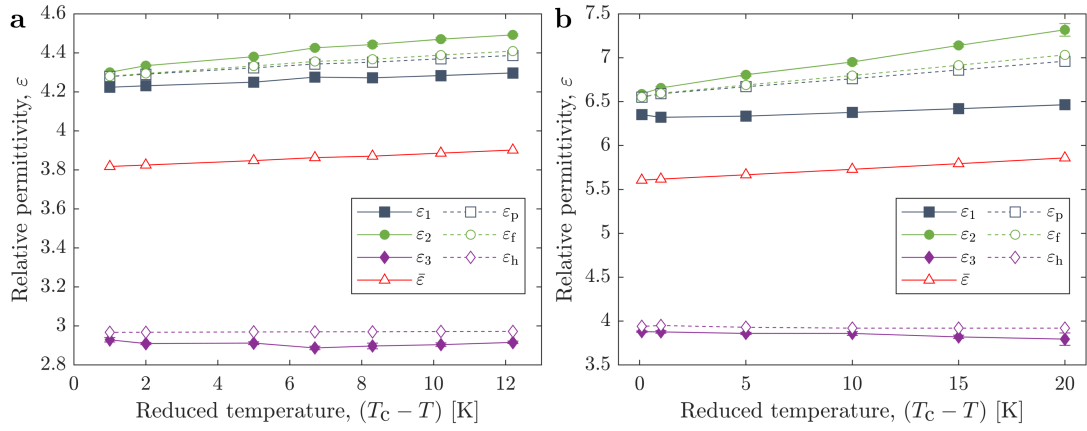


Figure 3.6: Dielectric permittivity measurements. Plot of principal permittivities ϵ_1 (closed circle), ϵ_2 (closed square), ϵ_3 (closed diamond), $\bar{\epsilon}$ (open triangle), ϵ_p (open circle), ϵ_f (open square) and ϵ_h (open diamond) against the reduced temperature $T_c - T$ for (a) X and (b) Y. Lines serve as eye guides only. Dielectric data is shown for the temperatures corresponding to the optical measurements.

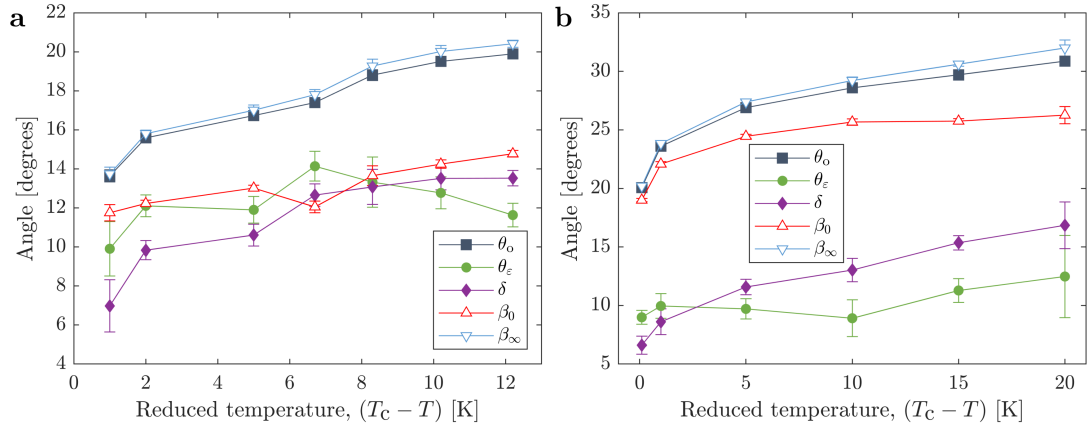


Figure 3.7: Angle measurements. Plot of optical cone angle θ_o (filled square), dielectric cone angle θ_ϵ (filled circle), layer tilt δ (filled diamond), zero voltage optical extinction angle β_0 (open upward pointing triangle) and infinite voltage optical extinction angle β_∞ (open downward pointing triangle) against the reduced temperature $T_c - T$ for (a) X and (b) Y. Lines serve as eye guides only.

Capacitance scans on SmC* liquid crystals can show two relaxation modes: due to field induced fluctuations of the azimuthal director (Goldstone mode) at low frequencies and stretching with respect to the cone's reference frame (soft mode) at higher frequencies, the latter occurring particularly close to the phase transition. Due to the first order nature of NLC to SmC phase transitions, no soft mode was observed in X and Y. On the other hand, a small degree of the Goldstone mode was expected at low frequencies but ionic screening was found in practice. For this reason, a frequency of 10 kHz was selected for calculating dielectric cone angles and principal permittivities of X and Y, where no azimuthal fluctuations around the cone was observed. Examples of broadband dielectric spectra at 10 K below the NLC to SmC phase transitions are shown in Figure 3.8(a) and Figure 3.8(b) for X and Y respectively, where ϵ' represents the real component of dielectric permittivity and ϵ'' represents its imaginary component. By evaluating the dielectric loss factor ϵ''/ϵ' and ϵ' , we can see that the static regime occurs around 10 kHz, which was selected for calculations of the main results.

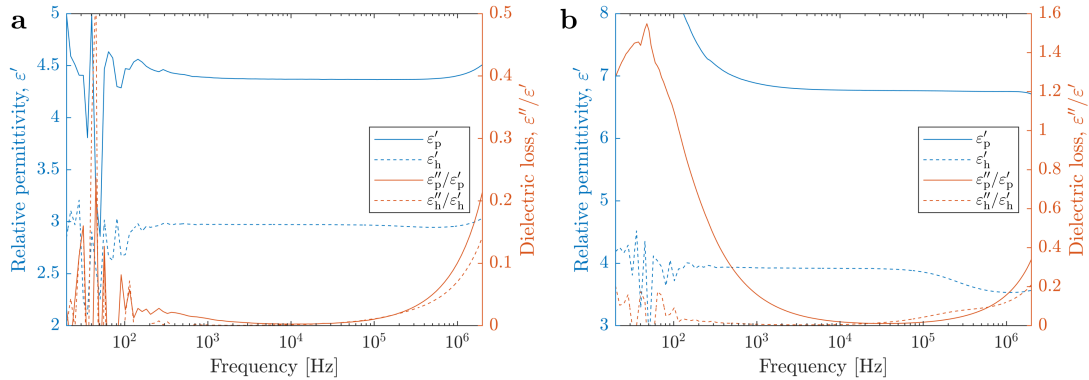


Figure 3.8: Frequency dependence of the dielectric permittivity. Plot of measured permittivities ϵ' (blue lines) and the corresponding dielectric losses ϵ''/ϵ' (orange lines) for (a) X and (b) Y at $T_c - T = 10$ K. Solid lines represent the TBC geometry and the dashed lines represent the NBC geometry.

3.5 Results and Discussion

A comparison of optical and dielectric measurements for each compound confirms that there is a difference $\partial\theta$ between optical and dielectric cone angles. From Figure 3.9 it is clear that $\partial\theta$ increases as the samples are cooled through the SmC phases, showing

an increasing degree of disassociation between the principal optical and permittivity axes. These results show that θ_ε may differ from θ_o by a considerable amount. As $\partial\theta$ increases, orthorhombic approximations become less appropriate for calculating the dielectric properties.

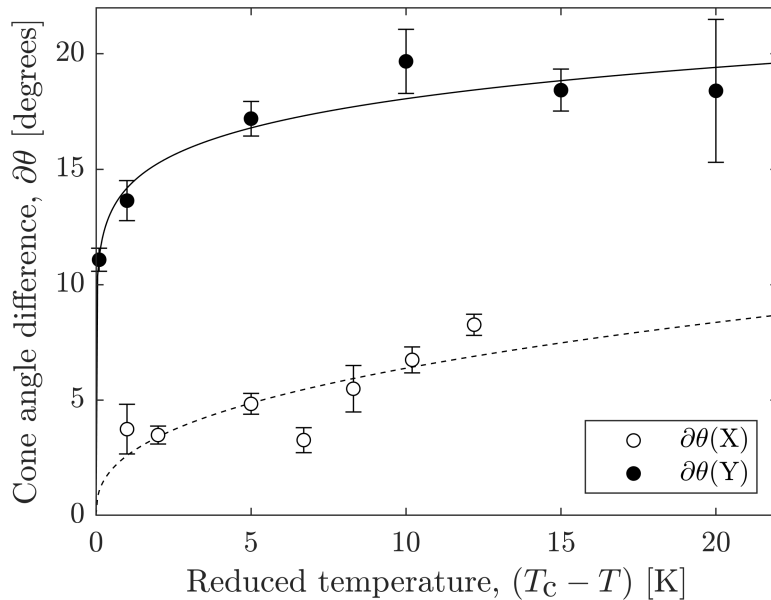


Figure 3.9: Disassociation of optical and dielectric cone angles. Plot of the cone angle difference, $\partial\theta$, against the reduced temperature below the NLC to SmC phase transition, $T_c - T$. Open symbols are used for X and closed symbols are used for Y. Lines are fits to $\partial\theta = a_1(T_c - T)^{a_2}$ and are used as guides for the eye only, where $a_1 = 2.6 \pm 0.9$, $a_2 = 0.39 \pm 0.16$ for X and $a_1 = 14.2 \pm 0.6$, $a_2 = 0.10 \pm 0.02$ for Y.

The introduction of monoclinic symmetry does not have a significant effect on the magnitude of dielectric anisotropy $\Delta\varepsilon$, which already exists in the uniaxial phase. However, dielectric biaxiality $\partial\varepsilon$ only appears in biaxial phases, which makes it sensitive to the monoclinic nature of the molecular shape. Since $\theta_\varepsilon < \theta_o$, using an orthorhombic approximation for a monoclinic molecule will result in an overestimated value of $\partial\varepsilon$. Consequently, the switching times of ferroelectric SmC materials will show a varying degree of disagreement between the theoretical estimates and experimental values, depending on how weak the biaxial order parameters are at a given temperature.

As expected, $\partial\varepsilon$ shows a positive correlation with reduced temperature for both compounds, as shown in Figure 3.10. There is a first order jump of $\partial\varepsilon$ at the NLC to SmC phase transition, which is followed by a roughly linear trend below a temperature

slightly below the transition corresponding to the point at which the layers become fixed at the device surfaces. Unlike X, molecules of Y have several polar components, pointing in different directions, which contribute towards the overall transverse dipole moment. Thus, we observe higher $\partial\varepsilon$ in Y in comparison to those of X. A comparison of $\partial\varepsilon$ to the results obtained from the orthorhombic approximation shows that such an approximation would result in an overestimation by more than a factor of 2. However, it is also clear that this comparison is not appropriate, as the orthorhombic approximation does not allow the governing equations to all be satisfied within experimental error.

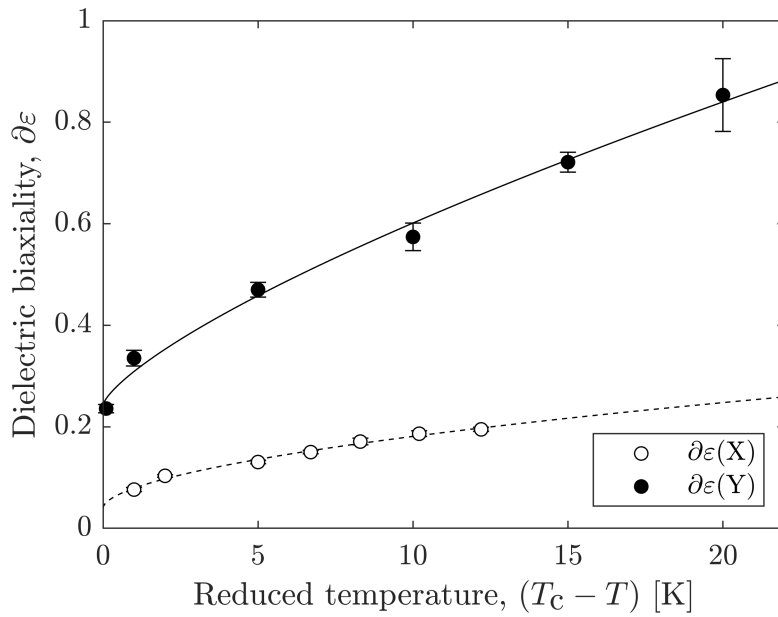


Figure 3.10: Dielectric biaxiality. Plot of dielectric biaxiality $\partial\varepsilon$ against the reduced temperature below the NLC to SmC phase transition, $T_c - T$. Open symbols are used for X and closed symbols are used for Y. Lines are fits to $\partial\varepsilon = b_1(T_c - T)^{b_2} + b_3$ and are used as guides for the eye only, where $b_1 = (3.9 \pm 2.0) \times 10^{-2}$, $b_2 = 0.56 \pm 0.16$, $b_3 = (3.9 \pm 2.4) \times 10^{-2}$ for X and $b_1 = (6.6 \pm 2.3) \times 10^{-2}$, $b_2 = 0.74 \pm 0.11$, $b_3 = 0.24 \pm 0.03$ for Y.

In this study, we have assumed that the optical director (indicated by \mathbf{n}_3 in Figure 3.2) lies in the plane of the device. However, this is not necessarily the case if the steric axis does not coincide with the optical director. By simple consideration of the zigzag shape of the average molecule, we can deduce that the steric cone angle can be lower than θ_o . By performing density functional theory simulations in GAUSSIAN 09 using B3LYP method and a 6-31G(d) basis set, while maintaining the general zigzag shape with a

maximized transverse dipole moment to account for the SmC phase, we can see that the steric axis differs from the polarizability axes by 4.1° for X (net dipole moment of $\mu = 6.07 \times 10^{-30}$ Cm) and 4.6° for Y ($\mu = 9.84 \times 10^{-30}$ Cm); (see Figure 3.11). The result is for individual molecules, which will be affected by the ensemble within the SmC phase and is only valid when there are no intermolecular interactions. Since the optic eigenvalues depend on polarizability, while the dielectric eigenvalues also depend on dipole moment contributions, we expect that the steric axis will deviate from the optics as the cone angle increases. The analysis can also be performed with the assumption that the dielectric director (indicated by ϵ_3 in Figure 3.2) lies in the plane of the device in the TBC geometry. While the dielectric director is much further away from the steric axis, it provides the other extremum to the solution set. The calculation requires an adjustment to the optical results and the principal permittivity values. From this, we see that θ_o and θ_ϵ remain within experimental error of each other, while δ has a significant decrease. Consequently, the angle measurements associated with monoclinic symmetry can be assumed to have negligible error generated from our assumption of the steric axis matching that of the optics. However, the effect on δ is more significant, which means that $\partial\epsilon$ in Figure 3.10 show the upper bound for the actual values. For this reason, it would be instructive to measure the layer tilt angle directly using X-rays at a synchrotron source.

3.6 Conclusion

In conclusion, we have investigated monoclinic symmetry of SmC liquid crystals by showing that a disassociation can exist between the principal optical and dielectric axes with respect to one another. By applying invariance principles to the SmC phase, we can see that the eigenvector sets for optics and dielectrics must share at least one common axis, which must be parallel to the C_2 symmetry axis, due to monoclinic symmetry. The remaining axes need not coincide between optics and dielectrics, resulting in a disassociation of the two through a unitary rotation around the C_2 axis. This was interpreted as the existence of a dielectric cone angle θ_ϵ alongside the optic cone angle θ_o . This resulted in a new variable, given by the difference between the two cone angles $\partial\theta$, which provides a geometrical scale for monoclinic behavior. Following this, we have used two liquid crystal compounds with direct NLC to SmC phase transitions to verify

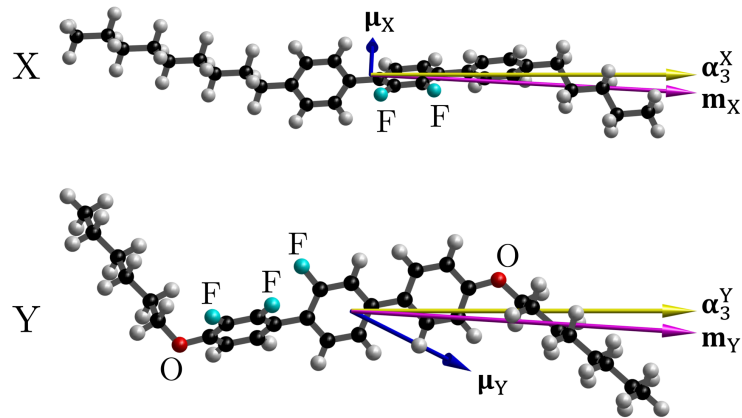


Figure 3.11: Optimised chemical structures for X and Y liquid crystals. Density functional theory B3LYP/6-31G(d) minimized energy configurations of X and Y, where hydrogen, carbon, oxygen (O) and fluorine (F) atoms are represented by white, black red and cyan spheres, respectively. Blue arrows show the direction of the net dipole moments given by $\mu_X = 6.07 \times 10^{-30}$ Cm for X and $\mu_Y = 9.84 \times 10^{-30}$ Cm for Y. Magenta arrows represent the average steric axis of each molecule \mathbf{m}_X for X and \mathbf{m}_Y for Y. Yellow arrows represent the direction of the principal polarisability axis associated with the director α_3^X for X and α_3^Y for Y.

this hypothesis. Since the nature of the NLC to SmC phase transition is first order, this resulted in highly pronounced monoclinic properties. The results indicated that $\partial\theta$ increased as the samples were cooled to as much as 20° for compound Y within the studied range of 20 K below the NLC to SmC phase transition. On the other hand, $\partial\theta$ only increased to roughly half of that for compound X. This suggests that multiple sources of dipole moment contributions result in a higher degree of monoclinic behavior. So far, other studies of ferroelectric liquid crystals have assumed D_{2h} symmetry for calculations of $\partial\varepsilon$, which resulted in overestimated $\partial\varepsilon$ and switching speeds. However, we have shown that monoclinic behavior becomes very important with decreasing temperatures and even immediately below first order phase transitions. Therefore, this will be particularly important for future novel devices, such as those using bent core liquid crystals, which are known to exhibit highly first order behaviour.

Chapter 4

Self-assembly of fractal liquid crystal colloids

This chapter reproduces the study from “Self-assembly of fractal liquid crystal colloids”, published in *Nature Communications*, vol. 10, no. 1, p. 198, 2019.^[93] Nikita V. Solodkov and J. Cliff Jones designed the research and performed confocal microscopy experiments. Nikita V. Solodkov performed the research. Jung-uk Shim and J. Cliff Jones supervised the project.

4.1 Introduction

In the previous chapter, we have considered the parallel plate geometry, which is standard in most device based studies due to its widespread use in commercial applications. However, there is an increasing interest in other confinement geometries such as the cylinder and the sphere. Recently, there has been an explosion of interest in micro-suspensions within nematic liquid crystals, wherein the inclusions self-assemble into various structures due to the creation of defects in the nematic director fields.^[94–100] This process was first observed by creating water droplets with radial BCs inside larger nematic droplets, which created linear chains of inclusions.^[95] In such systems, topologically forced hyperbolic defects stabilize the suspensions of particles by forming topological dipoles with the radial inclusions, which line up in a similar fashion to a linear array of electric dipoles.^[61,96] Similar systems have been observed by adding micro-particles with pre-determined BCs and locally melting the director field with laser tweezers to control the formation of structures through manual rearrangement of

inclusions.^[101] Other studies, such as Ref.,^[102] aim to create unique defect combinations by adding holes to particles, which changes their topological properties.

In this study, we use double emulsion droplets generated in a microfluidics device (see Section 2.4) and controlled agitation to create multiple water droplets with radial BCs inside larger radial nematic droplets. We find that the size differences between the water droplets play a key role in the spontaneous formation of complex three-dimensional (3D) structures, ranging from linear chains to fractal structures. To explain our observations, we use numerical analysis to relate the basic formation of colloidal structures in radial nematic droplets to the solutions of the Thomson problem^[103,104] and extend the analogy to the formation of fractal structures. In contrast to a recent study by Hashemi et al.^[105] that studies the behavior of nematic defects along predetermined fractal shapes, we observe spontaneous formation of fractal shapes due to the topological and elastic properties of nematic liquid crystals.

4.2 Methods

Room temperature nematic E7 liquid crystal mixture (from Synthon) and purified water (containing 0.5% CTAB surfactant) were used to create complex structures inside liquid crystal droplets. CTAB provides radial alignment and stabilizes the emulsions. Polydimethylsiloxane was used to create the double emulsion microfluidics devices in accordance to the methods described in reference.^[106] Double emulsions of water in liquid crystal in water were achieved using a combination of three Harvard Apparatus PHD ULTRA syringe pumps and controlled shaking. The samples were extracted onto glass slides, covered with glass covering slips and studied using a Leica 2700 cross polarizing microscope. Optical microscopy photographs were taken using a Nikon D7100 camera. Counting the number of primary satellites was performed by drying the outer water phase, which caused the nematic droplets to roll and rotate the structures inside them. Confocal microscopy was performed with J. Cliff Jones using a Zeiss Elyra PS1 microscope with an alpha Plan-Apochromat 100 \times oil immersion objective and captured using an Andor EMCCD detector.

Simulations of nematic director fields were performed using COMSOL 5.3a finite element analysis software (stationary study) through the minimization of the Frank free

energy,

$$F = \frac{1}{2} \int_v \left(K_1 (\nabla \cdot \mathbf{n})^2 + K_2 (\mathbf{n} \cdot \nabla \times \mathbf{n})^2 + K_3 (\mathbf{n} \times (\nabla \times \mathbf{n}))^2 \right) dv, \quad (4.1)$$

with the following values of Frank elastic constants $K_1 = 10.8$ pN, $K_2 = 6.5$ pN and $K_3 = 17.5$ pN. The domain radius was set to be $30 \mu\text{m}$, satellite size was fixed to $1 \mu\text{m}$ and r (ratio of the core to satellite radii) was varied from 1 to 10 in 0.1 step increments. Defect points were cut out from the nematic domains when evaluating the total free energy.

4.3 Self-assembly of radial inclusions

Consider the domain of a nematic droplet with radial (normal to the surface) BCs. From topological principles, a director field discontinuity with a charge of $+1$ is formed inside it and centralized to minimize the free energy of the system. Adding a smaller inclusion (such as a particle coated with a surfactant, or a second water droplet) with normal BCs does not create any additional distortion to the radial director field. Instead, the inclusion minimizes the free energy by creating a virtual, highly splayed defect at the centre of the particle and moving the inclusion to the centre of the system. In this work, we will refer to the first inclusion (water droplet) as the core and additional $+1$ radial inclusions as satellites, which must be accompanied by -1 hyperbolic defects to conserve the total topological charge of the system. Figure 4.1 illustrates a possible creation process of a water droplet at the boundary of the nematic domain and the continuous formation of the topological dipole.

For illustration purposes we assume that the core always remains at the centroid of the nematic domain, which is true for the cases of symmetric structures. Once a satellite enters the director field, elastic forces drag it towards the point of highest splay, where it enters the core's primary orbit. All other satellites entering this primary orbit are attracted to the core but repel each other. This suggests that there exists some characteristic number of satellites, N_c , beyond which the satellites are unlikely to enter the primary orbit of the core inclusion. By symmetry, the second satellite must attach itself on the opposite side of the core to the first, to minimize elastic distortion. A third satellite then has a choice between readjusting the positions of the first two satellites and attaching itself to the core or to one of the two existing satellites co-linearly. Figure 4.2 illustrates the satellite attachment process with linear chains of

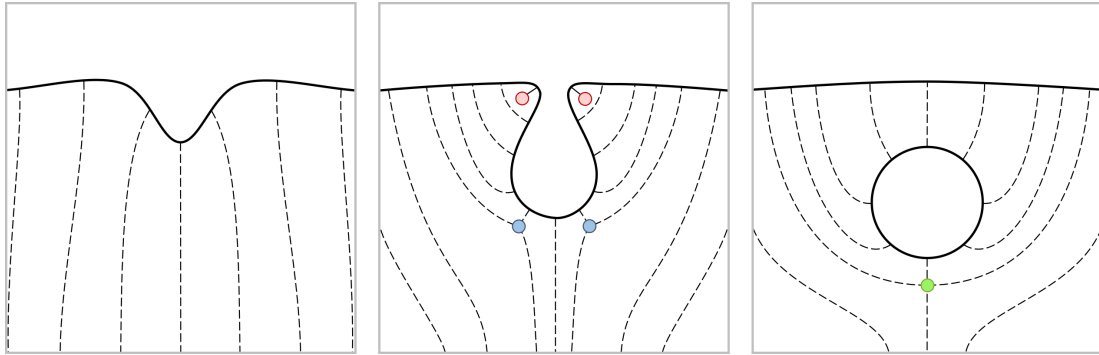


Figure 4.1: Double emulsion formation. Axisymmetric illustration of a possible sequence of events that may occur near the boundary of the nematic droplets during the shaking procedure. First, the boundary of a radial nematic droplet (solid black lines) becomes unstable. In the reference frame of the nematic droplet, this causes the boundary to be pushed inwards and a pair of disclination loops is created to accommodate the high elastic distortion of the director profile (dashed black lines). The disclination loops must originate from the same location to maintain topological continuity. Following this, the system begins to pinch off the the highly disturbed boundary to create a water droplet inside the nematic droplet. The disclination loop that is closest to the boundary has a cross-sectional topological charge of $+1/2$ (red circles), and helps the pinch off process by minimising its length. The other disclination loop has a cross-sectional topological charge of $-1/2$ (blue circles) and moves in the opposite direction to form a topologically equivalent hyperbolic hedgehog (green circle). Together with the newly formed inclusion, the hyperbolic defect creates a topological dipole, which is propelled towards the centre of the nematic droplet by elastic forces.

satellites extending radially outward from the core. The relative sizes of the droplets determine the resulting structure. For droplets of similar size, the third and fourth droplets will become arranged at the tetrahedral angles to the core, and additional droplets beyond the fourth attach as satellites to the higher orbitals, four per orbital, to create a characteristic tetrahedral structure.

To determine the maximal orbit capacity, we first need to study the solution sets for distributions of repulsive points around the boundary of a circle in 2D and on the surface a sphere in 3D. In 2D systems, primary orbit satellites distribute themselves along the vertices of regular polygons. Similarly, in 3D the structures follow the solutions to the Thomson problem (originally used to describe the electronic structure of atoms for the

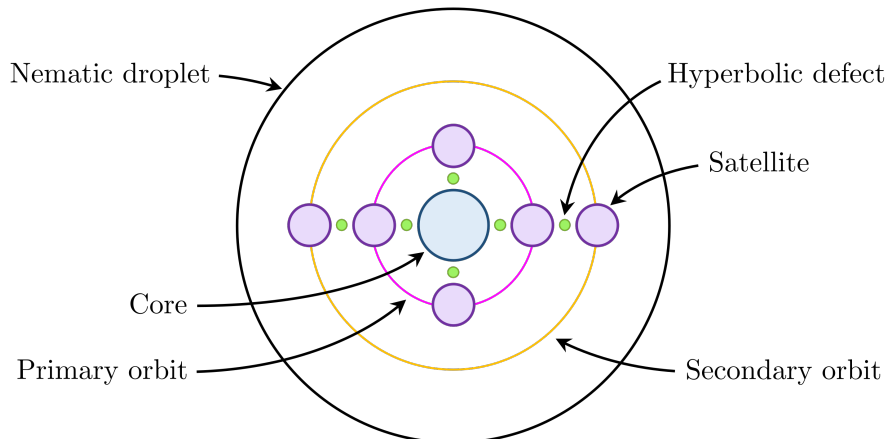


Figure 4.2: Structural self-assembly in double emulsion systems with normal boundary conditions. The largest water droplet (blue) situates itself at the centre of the nematic droplet and acts as the system’s core inclusion. This allows smaller satellite droplets (violet) to elastically attach themselves to the core via their accompanying topological defects (green), making up the primary orbit (magenta). Subsequent satellites can attach themselves to the primary orbit satellites, making up the secondary orbit (yellow).

superseded “plum-pudding” model), which include some regular polyhedrons. Two satellites can continue to move closer together until the director reaches a characteristic distortion (this is equivalent to adding more satellites to the orbit). By symmetry of the director field, primary orbit satellites share a network of mirror planes and symmetry axes of rotation (see Figure 4.3). We can see that the highest amount of distortion in the director field occurs in the plane containing the core and two nearest neighbor satellites. As the two satellites in the same orbit approach each other, the characteristic separation point will be reached first in this plane, thereby reducing a 3D problem to 2D.

Each satellite of unitary radius is pulled towards the core of radius r to minimize the system’s elastic free energy and stabilized at a centre-to-centre separation of $(r + 1)h$, where h is the separation factor. Using microfluidically generated inclusions, we measure that $h = 1.24$ for E7 liquid crystal at room temperature. This result closely follows the values determined numerically^[107] and experimentally^[95,108] for similar materials when in dipolar chains. Due to the symmetry of the system, we consider two elastic constants: K_1 , which opposes the divergence of the director field, and K_3 , which opposes the bending of director lines. In our system, K_3 is responsible for pushing orbit-equilibrated

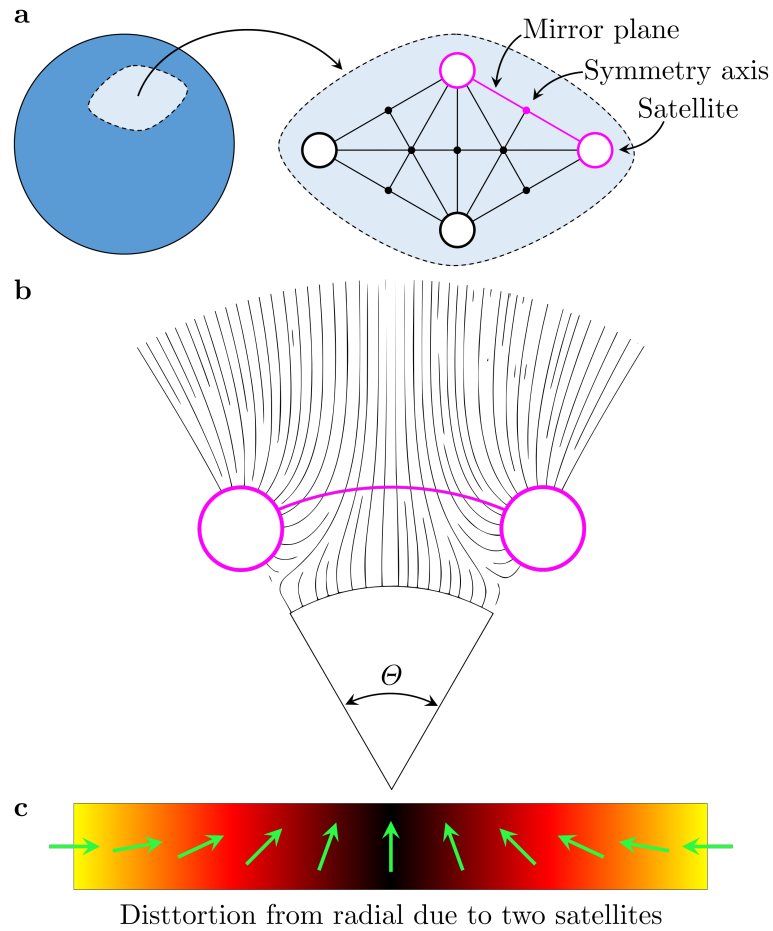


Figure 4.3: Satellite distortion network. (a) Sub-domain of the spherical surface corresponding to the primary satellite orbit. Large unfilled circles represent satellites, small filled circles represent symmetry axes of rotation with radial director profiles and solid lines represent unfolded mirror planes. The plane of highest disturbance (repeated in the structure) is highlighted in magenta. (b) A slice of the magenta plane from (a), showing the director lines due to two satellites separated by a polar angle of θ . (c) Distortion of the director field in the radial reference frame as a function of the polar angle between two neighbouring satellites along their orbital path, magenta arc from (b).

satellites away from each other. On the other hand, K_1 restores the director field to the radial configuration, which allows satellites to be closer to each other. This implies that there exists a characteristic angular separation of neighbouring satellites θ_c , beyond which no two satellites can come closer without a great cost to the elastic free energy of the system.

To determine the characteristic separation of satellites we look at the natural distortion of the director field that a lone satellite creates. Since we seek the characteristic value, only the distortion along the orbit needs to be examined, where the repulsion between adjacent satellites is greatest. At the boundary of the satellite, the distortion is maximal and decays away exponentially as a function of the polar angle at a rate that depends on the ratio of the ratio of K_1 and K_3 elastic constants. Introducing a second satellite to the same orbit is equivalent to creating a mirror line half way between them, where the director is fully straightened to the radial configuration. We guess that θ_c is reached at the point where the natural distortion angle from the radial configuration of the lone satellite reaches a characteristic value of $\xi_c = \tan^{-1}(K_1/K_3)$. This means that two satellites can be brought closer together up to the point where their push (K_3) dominant regions touch.

As the core to satellite size ratio r increases, we expect the polar influence of satellites to become less significant and θ_c to decrease with it, allowing a greater number of satellites to enter the primary orbit. At low values of r , satellites are closer to the centre of the domain and their natural director profiles closely match each other, which decreases θ_c . On the other hand, the natural director field of the domain becomes less divergent with increasing orbit size and director lines become more parallel. By comparing the director field to the electrostatic field lines between two charges, we make an ansatz of the following form

$$\theta_c = 2\theta_0 - 2\alpha \frac{\xi_c}{\sqrt{r}} \ln \left(\frac{\xi_c}{\xi_0} \right), \quad (4.2)$$

where α is constant for a given domain size, $\theta_0 = 2 \operatorname{arccsc}(2h(r+1))$ and $\xi_0 = (\pi - \theta_0)/2$ are the polar and the distortion angles at the boundary of the satellite, respectively. From this, we can expect that liquid crystals with high K_1/K_3 ratios will be able to support more satellites than the ones with low K_1/K_3 ratios. An example of the free energy density is illustrated in Figure 4.4, where the isosurfaces corresponding to $f = 1 \text{ J/m}^3 = 1 \text{ pN}/\mu\text{m}^2$ are shown in blue for $r = 2.5$ and $r = 5$. Here, there are 8 primary orbit satellites that assemble around the core in a square antiprism configuration to minimise the total free energy. Each satellite comes with its own distortion profile, which experiences no significant changes when we increase the core's radius. Consequently, this means that their angular influence becomes weaker as r is increased, which increases the likelihood of additional satellites joining the same orbit.

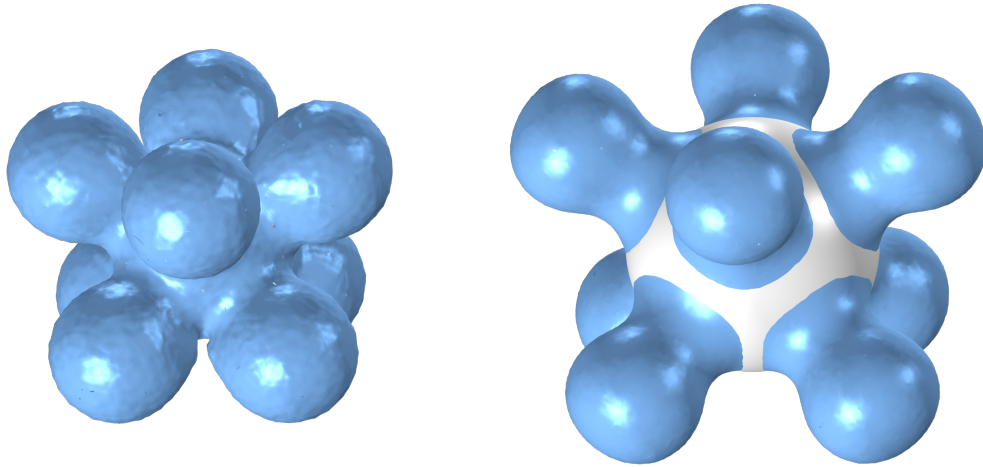


Figure 4.4: Square antiprism satellite packing. Illustration of the free energy density in a numerically simulated system consisting of 8 primary orbit satellites around a central core, with $r = 2.5$ (left) and $r = 5$ (right). White surface corresponds to the boundary of the core and blue surfaces correspond to a free energy density of 1 J/m^3 .

4.4 Primary orbit satellite packing

The maximal number of satellites in the primary orbit N_c can be calculated numerically by comparing Θ_c with the angles generated by the closest neighbouring vertices of the Thomson problem solutions. As r tends to infinity, exact solutions of N_c can be found using the Fejes inequality,

$$2 \sin \left(\frac{\Theta}{2} \right) \leq \sqrt{4 - \csc^2 \left(\frac{\pi N}{6(N-2)} \right)}, \quad (4.3)$$

which becomes exact for $N = 3, 4, 6, 12$ and $N \rightarrow \infty$.^[103] Due to the dependence of Θ_c on r and the associated Thomson problem solution for N , we find that the relationship between N_c and r is weakly non-linear for small values of r and increases in a step-function-like fashion. The numerical results indicate that for systems in which the satellites are identical in size to their cores, triangular configurations are expected and we may expect tetrahedral structures to form once r reaches 1.1. In practice, there always exists a small size distribution of water inclusions, which creates enough variation in r to allow tetrahedral structures. The value of N_c serves as the maximal achievable number of primary satellites for a given core to satellite ratio of the system. We find that our ansatz is closely matched by the numerical solution with $\alpha = (1.12 \pm 0.01)$ and

therefore, can be used as quicker estimation method for N_c as a function of r . This can be seen in Figure 4.5, which shows the allowed solutions for the primary orbit satellites alongside a representative selection of experimental results (the selection does not represent the frequency of occurrence).

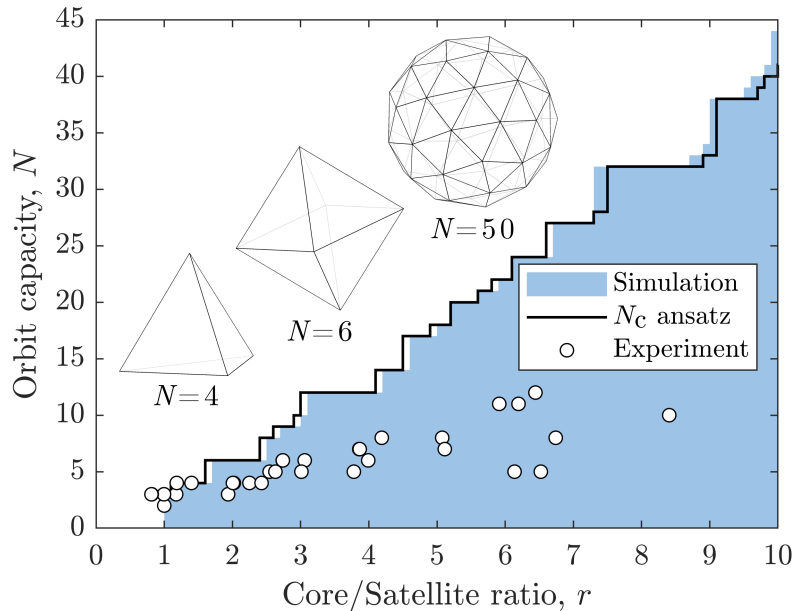


Figure 4.5: Primary orbit capacity and packing. Orbit capacity N as a function of the core to satellite size ratio r illustrating numerical space of possible values (blue shading), estimated maximal orbit capacity from the ansatz (black line), a representative selection of experimental results achieved with water in E7 in water double emulsions (circles). Shapes corresponding to $N = 4$, $N = 6$ and $N = 50$ are shown above the curves.

Our experimental observations of double emulsions formed using microfluidics indicate that satellite droplets self-assemble into tetrahedral configurations almost exclusively and lower order configurations are possible but rarely observed. This is a direct consequence of the fact that the total free energy is minimised when the nematic droplet the contained structures have spherical symmetry. This introduces an additional balance between spherical and polyhedral symmetries. Digonal and triangular configurations are two-dimensional and lack 3D symmetry balance. On the other hand, the tetrahedral configuration is the lowest order structure with 3D symmetry balance and is therefore preferred, as observed in double emulsions. To achieve configurations with two and three primary satellites in 3D nematic droplets, a reduction in symmetry must be introduced. The digonal configuration can be achieved by forcing the nematic

droplets to have an ellipsoidal shape during a slow self-assembly process. Following their assembly, such structures remained stable throughout the observation period (over a week), due to the stabilizing effects of the topologically imposed hyperbolic defects separating the inclusions at the centres of the nematic droplets. When the samples were heated above the nematic to isotropic phase transition temperature, this stabilization disappeared (due to the lack of a director field) resulting in collapse of the structures into a single, larger core.

Once a structure is formed inside a nematic droplet, it can be switched into a different configuration by applying an external field. Here we illustrate this by switching a tetrahedral structure inside a 3D radial nematic droplet into a lower order state. To achieve this effect, the droplet was deformed rapidly by applying external pressure to the observed region of the glass containers (used for observation under the microscope). This resulted in a large scale redistribution of the water droplets that formed the tetrahedral structure, followed by the reconstruction into a configuration with the closest energy minimum. By increasing the agitation, the structure was deformed sufficiently to reconstruct itself into a 2D shape while still remaining in a spherical 3D nematic droplet. A comparison between the original and the reformed structures is shown in Figure 4.6. The resulting structure consisted of a triangular segment with a single linear chain of satellites. This bears a clear resemblance to the structures seen in 2D nematic droplets from reference.^[95] Heating the sample close to the nematic to isotropic phase transition temperature reduces the number of birefringence fringes and allows a clearer comparison with the 2D cases.

Another way to switch the structures is by reducing the dimensionality of the samples. This can be done by reducing one of the coordinates to a length scale closely comparable to the inclusion diameter, for example, using a lateral force. Analogous to the 3D case, the satellites form structures following the vertices of regular polygons. When a droplet with a 3D structure is collapsed to a (relatively) flat disc, the geometrical shape is no longer supported by the dimensionality of the space and must collapse into a 2D configuration. Since $N_c(r \approx 1) = 3$, flattening a tetrahedral structure without an additional bias in a particular dimension can result in a delayed large scale redistribution of satellite droplets into a triangular structure. However, if a nematic droplet is deformed into a disc-like shape with a non-circular boundary, it results in a reorientation of the structure to mimic the geometrical asymmetry formed by the boundary. This is expected,

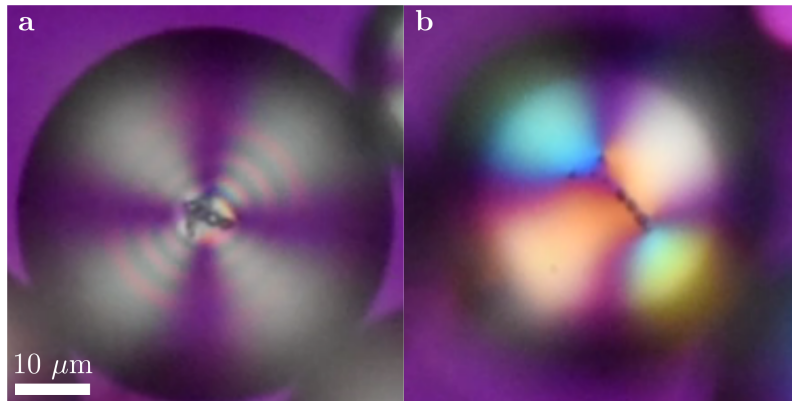


Figure 4.6: Switching between primary satellite configurations. Polarized microscopy images of (a) a nematic droplet with a tetrahedral structure in the centre and (b) the same nematic droplet after external agitation on the brink of the nematic to isotropic phase transition. Crossed polarisers at South-North and West-East orientations; full-waveplate at NW-SE orientation of the extraordinary axis (to confirm radial orientation of the director field).

as geometrical constraints extend their influence throughout the bulk of the nematic domain that they contain. To achieve this, a glass plate was freely suspended on the surface of a sample with radial nematic droplets, containing tetrahedral structures, in water. Evaporation of the external water resulted in the aggregation and flattening of the nematic droplets and a collapse of 3D structures formed by the inclusions. As before, the resulting structures showed digonal, triangular symmetries and their combinations. An example of this is shown in Figure 4.7, where we can see a combination these shapes, which form a structure that resembles the shape of the deformed disc-like container.

Increasing r further creates more docking sites in the primary orbit, allowing higher values of N to be achieved. However, most experimental observations are unlikely to reach the maximal orbit capacity limit for high r . Instead, each primary orbit satellite becomes a potential docking site for the nearby dock-seeking satellites, decreasing the statistical probability of subsequent primary orbit satellite attachments. An example of this can be seen in Figure 4.8, which shows a confocal microscopy image of a radial nematic droplet with a structure comprised of 6 primary orbit satellites (forming the vertices of an octahedron) for $r = 3.0 \pm 0.5$ (error from pixel size). The corresponding N_c for this core to satellite ratio from Figure 4.5 is 10 ± 2 , which suggests that the core had the potential to support up to 4 ± 2 additional satellites in its primary orbit.

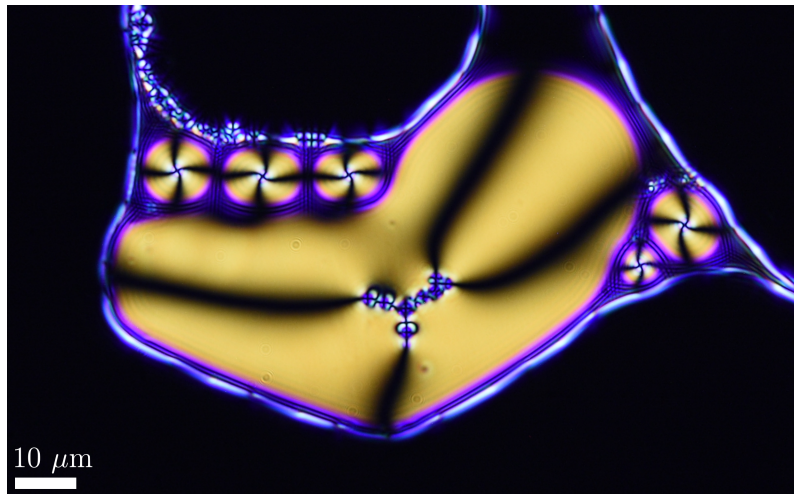


Figure 4.7: Triangular satellite self-assembly in a parallel plate geometry. Polarized microscopy image of a nematic droplet in the shape of a deformed disc in 2D space (third dimension is comparable to inclusion diameter) with normal BCs. Inside the nematic domain, a 2D structure comprising of linear and triangular segments of inclusions with radial BCs is formed, mimicking the shape of its container.

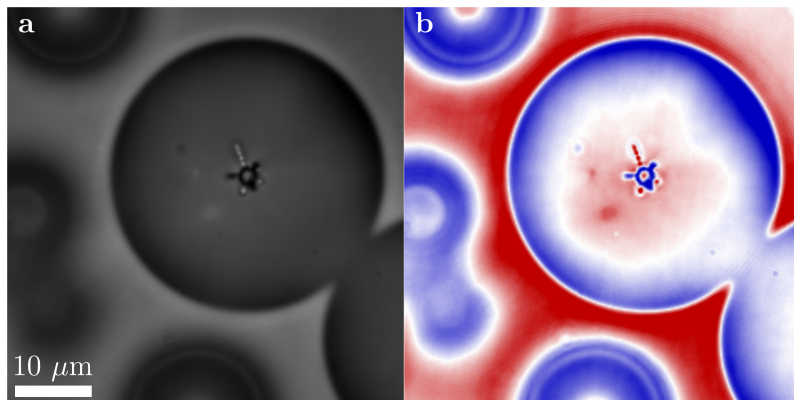


Figure 4.8: Octahedral satellite packing. (a) Confocal microscopy image of a radial nematic droplet showing a structure with 6 primary orbit satellites formed by water droplets with normal BCs and (b) the corresponding color enhanced image.

4.5 Fractals

Fractal structures are generated by self-similar patterns, consisting of rescaled copies of themselves. They are often seen in naturally occurring systems, ranging from snowflakes and seashells to the properties of the human heart,^[109] diffusion limited aggregation,^[110] Brownian motion^[111] and galaxy distributions^[112]. To measure the self-similarity

properties of fractals, we often use the (Hausdorff) fractal dimension, D , which describes the scale-independent change in detail of a fractal and its ability to fill space. For a given fractal pattern consisting of an initiator and a generator that produces n copies of its previous evolution, each scaled down by a factor of $1/r_i$, the fractal dimension is given by

$$\sum_{i=1}^n r_i^{-D} = 1, \quad (4.4)$$

where i represents the indexing of the individual fractal elements.^[113] If the scaling factor r_i is the same for all evolution sites ($r_i = r$), then this equation reduces to $D = \log n / \log r$. For example, the Cantor set is constructed from by repeatedly removing the middle third of a line segment at every step of the evolution. This results in the fractal dimension of $\log 2 / \log 3 \approx 0.63$, which does not have enough information to fill a 1D space.^[113] However, natural fractals often consist of finite number of evolution steps with irregular generators, which causes the fractal dimension to differ between evolution levels as well as within them.

In cases such as the one from Figure 4.8, the remaining space in the primary satellite orbit is not filled due to a small total number of inclusions. When there is a much larger number of inclusions, another self-assembly process can take over expanding the space of possibilities to the creation of fractal structures.

As satellites self-assemble into chains that extend radially outwards from the core (see Figure 4.2), they provide local distortion fields similar to that of the original core droplet. By symmetry, each droplet in a linear chain of satellites is separated by a series of warped planes that lie perpendicular to the pointing directions of each chain. Since the satellites have normal BCs, each separator plane is equivalent to a 2D disc with radial BCs. This means that a satellite situated between two neighbouring separator planes can act as a secondary core, which acts as an additional docking space for much smaller secondary satellites. The self-assembly process of producing secondary satellites is very similar to that of the initial 3D problem, but now the structures follow the vertices of regular polyhedrons, centred at a secondary core (cf. Figure 4.7). Figure 4.9 shows confocal microscopy images (taken from two different perspectives) of a fractal structure with 2 steps of evolution. The initial arrangement of the primary orbit satellites forms a tetrahedral base structure with $r = 2.0 \pm 0.4$, which is extended at three of the four primary satellite chains into additional secondary structures with deformed triangular symmetry or $r = 2.9 \pm 0.6$. Applying equation (4.4) before averaging gives $D = 2.1 \pm 0.4$

for the first evolution level and $D = 1.0 \pm 0.2$ range for the second evolution levels. With the aid of depth based color enhancement, we can clearly see that the structures are three-dimensional and follow the shapes described by our hypothesis.

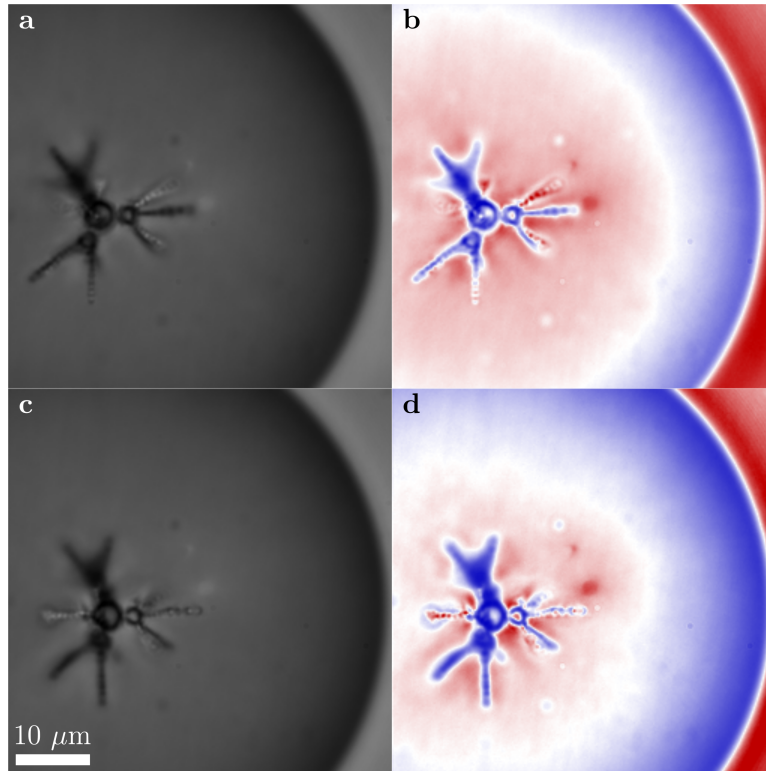


Figure 4.9: Fractal satellite packing. Confocal microscopy images showing a self-assembled fractal structure with 2 steps of evolution, formed by water inclusions with normal BC inside a radial nematic droplet. Images (a) and (c) show different orientations of the same structure. Images (b) and (d) show the corresponding visually enhanced equivalents.

We can extend this analogy further by allowing secondary satellites to act as tertiary cores for much smaller quaternary satellites, and so on. An example of this can be seen in Figure 4.10a, which shows a polarizing optical microscopy image of a fractal structure progressing through several levels of evolving symmetry. The structure consists of a tetrahedral base of primary satellites (fourth primary chain hidden in the image due to the viewing angle and the location of the focal plane) and extends into a series of fractal structures with 3 or more steps of evolution. This suggests that if there exists a sufficiently large number of inclusions with a wide size distribution inside a radial nematic droplet, then a fractal structure will form around the core. Evaluating the

fractal dimension of the first evolution level gives $D = 4.1$ with an undefined error, due to its divergence at $r = 1$. This implies that this fractal generator cannot be sustained in subsequent evolution steps, as it will overlap itself in space. As expected, the fractal dimension for the second level has a much lower value of $D = 0.9 \pm 0.1$. The onset of fractal formation along the initial satellite chain is determined by the difference between N_c and N_1 (shown in Figure 4.5), as well as the sizes of secondary satellites relative to potential secondary cores. For example, if the $N_1 = N_c$, then a fractal chain cannot form on the primary orbit and the fractal onset must happen further along primary chain. However, if the primary chain terminates at the primary orbit, then a splitting of the chain can occur (e.g. Figure 4.9).

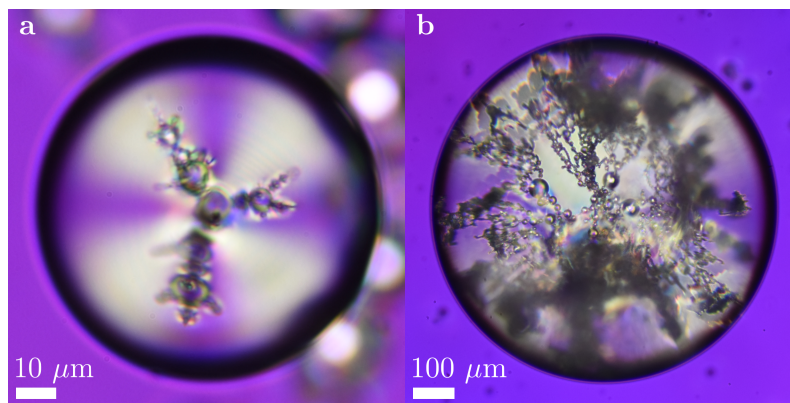


Figure 4.10: Large scale, complex fractal satellite packing. Polarizing optical microscopy photographs of (a) a nematic droplet with a fractal colloidal structure (tetrahedral frame with another arm behind the focal plane) and (b) a nematic droplet (450 micrometer radius) with an incoherent cascade of fractal structures formed by water inclusions with normal BCs. Crossed polarisers at South-North and West-East orientations; full-waveplate at NW-SE orientation of the extraordinary axis (to see the 3D structure clearly). Retardation difference from the waveplate is screened by the high retardation due to the thickness of the nematic droplet.

In general, the Hausdorff dimension of a fractal is always greater than its topological dimension,^[112] with lines producing fractals with $D > 1$ and surfaces producing fractals with $D > 2$. In this problem, the fractals are formed by the self-assembly of smooth spheres that are separated by hyperbolic defects. This means that unlike the Apollonian sphere packing, in which their surfaces touch and fill all available space, there is no roughness associated with any of the surfaces of these structures. Instead, the concept of

fractals manifests itself in the form of the tree-like structures of broken up components, such that $D > 0$ (cf. Cantor dust^[113] in 3D has $D = \log 8 / \log 3 \approx 1.89$). For a given evolution level, D describes the statistical distribution of inclusion sizes, as it represents the logarithmic ratio between the number of satellites and their sizes in relation to their core. We also observe that equal inclusion sizes have the tendency to form linear chains and a size jump is required to induce a fractal split. The only exception to this occurs at the primary core, where the split is symmetry driven. This means that all the relevant size distributions that are necessary to form fractal structures are described by the collection of fractal dimensions across the evolution levels in each nematic droplet.

Most of the first evolution structures from Figure 4.5 have fractal dimensions in the $d \in (1, 2)$ range, with a few exceptions close to $r = 1$. Since random motion is introduced during the creation of high r systems, fractal structures are also likely to form, which reduces the potential number of primary orbit satellites, as the branches extend laterally and push each other away. After each evolution step, both N and r typically increase, giving secondary evolution fractal dimensions in the $D \in (0.75, 1.25)$ range. Due to the limits of optical resolution, fractal structures with higher orders of evolution become increasingly difficult to identify. The presence of further iterations was observed but were not individually distinguishable for accurate measurements. Additionally, the concept of a director field loses its meaning and becomes undefined over length scales comparable to the molecular scale. This imposes a lower limit onto the sizes of satellites and the number of possible fractal evolution steps. Beyond this point, liquid crystals cannot support topologically stabilized structures. On the other hand, the effects of BCs on liquid crystals begin to lose coherence over distances larger than a few hundred μm . In this case, the fractal structures will still form locally but the directional symmetry will become increasingly less prominent with greater structure size. Figure 4.10b shows a nematic droplet with a 450 μm radius with an extremely complex fractal structure consisting of a large cascade of incoherent evolutionary steps.

4.6 Conclusion

In conclusion, we have investigated the properties of spontaneous self-assembly of geometric structures formed from water inclusion with normal BCs inside radial nematic liquid crystal droplets. Due to the vector like behavior of nematic liquid crystals,

all disturbances in the director field are governed by topological rules. We created permanent disturbances by adding small water droplets with normal BCs to the nematic droplet domains, which resulted in the formation of stabilizing hyperbolic defects these emulsions. Our results indicate that in geometrically unbiased nematic droplets, radial inclusions spontaneously form 3D structures with symmetry properties matching those described by the solutions to the classical Thomson problem. Using numerical simulations of the director field, we have shown that the ratio between the core and the satellite inclusions plays a key role in the resulting shapes of these self-assembled colloidal structures. We also provide a simple model to describe the maximal capacity of satellites around the core as a function of their size ratios and the elastic constants of the nematic liquid crystal. As expected, it suggests that as the ratio between the bend and the splay elastic constants gets bigger, a core can accommodate more satellites in its primary orbit. Similarly, a larger core can provide more room for director deformation and therefore, a higher number of satellites. The most common shape found experimentally consisted of a core with four dipolar satellite chains extending radially away from it with tetrahedral symmetry. The shape was then altered by physical agitation of the samples near the nematic to isotropic phase transition and deformation of spherical droplets to 2D disks to obtain single linear chains and triangular structures. Following this, we found that in systems with large distributions of satellite sizes, the colloids self-assembled into fractal structures. The number of symmetry evolutions depended on the distributions of satellite sizes. Systems with large distributions were able to achieve several evolutionary steps, surpassing the resolution of optical microscopy. Due to the length scales of director fields, the structures formed in nematic liquid crystals have a finite number of possible fractal evolution steps in the formation process of fractal colloids. This can be used for designing a variety of photonic structures with different complexity levels. For example, microfluidics can be used to create a core that accommodate a specific structure consisting of fluorescent intrusions or gold nano-particles.

Chapter 5

Electrically driven rotation and non-reciprocal motion of nematic liquid crystal colloids

The chapter presents a study that was performed in collaboration with Antariksh Saxena. Nikita V. Solodkov, Antariksh Saxena and J. Cliff Jones designed the research. Antariksh Saxena performed majority of the experiments with some contributions from Nikita V. Solodkov. Nikita V. Solodkov performed the analysis and the numerical simulations. J. Cliff Jones supervised the project.

5.1 Introduction

Deliberate manipulation of colloidal microparticles and nanoparticles offers the material scientist and application engineer an invaluable tool for controlling functional materials.^[114] Whether in the field of biology, photonics or micro-robotics, the ability to move and orient solid components within a liquid matrix has enormous potential for a variety of applications.^[97,115–118] A familiar and commercially successful example of this is the electrophoretic display that is used for e-paper, in which microcapsules containing a dispersion of bi-coloured nanoparticles are suspended in a polymer matrix.^[119] The nanoparticles are arranged with different zeta-potentials to allow electric field manipulation of their position within each droplet, thereby allowing an electrically controllable “ink on paper” appearance. Other possibilities that yet remain visions of their inventors include the self-assembly of colloidal and emulsion systems with potential

applications for optical computers^[120–122] and biological sensors^[123,124]. Meeting such potential, however, will require particles and media that are significantly more functional than the simple system used for e-paper. One of the more promising approaches is that of nematic liquid crystal colloids. Recently, there has been a wealth of activity in using nematic liquid crystals as hosts for colloidal dispersions due to their optical and electrically controllable and anisotropic nature.^[93,101,102,123–131]

As we have already discussed in the previous chapter, NLC colloids are highly susceptible to topology and BCs that can produce long range gradients in the director fields and promote the self-assembly of structures with varying complexity, ranging from linear chains to crystal-like structures^[98,101,126,132] and fractals^[93,133]. Furthermore, geometrical properties of the colloids^[94,125,128,132,134] as well as that of the bounding domains^[93,135] can have a strong influence on their configurations in NLCs.

In this study, we demonstrate the importance of the geometry of colloidal particles on their behaviour in NLC hosts and in particular their response to external electric fields. The systems are studied both numerically and experimentally to distinguish the key factors that influence the orientation of colloidal particles. A similar set of systems has been investigated in recent studies by C. Lapointe et al.^[125] and Y. Yuan et al.^[131] The first study investigates in-plane and out-of-plane electrical switching properties of torus-like cuboidal microparticle platelets, while the second study investigates the spinning of colloidal particles mediated by polarising light. In contrast, our study focuses on determining the optimal configurations of microparticle platelets as a function of their aspect ratios and domain sizes. Following this, we use geometrical symmetry breaking to induce rotation and non-reciprocal motion of colloidal particles in a direction that is perpendicular to that of the applied electric field. It is worth noting that the emulsion described in the previous chapter have complex electrical characteristics due to the high electrical conductivity of water. However, the colloidal particles in this study are dielectrics, which simplifies the electrical effects of the system.

5.2 Methods

Cuboid and triangular prism shaped particles were created from SU-8 photoresist using a two-dimensional direct write laser photolithography process (by Antariksh Saxena).^[136] Particles with length $\mathcal{L} = 15 \mu\text{m}$, thickness $\mathcal{T} = 5 \mu\text{m}$ and width $\mathcal{W} = 15 \mu\text{m}$ (see

Figure 5.1a) were dispersed into the commercial NLC mixture MLC-6204-000 (Merck Chemicals Ltd.), which has a highly positive dielectric anisotropy of 29.3 at 25°C. The nature of the interaction between SU-8 and the NLC led to degenerate tangential BCs of the director field at the particles' surfaces. The system was then studied under various conditions inside parallel plate capacitor glass cells, with an inner separation gap d and normal BCs at the surfaces (induced by the SE1211 polyimide alignment layer), and observed using transmission polarised light microscopy. The devices were studied using a Leica DM2700P cross-polarising microscope with a $\times 50$ objective and imaged using an EO-23121C camera (Edmund Optics). Electrical addressing was performed by applying 10 kHz sine waves with increasing voltages using a 33622A (Keysight Technologies) arbitrary waveform generator across the samples. For the case of dynamic motion, an additional 0.5 Hz pulse envelope wave was used to switch between the on and off states. The voltage was monitored using a TDS2014 (Tektronix Inc.) oscilloscope and a 34419A (Keysight Technologies) digital voltmeter.

Simulations of nematic order tensor were performed using COMSOL 5.4a finite element analysis software through the minimization of the Landau-de Gennes free energy

$$F = \int_v \left(\frac{A}{2} Q_{ij} Q_{ij} + \frac{B}{3} Q_{ij} Q_{jk} Q_{ki} + \frac{C}{4} (Q_{ij} Q_{ij})^2 + \frac{L}{2} (Q_{ij,k})^2 - \frac{1}{2} \varepsilon_0 \varepsilon_{ij} V_i V_j \right) dv + \int_s W \left((\tilde{Q}_{ij} - \tilde{Q}_{ij}^\perp)^2 + (\tilde{Q}_{ij}^2 - S_0)^2 \right) ds. \quad (5.1)$$

Due to the complexity of the system, a time-dependent contribution was introduced to Equation (1.35) of the following form

$$\frac{\partial f}{\partial Q_{ij}} - \frac{\partial}{\partial x_k} \left(\frac{\partial f}{\partial Q_{ij,k}} \right) = -\gamma \frac{\partial Q_{ij}}{\partial t}, \quad (5.2)$$

where $\gamma = 0.67$ Pa·s is the numerical relaxation constant (directly proportional rotational viscosity) and t is the time coordinate. In our calculations, we set $A = -324$ kJ/m³, $B = -540$ kJ/m³, $C = 1800$ kJ/m³, $L = 12$ pN, $\varepsilon_{ij} = 3.8 \delta_{ij}$ for the particles, $\varepsilon_\perp = 8.4$ and $\varepsilon_\parallel = 38.1$ for the liquid crystal. These values correspond to an equilibrium order parameter of 0.6 and a nematic correlation length of 4 nm. Tangential BCs with strong anchoring were achieved by setting $W = 1$ cJ/m² = 10^{-4} pN/ μ m. Optimal configurations of the particles were found by simulating 10 s of dynamics, evaluating the resulting values of F across a range of particle tilt angles and locating the points at which it was minimised. This procedure was repeated for different values of d and V .

5.3 Quasistatic orientation

To minimise the free energy of the system, the liquid crystal director field must construct itself in a way that both satisfies the BCs on the contacting surfaces and minimises the elastic distortion in the bulk. From this, we can expect that the cuboid will assume an equilibrium at an angle to the plane of the cell such that there are defects on the top and bottom corners of the particle. By considering the symmetry properties of the particles, their orientation can usually be reduced to a single out of plane tilt angle, Φ_0 , in a particular vertical plane. For the case of cuboids, we assume that $\mathcal{T} \leq \mathcal{L} \leq \mathcal{W}$ and that the angular orientation occurs in the \mathcal{L} - \mathcal{T} plane. An example of this is shown in Figure 5.1b, where we see the optimal orientation of a cuboid shaped particle in the \mathcal{L} - \mathcal{T} plane. From the 2D simulations, we observe that Φ_0 depends on the particle's aspect ratio, \mathcal{L}/\mathcal{T} , as well as the relative size of the cell gap. For systems in which the particle's 2D diagonal length, $\mathcal{D}_{2D} = \sqrt{\mathcal{L}^2 + \mathcal{T}^2}$, is greater than d , Φ_0 is geometrically restricted to a certain range, beyond which it is physically impossible for the particle to tilt, which defines the blocked region in Figure 5.1c. In fact, two such regions exist: one in which the particle is able to lay in the plane of the cell, where $d \in [\mathcal{T}, \mathcal{D}_{2D})$, and the other in which the particle can stand perpendicular to it, where $d \in [\mathcal{L}, \mathcal{D}_{2D})$, which is shown as a secondary region in Figure 5.1c. However, the second possibility becomes increasingly unlikely as \mathcal{L}/\mathcal{T} is increased and has not been observed experimentally in our systems.

As the cell gap is increased, we observe an increase in the optimal tilt angle of the particles, both experimentally and numerically, which are in good agreement with each other, within the experimental error range. In 2D simulations, we see that, as d is increased further, Φ_0 quickly tends to an asymptote of Φ_0^∞ . While an analytical solution for this problem does not exist, we can describe the behaviour by approximating it with a suitable function that satisfies the key criteria. Firstly, there must exist a geometrically imposed characteristic cell gap, d_c , beyond which Φ_0 changes its course and tends to Φ_0^∞ . Additionally, we can deduce that because the function that describes the boundary of the restricted region has a non-zero gradient at $d = \mathcal{T}$, so should Φ_0 . The same argument can be used to show that Φ_0 must also have a non-linear increase below d_c . This leads to the following function in the simplest form

$$\Phi_0 = (\Phi_0^\infty - \alpha) \tanh \left(\left(\frac{d - \mathcal{T}}{d_c - \mathcal{T}} \right)^2 \right) + \alpha \tanh \left(\frac{d - \mathcal{T}}{d_c - \mathcal{T}} \right), \quad (5.3)$$

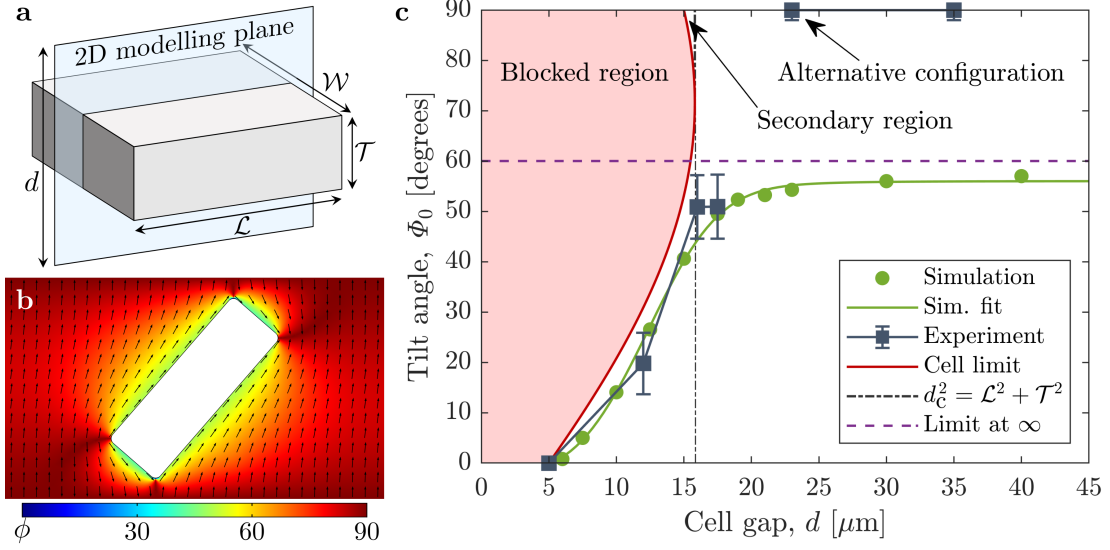


Figure 5.1: 2D numerical simulations of a cuboid shaped particle's out of plane tilt in cells filled with MLC-6204-000 NLC. (a) Schematic illustration of the 2D modelling plane for a cuboid shaped particle with length \mathcal{L} , thickness \mathcal{T} and depth \mathcal{W} inside a cell with a cell gap d . (b) Optimal orientation of a particle with tangential BCs ($\mathcal{L} = 15 \mu\text{m}$, $\mathcal{T} = 5 \mu\text{m}$) inside a nematic director field with normal BCs on top and bottom surfaces of the cell ($d = 17.5 \mu\text{m}$). Local nematic director field orientation is indicated with black arrows and its out of plane tilt, ϕ , is shown as a colour map from 0° (blue) to 90° (red). (c) Out of plane tilt of the same particle, Φ_0 , as a function of the cell gap, d . Optimal Φ_0 is shown in green circles for 2D numerical simulations and in blue squares for experimental results. Physically impossible values of Φ_0 are indicated by the red shaded region and the grey dot-dashed indicates the point where the system becomes geometrically unrestricted (where d is greater than the diagonal size of the particle). Violet dashed line indicates the infinite cell gap asymptote of 2D particle's tilt.

where α is a constant that is responsible for the non-zero gradient at $d = \mathcal{T}$. An example of this behaviour can be seen in Figure 5.1c, which shows the numerical results of the optimal orientation of a particle with $\mathcal{L} = 15 \mu\text{m}$, $\mathcal{T} = 5 \mu\text{m}$ as a function of d . Equation (2) fits this data with $\Phi_0^\infty = (56.0 \pm 0.9)^\circ$, $\alpha = (8.91 \pm 5.69)^\circ$ and $d_c = (15.6 \pm 0.3) \mu\text{m}$ (equal to \mathcal{D}_{2D} , considering the effect of the rounded corners) with an R-squared value of 0.999. By considering the limiting case of $d \gg \mathcal{L}, \mathcal{T}$, we observe that a pure balance of torques between \mathcal{L} and \mathcal{T} results in $\Phi_0^\infty \lesssim \arctan \sqrt{\mathcal{L}/\mathcal{T}}$, which is slightly decreased by the cross interactions of the two regions and the outer ends

of the particle. The full extent of this behaviour can be visualised by considering the dimensionless version of the system using Equation (5.3). Figure 5.2 illustrates the dependence of Φ_0 as a function of the dimensionless cell gap, d/\mathcal{T} , and the dimensionless length (aspect ratio) of the particle, \mathcal{L}/\mathcal{T} . However, once d becomes comparable to the full 3D diagonal length of the particle, the 2D approximation is no longer valid and the particles assume 3D configurations by also tilting in the $\mathcal{W}\text{-}\mathcal{T}$ plane.

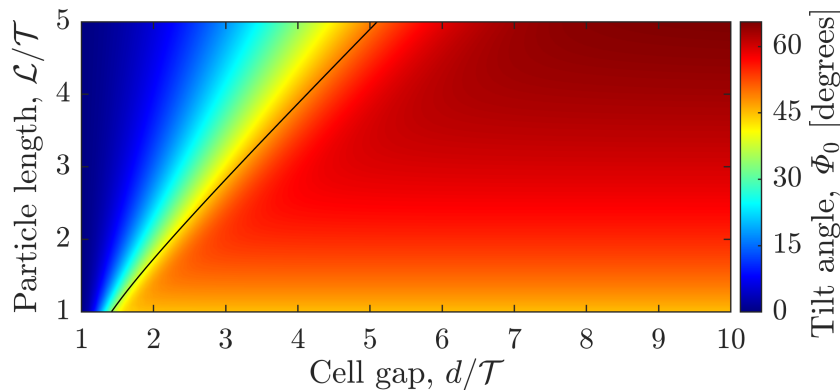


Figure 5.2: 2D out of plane tilt of a cuboid shaped particle in cells filled with MLC-6204-000 NLC, as a function of the dimensionless cell gap, d/\mathcal{T} , and the dimensionless particle length, \mathcal{L}/\mathcal{T} . Out of plane tilt of the particle, Φ_0 , is shown as a colour map from blue to red. The curve corresponding to the 2D diagonal length of the particle (and the end of the blocked region) is shown as a black line.

Due to the positive dielectric anisotropy of MLC-6204-000, applying an electric field across the system will begin to reorient the director to point parallel to the local voltage gradient. In turn, if $\mathcal{L} \neq \mathcal{T}$, this will impose an elastic torque on the particle and cause it to increase its out of plane tilt. As before, we can construct a function that closely approximates the solution by considering its key physical characteristics. Akin to the previous example, there exists a characteristic voltage, V_c , that determines the function's inflection point. However, the fact that the director has cylindrical symmetry implies that the voltage response must be described by a function that is even in V and has a Φ_0 intercept with a gradient of zero. The simplest function to describe this behaviour is

$$\Phi = (\Phi_\infty - \Phi_0) \left(1 - \exp \left(- \left(\frac{V}{V_c} \right)^2 \right) \right) + \Phi_0. \quad (5.4)$$

To allow maximal reorientation capabilities, d was chosen to be sufficiently large for Φ to be geometrically unrestricted but not so large that the particles stand up fully in

the unperturbed state. From our experiments, we find that the cuboids ($\mathcal{L} = \mathcal{W} = 15 \mu\text{m}$, $\mathcal{T} = 5 \mu\text{m}$) in $d = 17.5 \mu\text{m}$ cells are initially oriented at an angle of $(51 \pm 6)^\circ$, which increases with increasing applied voltage and tends to an asymptote of 90° (at infinite voltage). Equation (3) fits this data with $\Phi_\infty = (85.0 \pm 1.4)^\circ$, $\Phi_0 = (51.6 \pm 1.8)^\circ$ and $V_c = (1.40 \pm 0.14) \text{ V}$ with an R-squared value of 0.993. Results for this configuration are shown in Figure 5.3a, where the experimental data is also closely matched by the 2D simulations (within the experimental error bounds). Individual snapshots of the 2D simulation, corresponding to a minimised free energy configuration in the \mathcal{L} - \mathcal{T} plane, are shown for 0 V, 1 V and 3 V in Figure 5.3b.

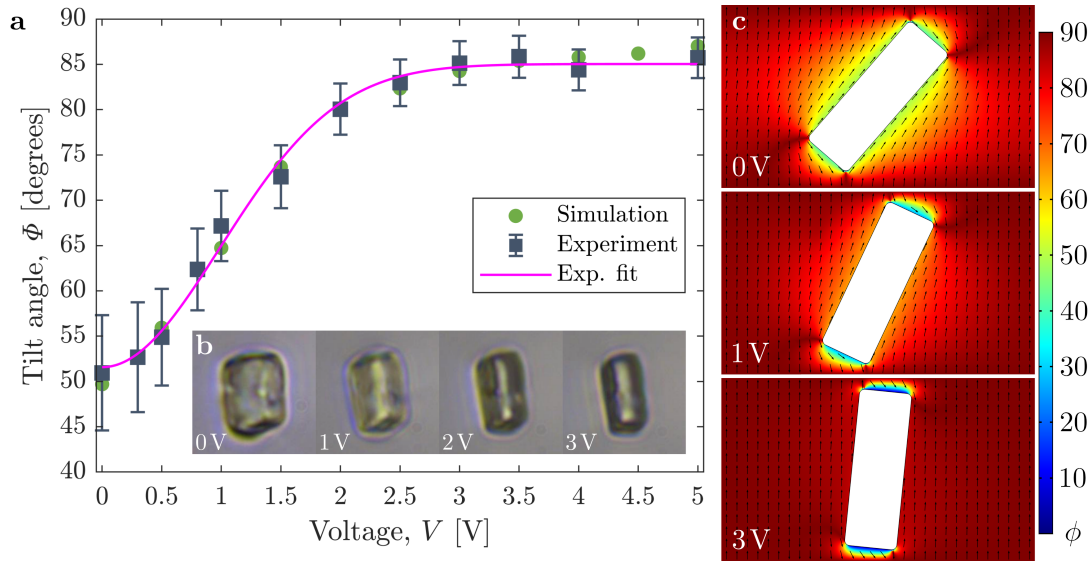


Figure 5.3: Experimental and numerical voltage dependence of a particle's out of plane tilt in a geometrically unrestricted cell filled with MLC-6204-000 NLC. (a) Optimal tilt angle of a particle with tangential BCs ($\mathcal{L} = 15 \mu\text{m}$, $\mathcal{T} = 5 \mu\text{m}$) in a cell ($d = 17.5 \mu\text{m}$) with normal BCs on top and bottom surfaces. 2D numerical simulation results are shown in green circles, experimental results are shown in blue squares and the corresponding experimental fit using Equation 5.4 is shown in magenta. (b) Optical microscopy photographs at 0 V, 1 V, 2 V and 3 V. (c) Numerical simulation results that correspond to the minimal energy configurations of the system at 0 V, 1 V and 3 V. Local nematic director field orientation is indicated with black arrows and its out of plane tilt, ϕ , is shown as a colour map from 0° (blue) to 90° (red). Voltage is applied perpendicular to the parallel plates of the cell (out of plane in (b), top and bottom edges in (c))

Since the system can be described by a balance of torques on the particle, we expect

that the window of angular operation must depend on \mathcal{L}/\mathcal{T} . This means that particles with large aspect ratios will require lower voltages to fully switch, but they will also have a lower range of possible Φ . On the other hand, the particles with a lower aspect ratio will have a greater range of possible Φ , but require higher voltages to achieve the same angular change. Alternatively, tangential BCs on all surfaces can be used to maximise the range of electrically controllable Φ in devices with $d > d_c$.

5.4 Restricted geometries and non-reciprocal motion

In systems where the particles are geometrically restricted from tilting beyond a certain angle, there exists an additional elastic counter torque on the particle to that of the voltage. Consequently, a higher voltage is required to change a given particle's tilt for thinner spaced cells. In Figure 5.4a we show that Φ increases with increasing external voltage and reaches the asymptote that is imposed by the geometry. Equation (5.4) fits this data with $\Phi_\infty = (30.9 \pm 1.1)^\circ$, $\Phi_0 = (20.5 \pm 2.1)^\circ$ and $V_c = (2.31 \pm 0.70)$ V with an R-squared value of 0.857. As the voltage is increased further, Φ remains unchanged. However, unlike the geometrically unrestricted case, at some point we can expect that the electric field will overpower the anchoring strength on the particle's surface and allow the defects to move around. Once a critical voltage is reached (44 V for cuboids with $\mathcal{L} = \mathcal{W} = 15 \mu\text{m}$, $\mathcal{T} = 5 \mu\text{m}$, in MLC-6204-000 filled cells with $d = 12 \mu\text{m}$), we observe a spontaneous change in the system. The defects break away from the corners/sides and swim towards the top and bottom faces of the particle (\mathcal{L} - \mathcal{W} plane), and the tilt suddenly drops to zero, as shown in Figures 5.4a-c.

While the state shown in Figure 5.4b is an equilibrium state for all systems, it only becomes stable when $d < d_c$ and at high voltages. Therefore, as the voltage is removed, the defects are guided back to the opposite corners by the free energy gradients and the particle must return to a tilted state (see Figure 5.1c). Depending on the path that each defect takes, the particles may also experience some rotation in the \mathcal{L} - \mathcal{W} plane. However, due to their geometrical symmetry, cuboid shaped particles tend to remain in roughly the same location and no motion is induced, as shown in Figures 5.5a and 5.5c. This was not the case for triangular prisms, since while they are topologically equivalent to cuboids, they don't have orthogonally opposing corners. When the voltage is removed, the director field relaxes and the defects move to the corners of the triangle,

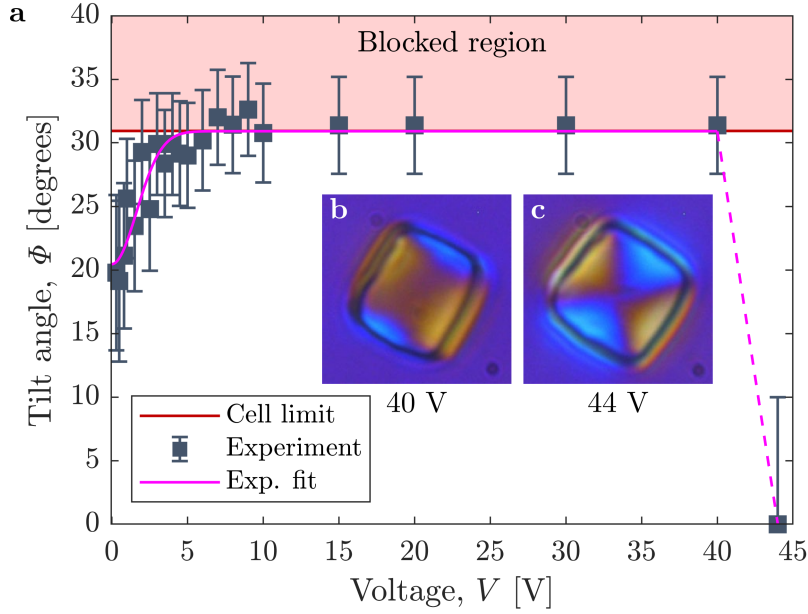


Figure 5.4: Experimental voltage dependence of a particle’s out of plane tilt in a constricted cell filled with MLC-6204-000 NLC. (a) Tilt angle of a cuboid shaped particle ($\mathcal{L} = 15 \mu\text{m}$, $\mathcal{T} = 5 \mu\text{m}$, $\mathcal{W} = 15 \mu\text{m}$) in a cell ($d = 12 \mu\text{m}$) with normal BCs on top and bottom surfaces. Geometrically restricted tilt angles are indicated by the shaded red region, experimental results are shown in blue squares and the corresponding fit is shown in magenta. (b and c) Optical polarized microscopy photographs at 40 V and 44 V of the same particle, showing the transition between tilted (b) and flat (c) orientations of the particle after passing the critical voltage for defect motion. Voltage is applied perpendicular to the image plane of (b) and (c). Crossed polarisers at South-North and West-East orientations with a full wave plate inserted between them at SW-NE orientation of the slow axis.

as shown in Figures 5.5b and 5.5d. By symmetry, the particle must move in the opposite direction to the net movement of the defects. Velocity of the particle decays exponentially from an initial velocity of $(117 \pm 26) \mu\text{m/s}$ with a reciprocal decay constant of $(29.6 \pm 2.8) \text{ms}$. This results in a non-reciprocal displacement of $(5.3 \pm 0.8) \mu\text{m}$ over the course of $(170 \pm 38) \text{ms}$, which closely matches the centroid to side distance of the particles’ triangular faces. Following this, the particles experience a drifting motion that is partially reciprocated by the subsequent tilting of the particles as they assume an equilibrium orientation at a distance of $(0.9 \pm 0.3) \mu\text{m}$ from the endpoint of the non-reciprocal displacement. An example of this is shown in Figure 5.6.

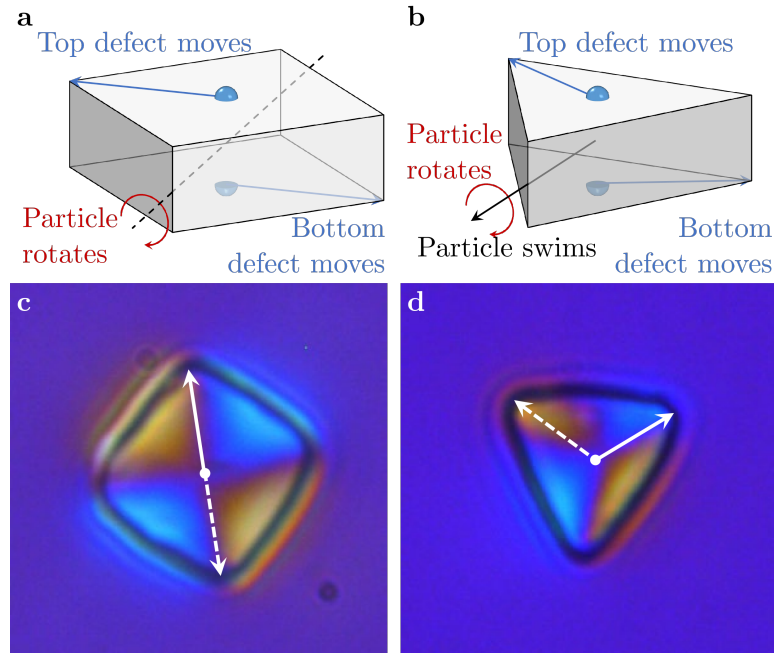


Figure 5.5: Dynamics of colloidal particles caused by the motion of topological defects after the removal of high voltage. (a and b) Schematic diagrams illustrating the motion of topological defects towards the opposite corners of the top and bottom faces of a cuboid and a triangular prism shaped particles and the subsequent dynamics of the particles after the removal of a high external voltage. Due to the direction of motion of the defects in each case, cuboids rotate along the axis that is perpendicular to the plane of motion of its topological defects. On the other hand, the net direction of defects' motion causes the triangles to swim in the opposite direction. (c and d) Optical polarized microscopy photographs of a cuboid ($\mathcal{L}=15\ \mu\text{m}$, $\mathcal{T}=5\ \mu\text{m}$, $\mathcal{W}=15\ \mu\text{m}$) and a triangular prism ($15\ \mu\text{m}$ side length, $T=5\ \mu\text{m}$) shaped particles at 44 V in a cell with $d=12\ \mu\text{m}$. Motion of the topological defects is indicated by the arrow directions. Crossed polarisers at South-North and West-East orientations with a full wave plate inserted between them at SW-NE orientation of the slow axis.

The manifestation of non-reciprocal motion is likely due to the sequence at which each event occurs in the system. When the particle is in the high tilt state, but the voltage is insufficient to break the surface anchoring of the defects, it is in close proximity to the boundaries of the cell (see Figure 5.4a). Since viscous forces are more prominent closer to the boundaries, the defects move through the reorientation of the director and the particles can only rotate when the critical voltage is applied, leaving little energy for

translation. On the other hand, when the particle is in the low tilt state, as shown in Figure 5.5d, it is far away from all boundaries and translational motion becomes much easier. Sudden removal of voltage leads to a much slower relaxation of the director and the decoupling between director reorientation and flow is lost. This allows the particle to swim first and rotate back to equilibrium later. This means that an on-off sequence of voltages (above the critical value) can be used to create discretised net motion of the particles in a particular direction.

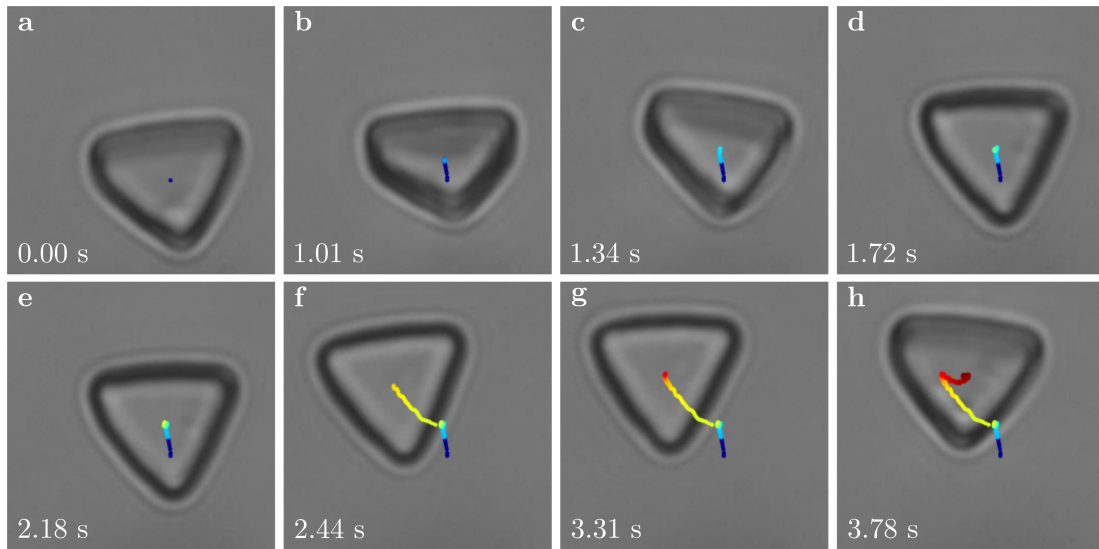


Figure 5.6: Image sequence showing positional tracking of a triangular prism. (a) No external voltage is applied. (b) Particle tilt increases when external voltage (below the critical value) is applied. (c) Increasing voltage beyond the critical value induces reorientation of the particle. (d) Highest symmetry axis of the particle fully aligns with the average electric field direction. (e) Voltage is removed. (f) Symmetric director configuration becomes unstable and the particle is laterally transposed. (g) Particle drifts further at a much slower velocity. (h) Particle partially reciprocates the drifting motion and tilts out of plane to assume an equilibrium state. Path line represents the positioning of the centroid as a colour coded function of time.

By considering the symmetry properties of the particles, we can deduce that translational motion should only occur in particles with an odd number of corners on their shape defining faces (assuming homogeneous thickness and regular convex polygonal faces). As the number of corners is increased, the maximal distance of translational motion is decreased. Since the defects are guided by the elastic free energy gradients to be as far away as possible from each other, equilateral triangular prisms

have the largest potential for translational motion (conversely, particles with irregular convex polygonal faces have a reduced travel potential). This can be emphasised by using hyperbolic triangles with concave edges of equal length, as they will have more prominent minimal energy paths for the defects to travel along. Furthermore, we can expect that the direction of motion can be controlled by using hyperbolic triangular prisms with two of the corners being sharper than the rest to act as designated docking stations for the defects.

5.5 Conclusion

In conclusion, we have investigated the effects of geometric symmetry on electrically induced quasi-static and dynamic reorientation and motion of particles with tangential BCs in NLCs. By considering the balance of torques, we have shown that these particles tilt at an angle that depends on the aspect ratio of the particles and their relative size to the cells containing them. Furthermore, the tilt angle can be controlled by applying an external electric field, through which the particles can assume a fully standing position in geometrically unrestricted systems. Similar behaviour is found in geometrically restricted systems. In this case, it is physically impossible for the particles to tilt beyond a certain angle and increasing the voltage past a critical value breaks the surface anchoring and allows the defects to relocate to the centres of the top and bottom faces of the particles. Removing the high voltage causes the defects to travel to the opposite corners of the particle, which allows it to assume a high tilt state. We observe that geometry plays a key role in the subsequent motion of the particles. By symmetry, the centroids of the cuboid shaped particles remain stationary during this process while the triangular particles are able to move in a direction that is perpendicular to that of the applied electric field. In fact, this process is non-reciprocal and the triangular prisms are able to travel forwards in a stop-motion-like fashion when an on-off sequence of high voltages is applied across the sample. These findings are beginning to show how both rotation and translation of particles can be controlled through the shape of the particle and its containment. Work is underway on providing different properties to the particle faces (including reflectance, fluorescence, absorption, and alignment) to produce a variety of functional particles controlled through the application of electric fields.

Chapter 6

Discussion

The main focus of this project was to investigate the effects of symmetry on the observable properties of liquid crystal systems. We start by providing a comprehensive introduction to the physics of liquid crystal systems and discussing their key characteristics. Following this, we use smectic-C liquid crystals to illustrate the importance of symmetry in monoclinic systems and discuss the effects of using orthorhombic approximations. In the subsequent chapter, we demonstrate the spontaneous self-assembly of fractal liquid crystal colloids and analyse their formation mechanisms. Finally, we combine experimental observations with numerical simulations to investigate the effects of geometry on electrically induced rotation and non-reciprocal motion of nematic liquid crystal colloids. The goal of this chapter is to provide an overview of this thesis by reviewing the key findings from each chapter and discussing the outlook of future projects.

In Chapter 3, we consider the effects of monoclinic symmetry on observable properties of biaxial liquid crystal phases. The concept of monoclinic symmetry is hypothesised in other studies, but due to the difficulty in distinguishing its effects experimentally, it is often overlooked. Here, we utilise the inherent monoclinic symmetry of the smectic-C phase to demonstrate its effects on the observable properties of the phase. Through a series of symmetry arguments, we show that the eigenframes of different physical properties do not necessarily coincide in monoclinic systems. In the case of the smectic-C phase, this is interpreted as a disassociation of the individual cone angles that correspond to unique observable properties of the system. This allows us to define a measure of monoclinic symmetry as the difference between optical and dielectric cone angles, $\partial\theta$. The results show that smectic-C liquid crystals can exhibit a high

degree of monoclinic symmetry and the dielectric cone angle can differ significantly from its optical counterpart. In turn, this indicates that other physical properties, such as dielectric biaxiality and switching speeds, are potentially mischaracterised in studies that assume orthorhombic symmetry of the smectic-C phase.

The results of our research would benefit from performing X-ray scattering experiments on our samples to determine the layer tilt as a function of temperature. This would allow us to disassociate the steric eigenframe from that of optics and dielectrics and provide us with better cone angle measurements. Furthermore, measuring the cone angles that correspond to all of the other physical properties would allow us to further understand the effects of monoclinic symmetry in biaxial liquid crystals. In principle, our method can be extended to other liquid crystal phases with potential monoclinic symmetry, such as some nematic and smectic-A phases consisting of non-calamitic molecules (see Ref.^[19]).

In Chapter 4, we investigate the self-assembly of fractal liquid crystal colloids in nematic droplets with normal boundary conditions. First, we consider a basic system, formed by a distribution of small satellite inclusions around a larger core inclusion. Through a series of symmetry arguments, we show that the satellites distribute themselves around the primary orbit of the core in configurations that can be described by the solutions to the Thomson problem. Using numerical simulations of the nematic director, we show that each satellite comes with its own distortion profile that can be assumed to be independent of the core to satellite size ratio, r . This suggests that systems with larger values of r can allow a greater number of satellites to enter the primary orbit of the system. However, with every docked satellite, the likelihood of subsequent satellites entering the primary orbit rapidly decreases. These satellites then attach themselves onto the existing satellites, forming linear chains that extend radially outwards from the core. Following this, we show that the satellites themselves can act as secondary cores for smaller satellites and create fractal structures. Experimentally, we observe fractal structures with up to three (optically distinguishable) steps of evolution. Furthermore, we find that a distribution of droplet sizes plays a key role in determining the symmetry properties of the self-assembled structures. We also show that it is possible to switch between different satellite configurations with external stimuli. The results are relevant to a variety of inclusions, ranging from colloidal suspensions to multi-emulsion systems. Such systems have potential applications for novel switchable

photonic structures as well as providing wider insights into the packing of self-assembled structures in general.

The goal of this study was to illustrate the mechanisms behind the self-assembly process of fractal liquid crystal colloids. For simplicity, we assumed that the distances between the satellites are determined by a size-dependent separation factor (based on experimental measurements) and modelled the systems using vector representation of the director. A natural extension to this study is repeat the numerical simulations using the order tensor representation and determine the optimal core to satellite separation factor for each configuration. This would allow us to accurately determine the maximal orbit capacity for each value of r . Furthermore, it would be interesting to investigate more general cases of our system, such as using conical boundary conditions, non-spherical inclusions and non-spherical domains.

In Chapter 5, we study effects of geometry on electrically induced rotation and non-reciprocal motion of colloidal particles in parallel plate capacitor cells filled with nematic liquid crystals. The systems are modelled using the order tensor representation, which shows excellent agreement with the corresponding experimental results. We find that the optimal orientation of the particles is determined by their aspect ratios and their size relative to the cells containing them. Furthermore, the out of plane tilt of the particles, Φ , can be controlled by an external electric field. In systems that allow unrestricted particle rotation, the long axes of the particles are able to fully align themselves with the external electric field vector (when the voltage is sufficiently large). However, when the inner separation gap of the containing cells is smaller than the diagonal length of the particles, Φ is geometrically restricted. In this case, increasing the voltage beyond its critical value partially breaks the surface anchoring and allows the defects to relocate to a more symmetric configuration within the system. To minimise the free energy of the system, the highest symmetry axis of each particle must align itself with the electric field vector, causing a discontinuous change in Φ to 0. Removing the voltage causes the system to relax to its original state through the relaxation of the director to a minimal energy state, which is achieved when the distance between the defects is maximised. We observe that each particle moves in the opposite direction to the net motion of its defects, which is governed by the geometric symmetry of the system. Our results indicate that only particles with an odd number of corners on their shape defining faces can exhibit translational motion. In fact, the motion appears

to be non-reciprocal and the particles are able to move in a stop-motion-like fashion. Furthermore, we propose a possible mechanism based on the sequence of events that occur within the systems to explain our observations. Our results have a variety of potential applications in deliberate manipulation of colloidal particles for engineering functional materials.

In this study, we successfully model the rotational motion of the particles and propose empirical functions to describe our results based on key characteristic properties of our systems. For simplicity, we modelled the dominant cross-section of the particles, which cannot account for the possible three-dimensional configurations in systems with larger cell gaps. Additionally, the physical particles resembled truncated pyramids with trapezoid-like cross-sections, which further promoted alternative configurations. In principle, the geometry of the particles can be accurately determined with scanning electron microscopy and directly imported into the simulations. This would allow us to accurately determine the physics of our specific systems. Furthermore, our systems can be used to determine the anchoring strengths of materials that promote tangential boundary conditions by determining the voltages at which the defects are able to leave their designated corners and comparing them to the corresponding numerical results. In the study, we determine that equilateral triangular prisms have the highest potential for non-reciprocal motion and discuss the possibility of using hyperbolic shapes to improve the consistency of this mechanism. A natural extension to this study is to investigate this possibility experimentally and numerically using three-dimensional simulations. Additionally, the non-reciprocal component of our results requires further theoretical analysis.

References

- [1] D. J. Gross, “The role of symmetry in fundamental physics,” *Proceedings of the National Academy of Sciences*, vol. 93, no. 25, pp. 14256–14259, 1996.
- [2] P. G. de Gennes and J. Prost, *The Physics of Liquid Crystals*. International Series of Monographs on Physics, Clarendon Press, 1995.
- [3] R. Virchow, “Ueber das ausgebreitete vorkommen einer dem nervenmark analogen substanz in den thierischen gewebe,” *Virchows Archiv*, vol. 6, no. 4, pp. 562–572, 1854.
- [4] C. Mettenheimer, “Mikroskopische beobachtungen mit polarisiertem licht,” *Korrespondenzbl. d. Ver. f. gemeins. Arb. z. Ford. d. wissenschaftl. Heilk.*, vol. 24, p. 331, 1857.
- [5] F. Reinitzer, “Beiträge zur kenntniss des cholesterins,” *Monatsh. Chem.*, vol. 9, pp. 421–441, 1888.
- [6] O. Lehmann, “Über fließende krystalle,” *Z. Phys. Chem*, vol. 4, pp. 462–472, 1889.
- [7] A. Jáklí and A. Saupe, *One-and Two-Dimensional Fluids: Properties of smectic, lamellar and columnar liquid crystals*. CRC Press, 2006.
- [8] R. P. Feynman, R. B. Leighton, and M. Sands, *The Feynman Lectures on Physics, Desktop Edition Volume I*, vol. 1. Basic books, 2013.
- [9] D. S. Schonland, *Molecular symmetry: an introduction to group theory and its uses in chemistry*. Van Nostrand, 1965.
- [10] P. Curie, “Sur la symétrie dans les phénomènes physiques, symétrie d’un champ électrique et d’un champ magnétique,” *Journal de physique théorique et appliquée*, vol. 3, no. 1, pp. 393–415, 1894.

- [11] T. Rowland and E. W. Weisstein, "Group." <http://mathworld.wolfram.com/Group.html>. Accessed on 22 August 2016.
- [12] J. W. Goodby, P. J. Collings, H. Gleeson, T. Kato, P. Raynes, and C. Tschierske, *Handbook of liquid crystals*, vol. 1. Wiley-VCH, 2 ed., 2014.
- [13] L. M. Blinov, *Structure and properties of liquid crystals*. Springer Science & Business Media, 2011.
- [14] J. R. Ferraro and J. S. Ziomek, *Introductory Group Theory; and Its Application to Molecular Structures*. Plenum Press, 1969.
- [15] G. B. Arfken, H. J. Weber, and F. E. Harris, *Mathematical Methods for Physicists: A Comprehensive Guide*. Academic Press, 7 ed., 2013.
- [16] Z. Zhang, S. Kaur, B. Kundu, B. Sadashiva, and H. Gleeson, "Observing the emergence of phase biaxiality in a polar smectic a system via polarised raman spectroscopy," *Journal of Materials Chemistry C*, vol. 5, no. 5, pp. 1195–1205, 2017.
- [17] R. A. Reddy, C. Zhu, R. Shao, E. Korblova, T. Gong, Y. Shen, E. Garcia, M. A. Glaser, J. E. Maclennan, D. M. Walba, *et al.*, "Spontaneous ferroelectric order in a bent-core smectic liquid crystal of fluid orthorhombic layers," *Science*, vol. 332, no. 6025, pp. 72–77, 2011.
- [18] A. G. Vanakaras and D. J. Photinos, "Thermotropic biaxial nematic liquid crystals: Spontaneous or field stabilized?," *The Journal of Chemical Physics*, vol. 128, no. 15, p. 154512, 2008.
- [19] C. Tschierske and D. J. Photinos, "Biaxial nematic phases," *J. Mater. Chem.*, vol. 20, pp. 4263–4294, 2010.
- [20] T. Niori, T. Sekine, J. Watanabe, T. Furukawa, and H. Takezoe, "Distinct ferroelectric smectic liquid crystals consisting of banana shaped achiral molecules," *Journal of materials chemistry*, vol. 6, pp. 1231–1233, 1996.
- [21] Y. Shimbo, E. Gorecka, D. Pocięcha, F. Araoka, M. Goto, Y. Takanishi, K. Ishikawa, J. Mieczkowski, K. Gomola, and H. Takezoe, "Electric-field-induced

- polar biaxial order in a nontilted smectic phase of an asymmetric bent-core liquid crystal,” *Phys. Rev. Lett.*, vol. 97, p. 113901, Sep 2006.
- [22] G. R. Luckhurst, S. Naemura, T. J. Sluckin, T. B. T. To, and S. Turzi, “Molecular field theory for biaxial nematic liquid crystals composed of molecules with C_{2h} point group symmetry,” *Phys. Rev. E*, vol. 84, p. 011704, Jul 2011.
- [23] P. K. Karahaliou, A. G. Vanakaras, and D. J. Photinos, “Symmetries and alignment of biaxial nematic liquid crystals,” *The Journal of chemical physics*, vol. 131, no. 12, p. 124516, 2009.
- [24] W. L. McMillan, “Simple molecular theory of the smectic c phase,” *Physical Review A*, vol. 8, pp. 1921–1929, Oct 1973.
- [25] A. Wulf, “Steric model for the smectic-c phase,” *Physical Review A*, vol. 11, pp. 365–375, Jan 1975.
- [26] S. Jen, N. A. Clark, P. S. Pershan, and E. Priestley, “Raman scattering from a nematic liquid crystal: Orientational statistics,” *Physical Review Letters*, vol. 31, no. 26, p. 1552, 1973.
- [27] P. Davidson, D. Petermann, and A. Levelut, “The measurement of the nematic order parameter by x-ray scattering reconsidered,” *Journal de Physique II*, vol. 5, no. 1, pp. 113–131, 1995.
- [28] R. J. Mandle and A. Mertelj, “Orientational order in the splay nematic ground state,” *Physical Chemistry Chemical Physics*, vol. 21, no. 34, pp. 18769–18772, 2019.
- [29] M. Kohli, K. Otnes, R. Pynn, and T. Riste, “Investigation of nematic order by coherent neutron scattering,” *Zeitschrift für Physik B Condensed Matter*, vol. 24, no. 2, pp. 147–152, 1976.
- [30] G. R. Luckhurst and R. N. Yeates, “Orientational order of a spin probe dissolved in nematic liquid crystals. an electron resonance investigation,” *Journal of the Chemical Society, Faraday Transactions 2: Molecular and Chemical Physics*, vol. 72, pp. 996–1009, 1976.

- [31] A. Zeminder, S. Paul, and R. Paul, "Refractive indices and orientational order parameter of five liquid crystals in nematic phase," *Molecular Crystals and Liquid Crystals*, vol. 61, no. 3–4, pp. 191–206, 1980.
- [32] R. Richardson, J. Allman, and G. McIntyre, "Neutron scattering from mixtures of isotopically labelled molecules. a new method for determining the orientational distribution function in liquid crystals," *Liquid Crystals*, vol. 7, no. 5, pp. 701–719, 1990.
- [33] I. Chirtoc, M. Chirtoc, C. Glorieux, and J. Thoen, "Determination of the order parameter and its critical exponent for n_{cb} (n= 5–8) liquid crystals from refractive index data," *Liquid crystals*, vol. 31, no. 2, pp. 229–240, 2004.
- [34] W. Maier and A. Saupe, "Eine einfache molekular-statistische theorie der nematischen kristallinflüssigen phase. teil ii," *Zeitschrift für Naturforschung A*, vol. 15, no. 4, pp. 287–292, 1960.
- [35] R. Humphries, P. James, and G. Luckhurst, "A molecular field treatment of liquid crystalline mixtures," in *Symposia of the Faraday Society*, vol. 5, pp. 107–118, Royal Society of Chemistry, 1971.
- [36] J. V. Selinger, *Introduction to the theory of soft matter: from ideal gases to liquid crystals*. Springer, 2015.
- [37] N. J. Mottram and C. J. P. Newton, "Introduction to Q-tensor theory," 2014.
- [38] Ž. Kos, J. Aplinc, U. Mur, and M. Ravnik, *Mesoscopic Approach to Nematic Fluids*, pp. 51–93. Springer International Publishing, 2019.
- [39] L. Landau, "Zur theorie der phasenumwandlungen ii," *Phys. Z. Sowjetunion*, vol. 11, no. 545, pp. 26–35, 1937.
- [40] L. D. Landau, E. M. Lifshitz, J. B. Sykes, and M. J. Kearsley, *Statistical physics*. Pergamon Press, 2 ed., 1969.
- [41] I. W. Stewart, *The static and dynamic continuum theory of liquid crystals: a mathematical introduction*. CRC Press, 2014.
- [42] F. C. Frank, "I. liquid crystals. on the theory of liquid crystals," *Discussions of the Faraday Society*, vol. 25, pp. 19–28, 1958.

- [43] J. V. Selinger, “Interpretation of saddle-splay and the oseen-frank free energy in liquid crystals,” *Liquid Crystals Reviews*, vol. 6, no. 2, pp. 129–142, 2018.
- [44] M. Ravnik and S. Žumer, “Landau–de gennes modelling of nematic liquid crystal colloids,” *Liquid Crystals*, vol. 36, no. 10–11, pp. 1201–1214, 2009.
- [45] A. M. Sonnet and E. G. Virga, *Dissipative ordered fluids: Theories for Liquid Crystals*. Springer Science & Business Media, 2012.
- [46] F. Leslie, I. Stewart, and M. Nakagawa, “A continuum theory for smectic c liquid crystals,” *Molecular Crystals and Liquid Crystals*, vol. 198, no. 1, pp. 443–454, 1991.
- [47] A. Rapini and M. Papoular, “Distorsion d’une lamelle nématique sous champ magnétique conditions d’ancrage aux parois,” *Le Journal de Physique Colloques*, vol. 30, no. C4, pp. C4–54, 1969.
- [48] M. Nobili and G. Durand, “Disorientation-induced disordering at a nematic-liquid-crystal-solid interface,” *Physical Review A*, vol. 46, no. 10, p. R6174, 1992.
- [49] J.-B. Fournier and P. Galatola, “Modeling planar degenerate wetting and anchoring in nematic liquid crystals,” *Europhysics Letters*, vol. 72, no. 3, pp. 403–409, 2005.
- [50] R. B. Meyer, “Piezoelectric effects in liquid crystals,” *Physical Review Letters*, vol. 22, pp. 918–921, May 1969.
- [51] R. B. Meyer, “Ferroelectric liquid crystals; a review,” *Molecular Crystals and Liquid Crystals*, vol. 40, no. 1, pp. 33–48, 1977.
- [52] L. Beresnev, V. Chigrinov, D. Dergachev, E. Poshidaev, J. Fünfschilling, and M. Schadt, “Deformed helix ferroelectric liquid crystal display: a new electrooptic mode in ferroelectric chiral smectic c liquid crystals,” *Liquid Crystals*, vol. 5, no. 4, pp. 1171–1177, 1989.
- [53] N. A. Clark and S. T. Lagerwall, “Submicrosecond bistable electro-optic switching in liquid crystals,” *Applied Physics Letters*, vol. 36, no. 11, pp. 899–901, 1980.
- [54] D. R. Link, G. Natale, R. Shao, J. E. MacLennan, N. A. Clark, E. Körblova, and D. M. Walba, “Spontaneous formation of macroscopic chiral domains in a fluid

- smectic phase of achiral molecules,” *Science*, vol. 278, no. 5345, pp. 1924–1927, 1997.
- [55] W. P. Thurston, *Three-dimensional geometry and topology*, vol. 1. Princeton University Press, 1997.
- [56] G. F. Ellis, “Topology and cosmology,” *General Relativity and Gravitation*, vol. 2, no. 1, pp. 7–21, 1971.
- [57] H. Zhang, C.-X. Liu, X.-L. Qi, X. Dai, Z. Fang, and S.-C. Zhang, “Topological insulators in bi_2se_3 , bi_2te_3 and sb_2te_3 with a single dirac cone on the surface,” *Nature physics*, vol. 5, no. 6, p. 438, 2009.
- [58] J. Helman and L. Hesselink, “Representation and display of vector field topology in fluid flow data sets,” *Computer*, no. 8, pp. 27–36, 1989.
- [59] N. D. Mermin, “The topological theory of defects in ordered media,” *Rev. Mod. Phys.*, vol. 51, pp. 591–648, 1979.
- [60] M. Kleman and O. D. Lavrentovich, “Topological point defects in nematic liquid crystals,” *Philosophical Magazine*, vol. 86, no. 25–26, pp. 4117–4137, 2006.
- [61] H. Stark, “Physics of colloidal dispersions in nematic liquid crystals,” *Physics Reports*, vol. 351, no. 6, pp. 387–474, 2001.
- [62] O. D. Lavrentovich, “Topological defects in dispersed words and worlds around liquid crystals, or liquid crystal drops,” *Liquid crystals*, vol. 24, no. 1, pp. 117–126, 1998.
- [63] H. Stark, “Director field configurations around a spherical particle in a nematic liquid crystal,” *The European Physical Journal B-Condensed Matter and Complex Systems*, vol. 10, no. 2, pp. 311–321, 1999.
- [64] N. Schopohl and T. J. Sluckin, “Defect core structure in nematic liquid crystals,” *Phys. Rev. Lett.*, vol. 59, pp. 2582–2584, 1987.
- [65] G. P. Alexander, B. G.-g. Chen, E. A. Matsumoto, and R. D. Kamien, “Colloquium: Disclination loops, point defects, and all that in nematic liquid crystals,” *Rev. Mod. Phys.*, vol. 84, pp. 497–514, 2012.

- [66] G. Bryan-Brown, C. Brown, J. Jones, E. Wood, I. Sage, P. Brett, and J. Rudin, “Grating aligned bistable nematic device,” in *SID International Symposium Digest of Technical Papers*, vol. 28, pp. 37–40, Society for Information Display, 1997.
- [67] J. C. Jones, “The zenithal bistable display: From concept to consumer,” *Journal of the Society for Information Display*, vol. 16, no. 1, pp. 143–154, 2008.
- [68] T. J. Spencer, C. M. Care, R. M. Amos, and J. C. Jones, “Zenithal bistable device: Comparison of modeling and experiment,” *Physical Review E*, vol. 82, p. 021702, Aug 2010.
- [69] T. Needham, *Visual complex analysis*. Oxford University Press, 1998.
- [70] R. Schinzinger and P. A. A. Laura, *Conformal mapping: methods and applications*. Dover Publications, 2003.
- [71] A. Davidson and N. Mottram, “Conformal mapping techniques for the modelling of liquid crystal devices,” *European Journal of Applied Mathematics*, vol. 23, no. 1, pp. 99–119, 2012.
- [72] H. P. Langtangen and S. Linge, *Finite difference computing with PDEs: a modern software approach*, vol. 16. Springer, 2017.
- [73] I. Babuska, J. Whiteman, and T. Strouboulis, *Finite elements: an introduction to the method and error estimation*. Oxford University Press, 2010.
- [74] E. Raynes, C. Brown, and J. Strömer, “Method for the measurement of the k_{22} nematic elastic constant,” *Applied physics letters*, vol. 82, no. 1, pp. 13–15, 2003.
- [75] V. Fréedericksz and A. Repiewa, “Theoretisches und experimentelles zur frage nach der natur der anisotropen flüssigkeiten,” *Zeitschrift für Physik*, vol. 42, no. 7, pp. 532–546, 1927.
- [76] O. Lavrentovich, “Fluorescence confocal polarizing microscopy: three-dimensional imaging of the director,” *Pramana*, vol. 61, no. 2, pp. 373–384, 2003.
- [77] K. Welford and J. Sambles, “Analysis of electric field induced deformations in a nematic liquid crystal for any applied field,” *Molecular Crystals and Liquid Crystals*, vol. 147, no. 1, pp. 25–42, 1987.

- [78] J. Li, C.-H. Wen, S. Gauza, R. Lu, and S.-T. Wu, “Refractive indices of liquid crystals for display applications,” *Journal of Display Technology*, vol. 1, no. 1, p. 51, 2005.
- [79] B. E. Sørensen, “A revised michel-lévy interference colour chart based on first-principles calculations,” *European Journal of Mineralogy*, vol. 25, no. 1, pp. 5–10, 2012.
- [80] N. V. Solodkov, M. Nagaraj, and J. C. Jones, “Effects of monoclinic symmetry on the properties of biaxial liquid crystals,” *Phys. Rev. E*, vol. 97, p. 042702, 2018.
- [81] N. V. Solodkov, M. Hird, and J. C. Jones, “Alignment and electro-optical properties of smc* with direct transition to n* phases,” *Molecular Crystals and Liquid Crystals*, vol. 647, no. 1, pp. 162–168, 2017.
- [82] J. C. Jones, “On the biaxiality of smectic c and ferroelectric liquid crystals,” *Liquid Crystals*, 2015.
- [83] J. C. Jones and E. P. Raynes, “Measurement of the biaxial permittivities for several smectic c host materials used in ferroelectric liquid crystal devices,” *Liquid Crystals*, vol. 11, no. 2, pp. 199–217, 1992.
- [84] J. Hoffmann, W. Kuczynski, J. Malecki, and J. Pavel, “The determination of dielectric anisotropy in ferroelectric smectic c,” *Ferroelectrics*, vol. 76, no. 1, pp. 61–67, 1987.
- [85] F. Gouda, W. Kuczynski, S. T. Lagerwall, M. Matuszczyk, T. Matuszczyk, and K. Sarp, “Determination of the dielectric biaxiality in a chiral smectic-c phase,” *Phys. Rev. A*, vol. 46, pp. 951–958, Jul 1992.
- [86] T. Rieker, N. Clark, G. Smith, D. Parmar, E. Sirota, and C. Safinya, “Chevron local layer structure in surface-stabilized ferroelectric smectic-c cells,” *Physical review letters*, vol. 59, no. 23, p. 2658, 1987.
- [87] L. D. Landau, E. M. Lifshitz, J. B. Sykes, and J. S. Bell, *Electrodynamics of continuous media*. Pergamon Press, 1961.
- [88] D. C. Lay, *Linear algebra and its applications*. Addison Wesley Boston, MA, 4 ed., 2012.

- [89] M. Hird, “Ferroelectricity in liquid crystals—materials, properties and applications,” *Liquid Crystals*, vol. 38, no. 11–12, pp. 1467–1493, 2011.
- [90] M. E. Glendenning, J. W. Goodby, M. Hird, and K. J. Toyne, “The synthesis and mesomorphic properties of 2, 2', 3-tri-and 2, 2', 3, 3'-tetra-fluoro-1, 1': 4', 1"-terphenyls for high dielectric biaxiality ferroelectric liquid crystal mixtures,” *Journal of the Chemical Society, Perkin Transactions 2*, no. 3, pp. 481–492, 1999.
- [91] K. H. Yang, A. Lien, and T. C. Chieu, “Optical methods for the measurement of layer-tilt and pretilt angles in surface-stabilized ferroelectric liquid crystal devices,” *Japanese Journal of Applied Physics*, vol. 27, no. 11R, p. 2022, 1988.
- [92] J. Jones, E. Raynes, M. Towler, and J. Sambles, “Dielectric biaxiality in sc host systems,” *Molecular Crystals and Liquid Crystals*, vol. 199, no. 1, pp. 277–285, 1991.
- [93] N. V. Solodkov, J.-u. Shim, and J. C. Jones, “Self-assembly of fractal liquid crystal colloids,” *Nature Communications*, vol. 10, no. 1, p. 198, 2019.
- [94] C. P. Lapointe, T. G. Mason, and I. I. Smalyukh, “Shape-controlled colloidal interactions in nematic liquid crystals,” *Science*, vol. 326, no. 5956, pp. 1083–1086, 2009.
- [95] P. Poulin, H. Stark, T. Lubensky, and D. Weitz, “Novel colloidal interactions in anisotropic fluids,” *Science*, vol. 275, no. 5307, pp. 1770–1773, 1997.
- [96] T. C. Lubensky, D. Pettey, N. Currier, and H. Stark, “Topological defects and interactions in nematic emulsions,” *Phys. Rev. E*, vol. 57, pp. 610–625, Jan 1998.
- [97] F. Li, D. P. Josephson, and A. Stein, “Colloidal assembly: The road from particles to colloidal molecules and crystals,” *Angewandte Chemie International Edition*, vol. 50, no. 2, pp. 360–388, 2011.
- [98] I. Muševič, M. Škarabot, U. Tkalec, M. Ravnik, and S. Žumer, “Two-dimensional nematic colloidal crystals self-assembled by topological defects,” *Science*, vol. 313, no. 5789, pp. 954–958, 2006.
- [99] G. Posnjak, S. Čopar, and I. Muševič, “Hidden topological constellations and polyvalent charges in chiral nematic droplets,” *Nature communications*, vol. 8, p. 14594, 2017.

- [100] I. Muševič and M. Škarabot, “Self-assembly of nematic colloids,” *Soft Matter*, vol. 4, no. 2, pp. 195–199, 2008.
- [101] A. Nych, U. Ognysta, M. Škarabot, M. Ravnik, S. Žumer, and I. Muševič, “Assembly and control of 3D nematic dipolar colloidal crystals,” *Nature Communications*, vol. 4, p. 1489, 2013.
- [102] Q. Liu, B. Senyuk, M. Tasinkevych, and I. I. Smalyukh, “Nematic liquid crystal boojums with handles on colloidal handlebodies,” *Proceedings of the National Academy of Sciences*, vol. 110, no. 23, pp. 9231–9236, 2013.
- [103] L. Whyte, “Unique arrangements of points on a sphere,” *The American Mathematical Monthly*, vol. 59, no. 9, pp. 606–611, 1952.
- [104] J. J. Thomson, “Xxiv. on the structure of the atom: an investigation of the stability and periods of oscillation of a number of corpuscles arranged at equal intervals around the circumference of a circle; with application of the results to the theory of atomic structure,” *The London, Edinburgh, and Dublin Philosophical Magazine and Journal of Science*, vol. 7, no. 39, pp. 237–265, 1904.
- [105] S. Hashemi, U. Jagodič, M. Mozaffari, M. Ejtehadi, I. Muševič, and M. Ravnik, “Fractal nematic colloids,” *Nature communications*, vol. 8, no. 1, pp. 1–9, 2017.
- [106] D. C. Duffy, J. C. McDonald, O. J. Schueller, and G. M. Whitesides, “Rapid prototyping of microfluidic systems in poly (dimethylsiloxane),” *Analytical chemistry*, vol. 70, no. 23, pp. 4974–4984, 1998.
- [107] J.-i. Fukuda, H. Stark, M. Yoneya, and H. Yokoyama, “Interaction between two spherical particles in a nematic liquid crystal,” *Physical Review E*, vol. 69, p. 041706, Apr 2004.
- [108] K. Takahashi, M. Ichikawa, and Y. Kimura, “Force between colloidal particles in a nematic liquid crystal studied by optical tweezers,” *Phys. Rev. E*, vol. 77, p. 020703, Feb 2008.
- [109] C. O. Tan, M. A. Cohen, D. L. Eckberg, and J. A. Taylor, “Fractal properties of human heart period variability: physiological and methodological implications,” *The Journal of Physiology*, vol. 587, no. 15, pp. 3929–3941, 2009.

- [110] P. Meakin, "Formation of fractal clusters and networks by irreversible diffusion-limited aggregation," *Physical Review Letters*, vol. 51, pp. 1119–1122, Sep 1983.
- [111] B. B. Mandelbrot and J. W. Van Ness, "Fractional brownian motions, fractional noises and applications," *SIAM review*, vol. 10, no. 4, pp. 422–437, 1968.
- [112] B. B. Mandelbrot, *The Fractal Geometry Of Nature*. W.H. Freeman and Company, 1982.
- [113] K. Falconer, *Fractal geometry: mathematical foundations and applications*. John Wiley & Sons, 2004.
- [114] V. N. Manoharan, "Colloidal matter: Packing, geometry, and entropy," *Science*, vol. 349, no. 6251, 2015.
- [115] W. J. Parak, D. Gerion, T. Pellegrino, D. Zanchet, C. Micheel, S. C. Williams, R. Boudreau, M. A. L. Gros, C. A. Larabell, and A. P. Alivisatos, "Biological applications of colloidal nanocrystals," *Nanotechnology*, vol. 14, no. 7, pp. R15–R27, 2003.
- [116] J. R. Lakowicz, "Plasmonics in biology and plasmon-controlled fluorescence," *Plasmonics*, vol. 1, no. 1, pp. 5–33, 2006.
- [117] F. Zhang, H. Zhong, C. Chen, X.-g. Wu, X. Hu, H. Huang, J. Han, B. Zou, and Y. Dong, "Brightly luminescent and color-tunable colloidal $\text{ch}_3\text{nh}_3\text{pbx}_3$ ($x = \text{br}, \text{i}, \text{cl}$) quantum dots: Potential alternatives for display technology," *ACS Nano*, vol. 9, no. 4, pp. 4533–4542, 2015.
- [118] H. Huang, L. Polavarapu, J. A. Sichert, A. S. Susha, A. S. Urban, and A. L. Rogach, "Colloidal lead halide perovskite nanocrystals: synthesis, optical properties and applications," *NPG Asia Materials*, vol. 8, no. 11, p. e328, 2016.
- [119] B. Comiskey, J. D. Albert, H. Yoshizawa, and J. Jacobson, "An electrophoretic ink for all-printed reflective electronic displays," *Nature*, vol. 394, no. 6690, p. 253, 1998.
- [120] Y. Fang and M. Sun, "Nanoplasmonic waveguides: towards applications in integrated nanophotonic circuits," *Light: Science & Applications*, vol. 4, no. 6, p. e294, 2015.

- [121] S. A. Maier, P. G. Kik, H. A. Atwater, S. Meltzer, E. Harel, B. E. Koel, and A. A. Requicha, “Local detection of electromagnetic energy transport below the diffraction limit in metal nanoparticle plasmon waveguides,” *Nature materials*, vol. 2, no. 4, p. 229, 2003.
- [122] M. Quinten, A. Leitner, J. R. Krenn, and F. R. Aussenegg, “Electromagnetic energy transport via linear chains of silver nanoparticles,” *Opt. Lett.*, vol. 23, no. 17, pp. 1331–1333, 1998.
- [123] S. Sivakumar, K. L. Wark, J. K. Gupta, N. L. Abbott, and F. Caruso, “Liquid crystal emulsions as the basis of biological sensors for the optical detection of bacteria and viruses,” *Advanced Functional Materials*, vol. 19, no. 14, pp. 2260–2265, 2009.
- [124] P. Bao, D. A. Paterson, P. L. Harrison, K. Miller, S. Peyman, J. C. Jones, J. Sandoe, S. D. Evans, R. J. Bushby, and H. F. Gleeson, “Lipid coated liquid crystal droplets for the on-chip detection of antimicrobial peptides,” *Lab on a Chip*, vol. 19, no. 6, pp. 1082–1089, 2019.
- [125] C. P. Lapointe, S. Hopkins, T. G. Mason, and I. I. Smalyukh, “Electrically driven multiaxis rotational dynamics of colloidal platelets in nematic liquid crystals,” *Phys. Rev. Lett.*, vol. 105, p. 178301, 2010.
- [126] U. Tkalec, M. Ravnik, S. Čopar, S. Žumer, and I. Muševič, “Reconfigurable knots and links in chiral nematic colloids,” *Science*, vol. 333, no. 6038, pp. 62–65, 2011.
- [127] O. D. Lavrentovich, “Transport of particles in liquid crystals,” *Soft Matter*, vol. 10, no. 9, pp. 1264–1283, 2014.
- [128] D. A. Beller, M. A. Gharbi, and I. B. Liu, “Shape-controlled orientation and assembly of colloids with sharp edges in nematic liquid crystals,” *Soft Matter*, vol. 11, no. 6, pp. 1078–1086, 2015.
- [129] Q. Liu, P. J. Ackerman, T. C. Lubensky, and I. I. Smalyukh, “Biaxial ferromagnetic liquid crystal colloids,” *Proceedings of the National Academy of Sciences*, vol. 113, no. 38, pp. 10479–10484, 2016.
- [130] Y. Yuan, A. Martinez, B. Senyuk, M. Tasinkevych, and I. I. Smalyukh, “Chiral liquid crystal colloids,” *Nature materials*, vol. 17, no. 1, p. 71, 2018.

- [131] Y. Yuan, G. N. Abuhaimed, Q. Liu, and I. I. Smalyukh, “Self-assembled nematic colloidal motors powered by light,” *Nature communications*, vol. 9, no. 1, p. 5040, 2018.
- [132] M. Ravnik and S. Žumer, “Nematic braids: 2D entangled nematic liquid crystal colloids,” *Soft Matter*, vol. 5, no. 22, pp. 4520–4525, 2009.
- [133] J.-K. Guo, S.-H. Hong, H.-J. Yoon, G. Babakhanova, O. D. Lavrentovich, and J.-K. Song, “Laser-induced nanodroplet injection and reconfigurable double emulsions with designed inner structures,” *Advanced Science*, vol. 6, no. 17, p. 1900785, 2019.
- [134] C. Lapointe, A. Hultgren, D. M. Silevitch, E. J. Felton, D. H. Reich, and R. L. Leheny, “Elastic torque and the levitation of metal wires by a nematic liquid crystal,” *Science*, vol. 303, no. 5658, pp. 652–655, 2004.
- [135] Y. Luo, D. A. Beller, G. Boniello, F. Serra, and K. J. Stebe, “Tunable colloid trajectories in nematic liquid crystals near wavy walls,” *Nature Communications*, vol. 9, no. 1, p. 3841, 2018.
- [136] A. del Campo and C. Greiner, “SU-8: a photoresist for high-aspect-ratio and 3D submicron lithography,” *Journal of micromechanics and microengineering*, vol. 17, no. 6, pp. R81–R95, 2007.